UNIVERSITY OF
LIVERPOOL

A High Statistics Study of the Scalar Singlet States in Lattice QCD

Thesis submitted in accordance with the requirements of
the University of Liverpool for the degree of Doctor in Philosophy
by
Christopher M. Richards

September 2009

Declaration

I hereby declare that the work described in this thesis is the result of my own research activities unless reference is given to others. None of this material has been previously submitted to this or any University. All work was carried out in the Theoretical Physics division of the Department of Mathematical Sciences during the period October 2005 to September 2009.

Contributions to this work have previously been published or are awaiting publication elsewhere in

- E. B. Gregory, A. C. Irving, C. M. Richards and C. McNeile, "Methods for Pseudoscalar Flavour-Singlet Mesons with Staggered Fermions," Phys. Rev. D **77** (2008) 065019 [arXiv:0709.4224 [hep-lat]].

- E. B. Gregory, C. McNeile, A. C. Irving and C. Richards [UKQCD Collaboration], "A High Statistics Study of Flavour-Singlet Mesons with Staggered Fermions," *To appear in the proceedings of 26th International Symposium on Lattice Field Theory (Lattice 2008), Williamsburg, Virginia, 14-20 July 2008* arXiv:0810.0136 [hep-lat].

Acknowledgements

Firstly I must thank my supervisor Alan Irving for being a fantastic supervisor and, despite his impossibly busy schedule, always being available to answer my questions (which were invariably the same one as a few days before). Your faith and calmness in the last few months and weeks has helped to keep me near to sane.

I'd also like to thank Craig and Eric for keeping this project going — hopefully those D/C plots will come out right in the end! My thanks must also go to Chris who has always had an answer to my questions and for helping me make sense of the behemoth that is `tmmgb`! I should also thank the various support staff that have helped me over the years: George Beckett with the grid, Craig Morris with *that* machine, and most of all Steve Downing with just about everything else.

There have been plenty of postdocs and PhD students over the years, but particular mention goes to Andrea, Kirk, Rob, Conor, Mike, Renzo, Owen and Gary.

2005 seems a hell of a long time ago now but somehow Ben, Cathy, Elisa and Frank made sharing such a small office between five not the hellish experience it ought to have been — I'm sure once I'm out of here I'll look back fondly on the cold winters and hot summers spent turning heaters and fans on and off. Most of all though my thanks go to Cathy for putting up with my desk and floor-based filing system for so long, for always being a sounding post for my stupid questions and for increasing my tea drinking to frankly unhealthy levels.

Obviously I'd like to thank Nicola and Katy — you're the best big sisters I could ask for! Most of all though there are not enough thanks in the world to go to my Mum and to John — I don't know how either of you have found the strength to support me emotionally over the last few months but it has meant the world to me and was one of the very few things that kept me going. Without your support and belief in me I would not and could not have made it this far.

For Mum

fæder alwalda mid arstafum eowic gehealde

Abstract

In this thesis we present a study of the glueball spectrum in lattice QCD, using $2+1$ flavours of Asqtad fermions and the one-loop Symanzik improved Lüscher-Weisz gauge action.

The ensembles for this study have been generated with very high statistics ($N_{\text{traj}} \sim 20000-30000$) to enable us to resolve the notoriously noisy glueball states as accurately as possible. We introduce the theoretical construction of lattice QCD and of staggered fermions in particular before describing how one goes about generating ensembles of gauge fields for such analysis. Here we briefly present our tuning results performed using the improved RHMC algorithm used to generate the finer ensemble.

We then present the methods by which one measures glueballs on the lattice before presenting our measurements and analysis for the scalar glueball. Here we discuss several complications which one may face, as we have, performing spectroscopy on the lattice. We finally present determinations of the 0^{++} and the excited 0^{++} glueball masses, as well as tentative continuum extrapolations.

We have also measured the pseudoscalar and tensor glueball states on our lattices and we present these results. Where possible we present a comparison with previous lattice measurements of the glueball spectrum obtained using both dynamical quarks and the quenched approximation in order to gauge the scale of unquenching effects on the glueball spectrum.

The study of the scalar glueball forms part of a wider physics project by the UKQCD collaboration which aims to study the flavour-singlet sector using $2+1$ flavours of dynamical fermions with unprecedented statistics. We briefly present motivation and an outline of the measurements performed as part of this wider project.

Contents

List of Figures

List of Tables

Chapter 1

Introduction

1.1 Hadron Physics before QCD

During the early 1960s the number of observed particles was becoming particularly large. Of concern to particle physicists was the need for some fundamental way to classify these particles and explain the observed grouping of hadrons into multiplets. In 1963 Gell-Mann and Zweig [1,2] proposed independently that these hadrons may be bound states of more fundamental particles, which Gell-Mann named *quarks*. It was initially proposed that there should be three such quarks — the up (u), down (d) and strange (s) — carrying fractional electric charges of $+\frac{2}{3}, -\frac{1}{3}$ and $-\frac{1}{3}$ respectively. They were thought to lie in the fundamental representation $\mathbf{3}_f$ of $SU(3)_{\text{flavour}}$ (where the subscript 'flavour' has been added for reasons that will become clear later) and their antiparticles ($\overline{u}, \overline{d}$ and $\overline{s}$) in the anti-fundamental representation $\overline{\mathbf{3}}_f$.

If one considers which states one can construct using our quarks and antiquarks one observes that, since the group product of $\mathbf{3}_f$ and $\overline{\mathbf{3}}_f$ decomposes as

$$\mathbf{3}_f \otimes \overline{\mathbf{3}}_f = \mathbf{8}_f \oplus \mathbf{1}_f \tag{1.1}$$

where $\mathbf{8}_f$ and $\mathbf{1}_f$ are the adjoint and trivial representations of $SU(3)_{\text{flavour}}$, it seems natural that one can form a flavour-octet and a flavour-singlet of meson states. It is found that there exists a similar decomposition for the product $\mathbf{3}_f \otimes \mathbf{3}_f \otimes \mathbf{3}_f$ into a decuplet, two octets and a singlet of baryons.

Consider for example the pseudoscalar mesons. The K^+,K^- and K^0,$\overline{K}^0$ each form strange isospin doublets, whereas the isovector π^+,π^0 and π^- form an isospin triplet and the isoscalar η lying at the centre of the octet. The corresponding singlet state is the η'. One can perform a similar classification of the vector mesons.

1.1.1 Colour

Despite the original Gell-Mann and Zweig quark model's successes it has some significant failures. The foremost of these is the absence of free quarks — there is no mechanism in the quark model to bind quarks together and as such the lack of experimental evidence for free quarks is troubling. There were several additional quark models which posited methods by which confinement could be achieved, the foremost of these being the MIT bag model [3].

Furthermore there was evidence of extra hadronic states with an additional quantum number *charm* which require us to introduce a further charm quark c. If we expand our $SU(3)_{\text{flavour}}$ to $SU(4)_{\text{flavour}}$ we find that the flavour symmetry of the 15-plet is badly broken by the heavier charm quark.

The spin-statistics of quarks led to a key development in particle physics — as spin-half fermions one expects them to obey Fermi-Dirac statistics and thus the baryonic wavefunctions should be antisymmetric. The observed baryon spectrum, however, suggests that the wavefunction should be completely symmetric under interchange of the quark spin and flavour, motivating the addition of a further quantum number *colour*.

If the baryon wavefunction is to be completely antisymmetric overall whilst being symmetric in spin and flavour then this requires that it is antisymmetric in colour and further that there should be three possible values of colour (which we name red, green and blue). It seems natural then that this colour quantum number be introduced by supposing that quarks lie in the fundamental representation $\mathbf{3}_c$ of $SU(3)_{\text{colour}}$, and that antiquarks lie in the anti-fundamental representation $\overline{\mathbf{3}}_c$. Mesons and baryons can then be considered as colourless bound states of quarks — mesons requiring the presence of a colour and its own anticolour (*e.g.*, red and anti-red) and baryons being a combination of red, green and blue (or anti-red, anti-green and anti-blue).

1.2 QCD

Whilst extended quark models such as the bag model did reproduce confinement of quarks they did so on a very *ad hoc* basis — there was no fundamental mechanism by which this could be achieved. It was necessary to find a more natural way in which quarks could be bound into colour-singlet states.

One can describe electrons as spin-half solutions of the Dirac equation, and equivalently photons as spin-one solutions of the Klein-Gordon equation. However there are number of physical effects, such as Compton scattering, that suggest electrons and photons interact — these interactions are not accommodated in the quantum field theory by either of the Dirac or Klein-Gordon equations.

The lagrangian describing free electrons

$$\mathcal{L}_D = \overline{\psi}(x)(i\gamma^\mu \partial_\mu - m)\psi(x) \tag{1.2}$$

is invariant under a global $U(1)$ transformation of the fermion field $\psi(x)$

$$\begin{aligned} \psi(x) &\to \psi'(x) = e^{-i\alpha}\psi(x) \\ \overline{\psi}(x) &\to \overline{\psi}'(x) = e^{i\alpha}\overline{\psi}(x) \quad . \end{aligned} \tag{1.3}$$

One can easily promote this global $U(1)$ gauge invariance to a local one by defining the covariant derivative

$$\partial^\mu \to D^\mu = \partial^\mu + ieA^\mu \tag{1.4}$$

and, by substituting this into (1.2)

$$\begin{aligned} \mathcal{L}'_D &= \overline{\psi}(x)(i\gamma^\mu D_\mu - m)\psi(x) \\ &= i\overline{\psi}(x)\gamma^\mu \partial_\mu \psi(x) - e\overline{\psi}(x)\gamma^\mu A_\mu \psi(x) - m\overline{\psi}(x)\psi(x) \quad , \end{aligned} \tag{1.5}$$

the interaction term $e\overline{\psi}(x)\gamma^\mu A_\mu \psi(x)$ emerges. The lagrangian (1.5) is invariant under the following local transformations

$$\begin{aligned} \psi(x) &\to \psi'(x) = e^{-i\alpha(x)}\psi(x) \\ \overline{\psi}(x) &\to \overline{\psi}'(x) = e^{i\alpha(x)}\overline{\psi}(x) \\ A_\mu(x) &\to A'_\mu(x) = A_\mu(x) + \frac{1}{e}\partial_\mu \alpha(x) \quad . \end{aligned} \tag{1.6}$$

The simplest gauge-invariant kinetic term for the field A_μ is

$$\mathcal{L}_A = -\frac{1}{4}F_{\mu\nu}F^{\mu\nu} \tag{1.7}$$

where

$$F_{\mu\nu} = \partial_\mu A_\nu - \partial_\nu A_\mu \tag{1.8}$$

which one can show leads to the Maxwell equations. The full Lagrangian for QED is therefore given by

$$\mathcal{L}_{\text{QED}} = \overline{\psi}(x)(i\gamma^\mu D_\mu - m)\psi(x) - \frac{1}{4}F_{\mu\nu}F^{\mu\nu} \quad . \tag{1.9}$$

Since the quarks and antiquarks lie in the representations **3** and $\overline{\mathbf{3}}$ of $SU(3)_{\text{colour}}$ it seems sensible that, in constructing a lagrangian describing quarks, it should be invariant under $SU(3)$ transformations. Describing quarks as spin-half solutions of the Dirac equation and performing the same promotion of a global $SU(3)$ invariance to a local one, one obtains the QCD lagrangian

$$\mathcal{L}_{\text{QCD}} = \overline{\psi}_i \left(i\not{D} - m_i\right)\psi_i - \frac{1}{4}F_{\mu\nu}F^{\mu\nu} \tag{1.10}$$

where ψ_i and $\overline{\psi}_i$ are the quark and anti-quark fields[1] with flavour i, and the covariant derivative is defined as

$$\not{D} = \gamma^\mu D_\mu = \gamma^\mu \partial_\mu + ig\gamma^\mu A_\mu \tag{1.11}$$

and introduces interactions between the quarks and the bosons mediating the gauge field. However whilst the introduction of a virtual particle — the *gluon* — explains in a consistent and field-theoretical manner the observed hadron spectrum there is still no *a priori* explanation as to why lone quarks are not observed.

The last term of the lagrangian describes the dynamics of the gauge field itself, and due to the non-Abelian nature of $SU(3)$ includes additional self-interactions of the gauge field

$$F_{\mu\nu}(x) = \sum_a \lambda^a F^a_{\mu\nu}(x) \quad , \tag{1.12}$$

where $F^a_{\mu\nu}$ is defined in terms of the gluon fields by

$$\begin{aligned} F^a_{\mu\nu} &= \partial_\mu A^a_\nu - \partial_\nu A^a_\mu + ig\left[A^a_\mu, A^a_\nu\right] \\ &= \partial_\mu A^a_\nu - \partial_\nu A^a_\mu - g f^{abc} A^b_\mu A^c_\nu \quad , \end{aligned} \tag{1.13}$$

where the gluons themselves lie in the adjoint representation **8** of $SU(3)$. These self interactions are postulated to give rise to bound states of gluons which we refer to as *glueballs* and will be discussed in more detail in Chapter 5.

A more in depth discussion of QCD can be found in any elementary textbook on quantum field theory, *e.g.* Peskin and Schröder [4].

1.2.1 Perturbative QCD

A common way of performing calculations in QCD, for example computing matrix elements, is to perform them perturbatively — this involves expanding in terms of the coupling constant g. Due to large renormalisation effects the coupling in QCD is strongly dependent on the energy scale at which it is measured, a phenomenon known as *running*. This dependence can be described by the β function which is a solution of the renormalisation group equation (RGE)

$$\beta(g) = \mu \frac{\partial g}{\partial \mu} \quad . \tag{1.14}$$

One can show that, at one-loop, the solution to (1.14) is given by

$$g^2(\mu) = \frac{16\pi^2}{\beta_0 \ln\left(\mu/\Lambda_{\mathrm{QCD}}\right)} \tag{1.15}$$

where Λ_{QCD} is the intrinsic momentum scale of QCD and β_0 is defined as

$$\beta_0 = \left(11 - \frac{2}{3} N_{\mathrm{f}}\right) \tag{1.16}$$

[1] Colour and Dirac indices are suppressed.

One can see that, provided that $N_f \leq 16$, as one increases the energy scale μ the coupling decreases, approaching zero as one takes μ to infinity — a phenomenon referred to as *asymptotic freedom*. The smallness of g at high energies means one can perform perturbative expansions here. At lower energies g becomes large and as such perturbation theory breaks down — this is referred to as the strong coupling or non-perturbative regime. This non-perturbative regime is where effects such as confinement of quarks are observed most strongly, and therefore in order to study bound states of quarks and gluons one must work here.

Chapter 2

Lattice QCD

2.1 Non-Perturbative Physics

As we can see from §1.2.1 perturbation theory breaks down at low energy scales due to our expansion parameter — the coupling — becoming large. This forces us to compute diagrams of higher and higher orders as well as their renormalisation counterterms which motivates us to find another way to study the strong-coupling limit of QCD in a theoretically sound way, that is to say without the use of effective field theories. In systems where the dynamics of the QCD vacuum is of great importance, for example topological field theory and the axial anomaly, perturbation theory is of little use and one must use non-perturbative methods — lattice QCD allows us to study such effects from first principles and as such is an attractive method.

2.2 Lattice Discretisation

Wilson introduced [5] a discrete four-dimensional Euclidean space-time lattice as a natural regulator. By considering our field theory on this lattice (with sites spaced by the lattice spacing a) we have introduced an ultraviolet momentum cutoff since modes can have wavelengths no less than $2a$ which implies a momentum cutoff of $\frac{\pi}{a}$, which can be removed in a consistent way by taking the limit $a \longrightarrow 0$ — the *continuum limit.*

Of course our field theory defined in Section 1.2 is defined in Minkowski spacetime — the action appears in the path integral approach as a phase e^{iS}. In order to consider our action in Euclidean spacetime we perform a Wick rotation to imaginary time, which formally amounts to a continuous rotation of our temporal coordinate from the real axis to the imaginary one. This has the additional benefit that the real-time phase e^{iS} now appears in imaginary time as a real and positive weight e^{-S_E}, where S_E is the action in Euclidean space[1] — this useful property will be used extensively in Chapter 3.

[1]Unless explicitly stated S,L and $\mathcal{L}$ shall correspond to the action, Lagrangian and Lagrangian density in Euclidean space from here on.

In addition to allowing us to define a theory without infinities the lattice has also reduced the number of degrees of freedom of our theory from an infinite number to a finite but, depending on our lattice volume, large number. This allows us to replace our analytic path integral by a finite sum.

2.3 QCD on the Lattice

There are two key requirements which we must bear in mind when discretising a gauge field theory on the lattice: firstly the action must be gauge invariant and secondly, and perhaps of more importance, it must have the correct continuum limit *i.e.* that of the original continuum gauge theory.

To discretise the QCD gauge action we define the gauge field on the links of the lattice as

$$U_\mu(x) = \mathcal{P} \exp\left(ig \int_x^{x+\hat{\mu}} A_\mu(x)\, dx_\mu \right) = \exp\left(igaA_\mu(x) \right) \tag{2.1}$$

where, as in the continuum, $A_\mu = \sum_b A_\mu^b \lambda_b$ is the vector potential and $U_\mu(x)$ is the parallel transporter of the $SU(3)$ colour matrices between sites x and $x + \hat{\mu}$ ($\hat{\mu}$ being the unit-vector in the direction μ) which we refer to collectively as *link variables.*

These link variables transform as

$$U_\mu(x) = \Lambda(x) U_\mu(x)\, \Lambda(x+\hat{\mu})^\dagger \tag{2.2}$$

where $\Lambda(x)$ and $\Lambda(x+\hat{\mu})$ are arbitrary $SU(3)$ matrices which we associate with the sites rather than the links.

Using the transformation property (2.2) we can begin to see how our first requirement of gauge invariance can be satisfied. Consider the product of links around an elementary square in the (μ,ν)-plane of the lattice, which is referred to in the literature as a plaquette,

$$P_{\mu\nu}(x) = U_\mu(x)\, U_\nu(x+\hat{\mu})\, U_\mu(x+\hat{\nu})^\dagger\, U_\nu(x)^\dagger \quad . \tag{2.3}$$

By using property (2.2) and unitarity it is trivial to show that the trace of the plaquette is gauge invariant. As an incredibly simple gauge invariant object the trace of the plaquette is used extensively throughout lattice QCD.

2.3.1 Wilson's Action

By writing each link variable in full using (2.1) it can be shown that

$$\begin{aligned} \sum_x \sum_{\mu<\nu} \mathrm{Tr}\, P_{\mu\nu}(x) &= \sum_x \sum_{\mu<\nu} \mathrm{Tr} \exp\left(iga^2 F_{\mu\nu}(x) \right) \\ &= \sum_x \sum_{\mu<\nu} \mathrm{Tr} \left(1 - iga^2 F_{\mu\nu}(x) + \frac{g^2 a^4}{2} F_{\mu\nu}(x) F_{\mu\nu}(x) + \mathcal{O}(a^6) \right) \quad . \end{aligned} \tag{2.4}$$

Wilson made the identification between (2.4) and the last term of (1.10) and suggested the following form for a discretised QCD action:

$$S_W^G = \frac{6}{g^2} \sum_x \sum_{\mu<\nu} \frac{1}{3} \mathrm{Re\,Tr}\ (\mathbf{1} - P_{\mu\nu}(x)) \tag{2.5}$$

where, by substituting (2.4) we obtain

$$S_W^G = -\frac{a^4}{4} \sum_x \left(F_{\mu\nu}(x) F_{\mu\nu}(x) + \mathcal{O}(a^2) \right) \quad . \tag{2.6}$$

The coupling constant $\frac{6}{g^2}$ occuring in (2.4) is often referred to in the literature as β.

2.3.2 Lüscher-Weisz Action

In the expansion of (2.4) there are higher order terms at $\mathcal{O}(a^6)$ and beyond that ruin the correspondence between the continuum and lattice action. These are known as lattice artefacts and can manifest themselves in many lattice measurements. In order to reduce the impact of these artefacts one is forced to work at small lattice spacings which either leads to increased finite-size effects or forces us to work at large volumes. Obviously this is an unacceptable situation and one must find a way of improving the action so that these artefacts occur at a higher order.

The first terms occurring beyond $F_{\mu\nu}F_{\mu\nu}$ were identified by Weisz [6] and are the following dimension-six operators:

$$\begin{aligned} \mathcal{O}_6^1 &= r_1 \sum_{\mu,\nu} \mathrm{Tr}\ (D_\mu F_{\mu\nu} D_\mu F_{\mu\nu}) \\ \mathcal{O}_6^2 &= r_2 \sum_{\mu,\nu,\rho} \mathrm{Tr}\ (D_\mu F_{\nu\rho} D_\mu F_{\nu\rho}) \\ \mathcal{O}_6^3 &= r_3 \sum_{\mu,\nu,\rho} \mathrm{Tr}\ (D_\mu F_{\mu\rho} D_\mu F_{\mu\rho}) \quad . \end{aligned} \tag{2.7}$$

Lüscher and Weisz [7] have identified a basis of six-link Wilson loops which can be used to cancel the contribution of these dimension-six operators to a given quantity. Using the Symanzik improvement program [8,9] they have found the set of coefficients for the Wilson loops shown in Fig. 2.1 that remove the $\mathcal{O}(a^2)$ scaling violations from the scattering amplitude. Indeed they show that under a field redefinition using the equations of motion one can, without loss of generality, set one of the coefficients to zero [7,10]. The remaining coefficients have been determined to one-loop [11] and the resulting action is referred to in the literature as the one-loop Lüscher-Weisz gauge action, and is the foundation of the gauge action used to generate the configurations for this work.

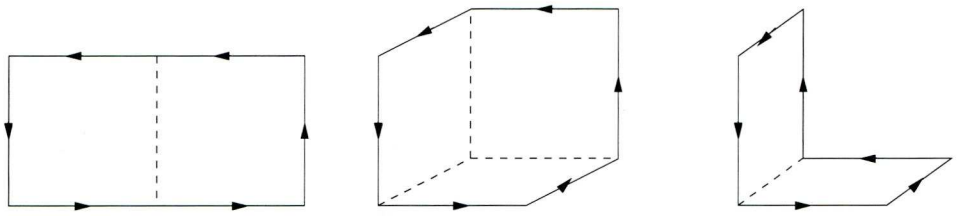

Figure 2.1: The three six-link loops used to cancel the dimension-six operators in (2.7). These are, from left to right, the double rectangle, parallelogram and chair terms.

It is important to note that the double-rectangle operator couples links on different timeslices and because of this our usual consideration of the transfer matrix as a time evolution operator runs into problems. Lüscher and Weisz [12] have proven in general that for improved actions where positivity is violated in this way we are still able to determine masses from the exponential fall-off of two-point correlation functions but that care must be paid for small temporal separations of source and sink. Similarly when using the variational method (§4.4) we must be careful not to set our basis at too small a value of t_0.

2.3.3 Tadpole Improvement

When performing lattice perturbation theory we expand the link variable (2.1) in terms of A_μ as follows

$$U_\mu(x) = \exp\left(igaA_\mu(x)\right) = 1 + iagA_\mu(x) - a^2g^2A_\mu(x)A_\mu(x) + \ldots \quad . \tag{2.8}$$

One might presume that, given the smallness of a^2g^2, one should be able to truncate this expansion at the first non-constant term and still obtain a rapidly convergent approximation. Unfortunately this turns out not to be the case — tadpole diagrams in the theory are divergent and when computed reduce to a form $\sim \frac{1}{a}$ which resurrects higher order terms that could otherwise have been neglected, ruining the convergence of lattice perturbation theory at all but the smallest values of a and introducing significant lattice spacing effects in physical observables.

In order to repair lattice perturbation theory Lepage and Mackenzie [13] noted that if the gauge links are reweighted such that

$$U_\mu(x) \leftarrow U_\mu(x) = u_0 \exp\left(igaA_\mu(x)\right) \approx u_0\left(1 + iagA_\mu\right) \tag{2.9}$$

then one can improve the convergence of lattice perturbation theory by enforcing that the expansion in the new link variables matches some physically expected value at a given order of perturbation theory (typically leading order).

The tadpole-improved plaquette can be written

$$\mathrm{Tr}\, P_{\mu\nu} = \frac{1}{u_0^4}\mathrm{Tr}\left(U_\mu(x)\, U_\nu(x+\hat{\mu})\, U_\mu(x+\hat{\nu})^\dagger\, U_\nu(x)^\dagger\right) \tag{2.10}$$

thus one can define u_0 by

$$u_0 = \left\langle \frac{1}{3}\mathrm{Tr}\, P_{\mu\nu} \right\rangle^{\frac{1}{4}} \tag{2.11}$$

which, being simple to compute, allows us to adjust our tadpole parameter on the fly. It has been observed [14–16] that discretisation effects are most improved when one computes u_0 as the mean link in Landau gauge

$$u_{0,L} = \left\langle \frac{1}{3}\mathrm{Tr}\, U_\mu \right\rangle \ , \quad \partial_\mu A_\mu = 0 \tag{2.12}$$

however for comparability with previous results we continue to use (2.11) to compute our tadpole factor.

One can apply tadpole improvement to the coefficients of the improvement terms in the one-loop Lüscher-Weisz gauge action presented in §2.3.2 in order to obtain the tadpole improved one-loop Lüscher-Weisz gauge actions — this is the gauge action used to generate the configurations for this study.

2.4 Discretising the Fermion Action

So far we have only placed the gauge fields on to the lattice. In order to simulate QCD fully we must also introduce the fermion fields onto the lattice. Recalling from Chapter 1 the fermionic piece of the continuum action is

$$S_{\text{fermion}} = \int d^4x\, \overline{\psi}(x)\, (\not{D} + m)\, \psi(x) \tag{2.13}$$

where we have taken the Dirac and colour indices as implicit.

2.4.1 Naïve fermions

The first thing we must do is define a lattice version of the continuum covariant derivative $\not{D}$

$$\gamma^\mu \hat{D}_\mu \psi(x) = \sum_\mu \gamma^\mu \left(\frac{U_\mu(x)\psi(x+\hat{\mu}) - U_\mu^\dagger(x-\hat{\mu})\psi(x-\hat{\mu})}{2a} \right) \tag{2.14}$$

where the gauge links have been inserted to ensure gauge invariance. Inserting this into the action, and replacing the integral with a lattice sum, we obtain

$$S_{\text{fermion}}^{\text{naive}} = \sum_x \left[\frac{1}{2a}\overline{\psi}(x) \sum_\mu \gamma^\mu \left(U_\mu(x)\psi(x+\hat{\mu}) - U_\mu^\dagger(x-\hat{\mu})\psi(x-\hat{\mu}) \right) + m\overline{\psi}(x)\psi(x) \right] . \tag{2.15}$$

By expanding the link variable $U_\mu(x)$ as usual one can show that this gives us the fermion part of the continuum QCD action, up to $\mathcal{O}(a^2)$ lattice artefacts.

The Fermion Matrix

We can write our action in a more compact form by defining the *fermion matrix* M_{xy}

$$M_{xy} = \sum_{\mu} \gamma^{\mu} \left(U_{\mu}(x)\delta_{x+\hat{\mu},y} - \delta_{x-\hat{\mu},y} U_{\mu}^{\dagger}(y) \right) + m\delta_{xy} \tag{2.16}$$

so that our naïve fermion action can now be written more compactly as

$$S_{\text{fermion}}^{\text{naive}} = \frac{1}{2a} \sum_{x,y} \overline{\psi}(x) M_{xy} \psi(y) \quad . \tag{2.17}$$

One can easily show that the two-point function for ψ (*i.e.* the fermion propagator) is

$$\langle \psi(x)\overline{\psi}(y) \rangle = M_{xy}^{-1} \tag{2.18}$$

and furthermore

$$\langle \psi(x)\overline{\psi}(y) \rangle = \lim_{a \to 0} \int_{-\frac{\pi}{a}}^{\frac{\pi}{a}} \frac{d^4p}{(2\pi)^2} \frac{-i\gamma^{\mu} \frac{1}{a} \sin p_{\mu} a + m}{\frac{1}{a^2} \sin^2 p_{\mu} a + m^2} e^{ip(x-y)} \tag{2.19}$$

which is the inverse Fourier transform of the momentum space propagator (where sums over μ in both the numerator and denominator are implied)

$$S(p) = \frac{-i\gamma^{\mu} \frac{1}{a} \sin p_{\mu} a + m}{\frac{1}{a^2} \sin^2 p_{\mu} a + m^2} \quad . \tag{2.20}$$

Comparing this to the continuum momentum space propagator

$$S(p) = \frac{-i\gamma^{\mu} p_{\mu} + m}{p^{\mu} p_{\mu} + m^2} \tag{2.21}$$

one sees that (2.20) reduces to the same form in the limit $a \to 0$, with $\mathcal{O}(a^2)$ artefacts, however at finite lattice spacing one may observe a problem with the momentum space poles.

The Doubling Problem

We can see from (2.21) that in the continuum there is a single momentum space pole at $p = (0,0,0,0)$ corresponding to the Dirac fermion with mass m. Comparing the denominator of (2.20) to that of (2.21) we see that whilst the denominator has the expected physical pole at $p = (0,0,0,0)$, corresponding to the Dirac fermion, it also has poles wherever $p_{\mu} = \frac{\pi}{a}$. These fifteen unphysical poles are referred to as *doublers* and avoiding this doubling problem has been the subject of much work in developing lattice QCD.

It is important to note that at a classical level these doublers are not of great concern — we could focus our attention on the $p = (0,0,0,0)$ pole p_0 — however at the quantum level one-loop contributions cause mixing between the different poles. Karsten and Smit [17] derived the spectrum of these doublers allowing us to consider their interactions in a more formal manner.

2.4.2 Wilson Fermions

In order to remedy this doubling problem Wilson [18] introduced a second derivative like term to the naïve fermion action

$$S^{\mathrm{W}} = -\frac{r}{2a}\overline{\psi}(x)\sum_{\mu}\gamma^{\mu}\left(U_{\mu}(x)\psi(x+\hat{\mu}) - 2\psi(x) + U_{\mu}^{\dagger}(x-\hat{\mu})\psi(x-\hat{\mu})\right) \quad . \tag{2.22}$$

This term introduces a term dependent on r into the denominator of the momentum space propagator which has the effect of lifting the doubler poles to masses $\sim \frac{1}{a}$ and hence decoupling them completely in the continuum limit, leaving us with a single pole corresponding to the physical Dirac fermion. However the additional term contains a contribution $\frac{r}{a}\overline{\psi}(x)\psi(x)$ which acts as a mass term, explicitly breaking chiral symmetry even in the $m \to 0$ limit and requiring additive mass renormalisation as well as the usual multiplicative renormalisation.

The Nielsen-Ninomiya No Go Theorem

This sacrificing of chiral symmetry in order to remove the doublers from our theory is not coincidental. There is a no go theorem due to Nielsen and Ninomiya [19–21] which states that, under a set of assumptions, one cannot construct an action which possesses chiral symmetry, locality and translational invariance without introducing doublers.

2.5 Staggered Fermions

One can show that each of the doubler poles in (2.20) are related by a set of similarity transformations [17]. One can exploit this symmetry by performing a spin diagonalisation on the action (2.15) in order to reduce the degeneracy by a factor of four.

This diagonalisation can be performed by defining our staggered fermion fields $\chi(x)$ and $\overline{\chi}(x)$ by

$$\begin{aligned} \psi(x) &\to \Omega(x)\chi(x) \\ \overline{\psi}(x) &\to \overline{\chi}(x)\Omega^{\dagger}(x) \end{aligned} \tag{2.23}$$

where we choose $\Omega(x)$ such that when these fields are inserted into (2.15) the action becomes diagonal in spin space. This is possible by choosing the following form [22,23] for $\Omega(x)$

$$\Omega(x) = \gamma_1^{x_1}\gamma_2^{x_2}\gamma_3^{x_3}\gamma_4^{x_4} \quad . \tag{2.24}$$

Substituting (2.23) and (2.24) into (2.15) we obtain the naïve staggered fermion action

$$S_{\mathrm{ferm}}^{\mathrm{stag}} = \frac{1}{2a}\sum_{x,\mu}\overline{\chi}(x)\eta_{\mu}(x)\left(U_{\mu}(x)\chi(x+\hat{\mu}) - U_{\mu}(x-\hat{\mu})\chi(x-\hat{\mu})\right) + m\sum_{x}\overline{\chi}(x)\chi(x) \tag{2.25}$$

where the $\eta_\mu(x)$ are defined by

$$\eta_\mu(x) = \Omega^\dagger(x)\gamma_\mu\Omega(x+\hat{\mu}) = (-1)^{\sum_{\nu<\mu} x_\nu} \tag{2.26}$$

and are referred to as the staggered or Kogut-Susskind phases. Since these $\eta_\mu(x)$ depend on the lattice site and direction only we have an action without any spin indices and we are able to ignore three of the four components of our staggered fields, reducing the degeneracy from a sixteen-fold degeneracy to a four-fold one. We refer to the symmetry under which these four degenerate fields interchange as *taste symmetry.*

2.5.1 Residual Chiral Symmetry

In (2.25) we see that the kinetic term couples fields at even sites to those at odd sites, and vice versa. By defining the matrix $\epsilon(x)$

$$\epsilon(x) = (-1)^{\sum_\mu x_\mu} \tag{2.27}$$

we see that the kinetic term is invariant under the set of transformations

$$\begin{aligned} \chi(x) &\to e^{i\theta\epsilon(x)}\chi(x) \\ \overline{\chi}(x) &\to \overline{\chi}(x)e^{i\theta\epsilon(x)} \quad . \end{aligned} \tag{2.28}$$

This axial $U(1)_A$ symmetry, when combined with the exact vector $U(1)$ symmetry $U(1)_V$ results in a $U(1)_V \otimes U(1)_A$ for the massless action. The axial part of this symmetry is broken by the mass term as one would expect but is enough to protect us from the additive mass renormalisation required by the Wilson action as well as providing us with a natural pseudo-Goldstone boson.

At all quark masses our fermion matrix satisfies a modified γ_5-hermiticity

$$M(x,y)^\dagger = \epsilon(x)M(x,y)\epsilon(y) \tag{2.29}$$

and at zero quark mass is antihermitian. One can also show that the spectrum of the staggered fermion kernel $M^\dagger M$ is bounded from below by a^2m^2 which for finite quark masses protects us from the small or zero eigenvalues which plague the Wilson formalism. This allows us to simulate lattice QCD at quark masses far smaller than is feasible using standard Wilson fermions.

2.5.2 Kluberg-Stern Representation

At this stage we are still dealing with fields in which our spin has been spread out across the hypercube. In order to make connection back to our original fermion fields in order to form, for instance, quark bilinears we need to be able to construct quark fields from our staggered fermion fields.

If we consider a hypercube with its origin at $x_\mu = 2y_\mu$ then the hypercube can be parameterised by its origin x_μ and its 16 corners as follows

$$r_\mu = 2y_\mu + \rho_\mu \quad \text{where} \quad \rho_\mu = 0 \text{ or } 1 \ . \tag{2.30}$$

It is convenient to relabel the fields $\chi, \overline{\chi}$ by making the identification

$$\chi_\rho(y) \equiv \chi(2y + \rho) \tag{2.31}$$

where our fields are now defined on a lattice with spacing $2a$. One can now reconstruct Dirac 'quark' fields by taking an appropriate linear combination of the fields over a hypercube[2]

$$Q^{a\alpha}(y) = \frac{1}{8}\sum_\rho \Gamma_\rho^{a\alpha}\chi_\rho(y) \tag{2.32}$$

$$\overline{Q}^{a\alpha}(y) = \frac{1}{8}\sum_\rho \overline{\chi}_\rho(y)\Gamma_\rho^{\dagger a\alpha} \tag{2.33}$$

where

$$\Gamma_\rho = \gamma_1^{\rho_1}\gamma_2^{\rho_2}\gamma_3^{\rho_3}\gamma_4^{\rho_4} \tag{2.34}$$

and α is the usual Dirac spin index and a labels the staggered taste.

One can reverse (2.32) and (2.33) to obtain

$$\chi_\rho(y) = 2\sum_{a,\alpha} \Gamma_\rho^{\dagger a\alpha} Q^{a\alpha}(y) \tag{2.35}$$

$$\overline{\chi}_\rho(y) = 2\sum_{a,\alpha} \overline{Q}^{a\alpha}(y)\Gamma_\rho^{a\alpha} \ , \tag{2.36}$$

substituting these into (2.25) and setting the gauge field equal to one everywhere one obtains the action

$$S = \frac{1}{2a}\sum_{y,\alpha,\beta,a,b} \overline{Q}^{a\alpha}(y)\left\{\sum_\mu \left[\Gamma_\rho^{a\alpha}\left(\delta_{\rho+\hat{\mu},\rho'} + \delta_{\rho-\hat{\mu},\rho'}\right)\eta_\mu(\rho)\Gamma_{\rho'}^{\dagger b\beta}\Delta_\mu \right.\right. \tag{2.37}$$
$$\left.\left. + \frac{1}{2}\Gamma_\rho^{a\alpha}\left(\delta_{\rho-\hat{\mu},\rho'} - \delta_{\rho+\hat{\mu},\rho'}\right)\eta_\mu(\rho)\Gamma_{\rho'}^{\dagger b\beta}\Box_\mu\right] + 2m\delta_{\alpha\beta}\delta_{ab}\right\} Q^{b\beta}(y)$$

where Δ_μ and $\Box_\mu$ are the symmetric first and second derivatives respectively, defined via their actions as

$$\Delta_\mu Q(y) = \frac{1}{4a}\left(Q(y+\hat{\mu}) - Q(y-\hat{\mu})\right) \tag{2.38}$$

$$\Box_\mu Q(y) = \frac{1}{4a^2}\left(Q(y+\hat{\mu}) + Q(y-\hat{\mu}) - 2Q(y)\right) \ . \tag{2.39}$$

We can see from the mass term that it is symmetric in both spin and taste indices. We follow the notation of Kluberg-Stern and write $\delta_{\alpha\beta}\delta_{ab}$ as the direct product $\mathbf{1} \otimes \mathbf{1}$

[2]The factor of $\frac{1}{8}$ is specific to four-dimensions — in d dimensions it is $\frac{1}{2^{d/2}\sqrt{2^{d/2}}}$.

, where the first matrix acts in spin space and the second in taste space — this is referred to as spin⊗taste or *Kluberg-Stern* notation. The situation for the kinetic term is slightly less clear but after some algebra (see [22, 24, 25] for details) we obtain

$$S = (2a)^4 \sum_{y,\mu} \overline{Q}(y) \left[(\gamma_\mu \otimes \mathbf{1}) \, \Delta_\mu + a \, (\gamma_5 \otimes \xi_\mu \xi_5) \, \Box_\mu \right] Q(y) \qquad (2.40)$$
$$+ (2a)^4 m \sum_y \overline{Q}(y) \, (\mathbf{1} \otimes \mathbf{1}) \, Q(y)$$

where $\xi_\mu = \gamma_\mu^\dagger$ and is the taste space equivalent of γ_μ.

We can see that the first part of the kinetic term is symmetric in taste space and a vector in spin space as one expects in the continuum, and as noted previously the mass term is a spin and taste singlet. However we see that the second piece of the kinetic term is not symmetric in taste space — this breaks the taste symmetry at nonzero lattice spacing. However in order to simplify the discussion we have been working in the unit gauge — in the interacting theory the expression for the quark fields (2.32) and (2.33), and likewise the inverse expressions (2.35) and (2.36) will include gauge links in order to preserve gauge invariance. With these gauge links included there is no simple expression such as (2.40) for the staggered action and one must expand the action in powers of the lattice spacing.

2.5.3 Taste Breaking

By expanding the action in powers of the lattice spacing one sees that there are dimension five operators (and beyond) which violate the taste symmetry [26, 27] and occur at $\mathcal{O}(a)$. However by following the Symanzik program it can be shown [28, 29] that we are unable to construct dimension-five operators (which occur with a dimensional factor $\mathcal{O}(a)$) that respect the symmetries of the action and therefore the action must already be improved at $\mathcal{O}(a)$ such that any taste symmetry violations must occur at $\mathcal{O}(a^2)$ or above. Indeed one can show [27] that taste symmetry is in fact broken by dimension-six effective four-fermion operators at $\mathcal{O}(a^2)$.

One can understand the mechanism behind taste breaking more clearly if one considers the action in momentum space. The taste of our fermion depends on from which corners of the Brillouin zone it receives contributions — in the free theory defined in (2.40) these tastes are linked by an exact symmetry under interchanges of the various momentum components. However in the interacting theory the momenta can be changed by the exchange of a highly virtual gluon with a momentum (in lattice units) of $\sim \pi$ between two fermions[3], resulting in a change of taste. Such interactions are referred to as *taste breaking* or *taste changing* interactions. Since each quark-gluon

[3] One might well be concerned that self-energy diagrams might cause a similar effect, however flavour breaking effects "cancel" in such one-loop diagrams.

vertex carries a factor of α_s taste symmetry violations are now suppressed even further to an $\mathcal{O}(a^2\alpha_s^2)$ effect.

These taste breaking effects are perhaps most evident in the pion spectrum — the pion spectrum falls into 8 distinct irreps of the lattice group [30–32] which can be loosely grouped into five taste multiplets ($i, j < 4$):

- P: pseudoscalar $\gamma_5 \otimes \gamma_5$
- V: vector $\gamma_5 \otimes \gamma_i$ and $\gamma_5 \otimes \gamma_4$
- A: axial-vector $\gamma_5 \otimes \gamma_i\gamma_5$ and $\gamma_5 \otimes \gamma_4\gamma_5$
- T: tensor $\gamma_5 \otimes \gamma_i\gamma_j$ and $\gamma_5 \otimes \gamma_i\gamma_4$
- I: singlet $\gamma_5 \otimes \mathbf{1}$

The pseudoscalar, vector, axial-vector and tensor multiplets form the $SU(4)$ irrep **15**, and the singlet the $SU(4)$ irrep **1** (where $\mathbf{4} \otimes \overline{\mathbf{4}} = \mathbf{15} \oplus \mathbf{1}$). In the continuum limit these are degenerate as one expects since this $SU(4)$ taste symmetry is an artefact of the lattice fermion construction, however at finite lattice spacing they are split from each other — this splitting can be rather dramatic, particularly in the naive staggered fermion formulation outlined above. As one might expect this splitting decreases as one takes the continuum limit.

2.6 Taste Symmetry Improvement

In order to improve this taste symmetry breaking it is evident that one must reduce the coupling of the fermions to these high momentum gluons. This is relatively simple to achieve if one considers the gluon propagator — in momentum space it is essentially the two-point function of the Fourier transform of the gluon fields and therefore the high momentum gluons correspond to highly local quantities. Thus, by replacing the link variable by something less local, one can reduce or indeed remove completely the high momentum modes. Such *smearing* techniques are used extensively in topology [33, 34] and glueball spectroscopy [35, 36].

The simplest such replacement one can make [37] is by replacing the single links $U_\mu(x)$ in the covariant derivative by the link plus a weighted sum of the six three-link paths, or *staples*, surrounding it. The resulting link $\widetilde{U}_\mu(x)$ is referred to as a *fat link*

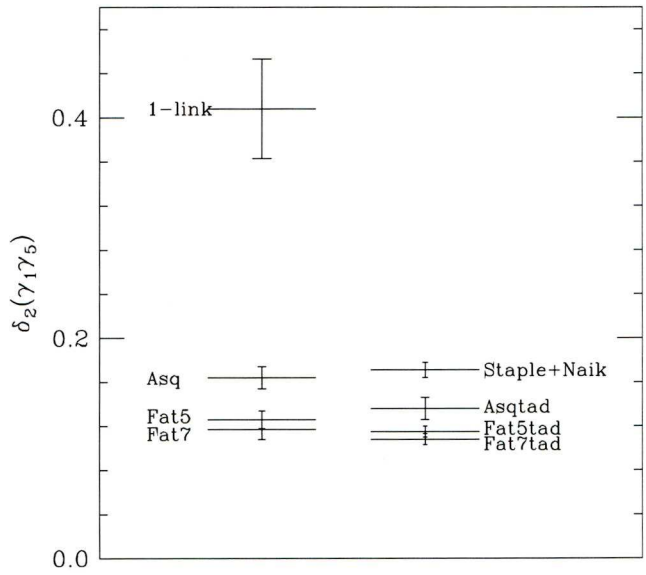

Figure 2.2: The measure of taste-symmetry violation δ_2 (defined as $\delta_2(\xi) = \left(m^2_{\pi_{\gamma_5\otimes\xi}} - m_{\pi_{\gamma_5\otimes\gamma_5}}\right) / \left(m^2_{\rho_{\gamma_5\otimes\xi}} - m_{\rho_{\gamma_5\otimes\gamma_5}}\right)$) for $\xi = \gamma_1\gamma_5$ for various staggered action improvements. Data from [40].

and can be written

$$\widetilde{U}_\mu(x) = \frac{1}{1+6w}\left[U_\mu(x) + w\sum_{\nu\neq\mu}\left(U_\nu(x)U_\mu(x+\hat{\nu})U^\dagger_\nu(x+\hat{\mu})\right.\right. \tag{2.41}$$
$$\left.\left. + U^\dagger_\nu(x-\hat{\nu})U_\mu(x-\hat{\nu})U_\nu(x-\hat{\nu}+\hat{\mu})\right)\right]$$

where w is an adjustable weight. The level of taste-symmetry has been shown to be relatively insensitive to the value of the weight used, with a value of 0.5 resulting in a reduction in their particular measure of splitting (the splitting between the Goldstone pion $\gamma_5\otimes\gamma_5$ and the $\gamma_5\otimes\mathbf{1}$ pion[4]) by a factor of three. Lepage carried out an analysis of taste-symmetry breaking within the framework of the Symanzik improvement program [38] and showed that the same three-link paths along with five and seven-link paths, were needed to completely suppress the tree-level coupling to high momentum gluons, but that they introduce $\mathcal{O}(a^2p^2)$ errors such that a further five-link path is required in order to correct these errors. As well as taste-symmetry improvements there is an additional third-nearest neighbour term introduced by Naik [39] which improves the quark-dispersion relation.

2.6.1 The Asqtad Action

To date the most widely used staggered fermion variant is the Asqtad action. This makes use of the taste symmetry improvements described above as well as the Naik

[4]Disconnected diagrams were not included, so this is technically a taste-split pion.

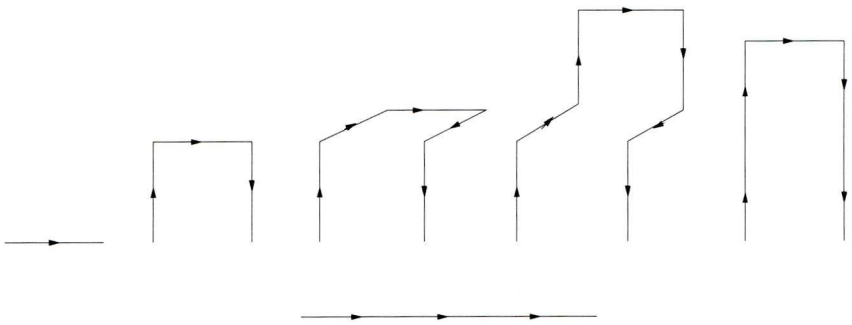

Figure 2.3: The improvement terms used in the asqtad action. Top (left to right): basic link (coefficient c_1), three-link staple (c_3), five-link non-planar (c_5), seven-link non-planar 'chair' (c_7), five-link planar Lepage term c_L.
Bottom: three-link Naik term (c_N). Coefficients are shown without their respective tadpole improvement factors.

term but the gauge links in the derivative are first tadpole improved using the tadpole improvement factor as defined in (2.11). For clarity the improvement terms are shown in Fig. 2.3. Whilst the taste-symmetry violations are larger than those for the Fat5 and Fat7 actions (and their tadpole improved versions), as demonstrated in Fig. 2.2, the Asqtad and Asq actions include the Lepage and Naik terms which have value in physics apart from the taste-symmetry issues — primarily their improved rotational symmetry due to the Naik term and the correction of $\mathcal{O}(a^2p^2)$ errors by the Lepage term — for which the introduction of $\mathcal{O}(a^4)$ taste-symmetry violations is deemed a satisfactory sacrifice. The large number of additional terms used to improve taste-symmetry does lead to some difficulties with certain algorithms and this will be discussed in Chapter 3.

2.6.2 The HISQ Action

Whilst the Asqtad action does well with regards to taste-symmetry violation for light quark masses, where their relativistic nature means that higher order $\mathcal{O}(a^4p^4)$ terms are negligible, this is no longer the case for heavier quarks such as charm where the large quark masses means we are dealing with errors at $\mathcal{O}(a^4m^4)$. Improving taste-symmetry here is particularly important given the rather fine splitting effects in the charmonium spectrum. The Fat7tad or *Highly-Improved Staggered Quark* (HISQ) action [41] is the most widely used of the staggered variants, using multiple levels of smearing similar to those used in Asqtad with the inclusion of a reunitarisation step, and has produced some excellent results in heavy-light and heavy quark physics [42].

2.7 Other Actions

2.7.1 Chiral Fermions

Whilst staggered fermions possess a remnant chiral symmetry we still lack a lattice fermion formulation exhibiting exact chiral symmetry. This, in part, is due to the Nielsen-Ninomiya no-go theorem. Our condition for chiral symmetry is

$$\{\gamma_5, D\} = 0 \tag{2.42}$$

i.e. that our Dirac operator anticommutes with γ_5. This is true of the continuum Dirac operator and indeed of the naïvely discretised Dirac operator. One can write the Ginsparg-Wilson (GW) relation [43]

$$\{\gamma_5, D\} = aD\gamma_5 D \tag{2.43}$$

which, for finite a breaks chiral symmetry but in the continuum limit reduces exactly to (2.42), *i.e.* chiral symmetry is recovered as one takes the continuum limit. The most frequently used fermion formulations which obey the GW-relation are overlap fermions [44] and Domain Wall fermions [45, 46]. Both of these formulations, whilst possessing exact chiral symmetry in the continuum, are more computationally expensive than the actions we have met so far.

2.7.2 Wilson Twisted-Mass Fermions

In §2.4.2 we introduced the Wilson term which removes the doublers from lattice QCD, at the expensive of explicitly breaking chiral symmetry. The twisted-mass formalism [47, 48] introduces an extra mass-like term which performs a rotation in flavour space. This additional term introduces a mass-squared like term to $M^\dagger M$ which protects the operator from troublesome exceptional configurations. The flavour rotation does however, for finite lattice spacings, break flavour and parity symmetries although these are restored in the continuum limit. There is a wide range of physics results to date obtained using the twisted-mass formalism [49–54].

Chapter 3

Ensemble Generation

3.1 Introduction

In lattice QCD we wish to calculate expectation values of operators which are functions of the gauge and fermion fields. Denoting such an operator by $\mathcal{O}[U, \overline{\psi}, \psi]$ we can write the expectation value as

$$\langle \mathcal{O}[U, \overline{\psi}, \psi] \rangle = \frac{\int \mathcal{D}U \mathcal{D}\overline{\psi} \mathcal{D}\psi e^{-S[U,\overline{\psi},\psi]} \mathcal{O}[U, \overline{\psi}, \psi]}{\int \mathcal{D}U \mathcal{D}\overline{\psi} \mathcal{D}\psi e^{-S[U,\overline{\psi},\psi]}} \tag{3.1}$$

where $\mathcal{D}U$, $\mathcal{D}\overline{\psi}$ and $\mathcal{D}\psi$ are the integration measures over the gauge and fermion fields respectively. For the remainder of this discussion we shall refer to the fields U,$\overline{\psi}$ and ψ collectively as Φ, i.e. $S[U, \overline{\psi}, \psi] \rightarrow S[\Phi]$.

The gauge-field integration measure is defined as

$$\mathcal{D}U = \prod_{x,\mu} dU(x, x + \hat{\mu}) \tag{3.2}$$

which for even a small sized lattice represents thousands of integration variables and for large lattices is of order $10^7 - 10^8$. It is clear that using standard integration techniques would represent an unreasonable amount of computational expense — indeed it is a problem ideally suited to Monte Carlo integration techniques.

3.1.1 Monte Carlo Integration

Rather than attempting to compute the integral (3.1) exactly one can generate a number of gauge configurations $\Phi_1, \ldots, \Phi_N$ on which $\mathcal{O}$ can be computed. The expectation value of $\mathcal{O}$ can then be approximated by the average of $\mathcal{O}_i$ computed over each of the N configurations Φ_i, where we weight each estimate by the configuration's Boltzmann weight

$$\langle \mathcal{O} \rangle \approx \overline{\mathcal{O}} = \frac{1}{N} \sum_{i=1}^{N} \mathcal{O}[\Phi_i] e^{-S[\Phi_i]} \quad . \tag{3.3}$$

We refer to the set of N configurations as the *gauge ensemble*, or *ensemble* for short, and the quantity $\overline{\mathcal{O}}$ as the *ensemble average* of $\mathcal{O}$. In the limit $N \to \infty$ the approximation is exact.

One could form the ensemble from gauge field configurations chosen uniformly from the entire space of possible configurations. Whilst effective in principle (and, given enough time, in practice) this is an incredibly inefficient method since the integrand of (3.1) is sharply peaked around a certain configuration. One can see that the integrands are weighted by a factor of $e^{-S[\Phi]}$ and hence configurations on which the action is large will contribute very little, and conversely for those which have small values of the action[1]. As a result of this we draw our gauge configurations from a distribution which reflects this weighting

$$P[\Phi] \propto \exp\left(-S[\Phi]\right) \tag{3.4}$$

3.1.2 Markov-Chain Monte Carlo

We consider a space of states from which we choose an initial state Φ_1. How we choose our next state (and all consequent states) varies from algorithm to algorithm and will be discussed below, however in order to reach proper equilibrium we require each algorithm to satisfy two key requirements: ergodicity and detailed balance.

Ergodicity and Detailed Balanced

In order that our algorithm properly reflects the underlying physical system we require that it is possible to reach all points of configuration space from every other point in a finite number of applications of the algorithm. This condition is known as ergodicity.

The second condition is that of detailed balance

$$P(\Phi_j \leftarrow \Phi_i)e^{-S[\Phi_i]} = P(\Phi_i \leftarrow \Phi_j)e^{-S[\Phi_i]} \tag{3.5}$$

and is essentially a statement of reversibility.

A more thorough discussion of these conditions and of the Markov-chain Monte-Carlo technique in general can be found in [55].

3.2 Algorithms for Lattice QCD

One of the key expenses we face when performing lattice QCD simulations is the computation of the fermion action. This will be a significant factor in the practicality of the algorithms which we discuss below.

[1] This is a manifestation of Feynman's principle of least action.

3.2.1 The Fermion Determinant

In equation (2.17) we showed that the fermion action could be written in terms of the quark fields ψ and $\overline{\psi}$ and the fermion matrix M. When computing functional integrals such as (3.1) we are integrating over fermionic fields which are Grassmann variables and respect rules rather different from those governing commuting numbers (see *e.g.* [4]). The fermionic contribution to the Boltzmann weight factor is now an anticommuting quantity and as such is unsuitable for use in Monte Carlo simulations. Fortunately we may use the rules governing Grassmann variables in order to show that the fermionic part of the Boltzmann integral can be written as $\det M$ which we refer to as the *fermion determinant*, *i.e.* one has integrated out the fermionic part of the action leaving a real and positive multiplicative quantity.

The computation of this determinant represents a large computational problem — despite its sparsity for typical fermion actions it is very large indeed and must be recomputed for each unique gauge configuration. In has only recently become feasible to include the effects of sea quarks by evaluating the fermion determinant — one had previously been forced to work in the *quenched approximation*, in which one sets $\det M \equiv 1$.

Pseudofermions

One can rewrite [56] the determinant as an integration over the bosonic fields ϕ and $\overline{\phi}$

$$\det M = \int \mathcal{D}\overline{\phi}\mathcal{D}\phi \exp\left(-\overline{\phi}M^{-1}\phi\right) \tag{3.6}$$

where ϕ and $\overline{\phi}$ are referred to as *pseudofermions*. The problem now is computing the product $\overline{\phi}M^{-1}\phi$, which due to the sparsity of M can be done using conjugate gradient (CG) methods [57]. CG methods require that M is positive-definite which in our case is not in general true. One can remedy this by replacing the matrix M, which describes a single fermion flavour, with the positive-definite matrix $\mathcal{M} = M^\dagger M$ describing two flavours of fermions with degenerate mass. We shall see later that this has additional benefits.

3.2.2 The Metropolis Algorithm

One of the simplest methods to generate an ensemble of configurations, due to Metropolis and Hastings [58], is to start with some initial configuration Φ_1 on which the action $S[\Phi_1]$ is computed. An update is made to this configuration, following some update strategy, in order to generate a trial configuration Φ_1' on which we compute the action $S[\Phi_1']$. The difference between these two actions $\Delta S = S[\Phi_1'] - S[\Phi_1]$ is then calculated and the trial configuration is either accepted or rejected following this simple prescription:

- If $\Delta S < 0$ then the trial configuration is accepted ($\Phi_2 = \Phi_1'$) and the algorithm returns to the update step on Φ_2.
- If $\Delta S \geq 0$ then a pseudo-random number r is generated uniformly on the interval $[0, 1]$. If $e^{-\Delta S} < r$ then the trial configuration is accepted and $\Phi_2 = \Phi_1'$, otherwise the trial configuration is rejected and $\Phi_2 = \Phi_1$.

This procedure is repeated until the desired number of configurations has been reached.

One must consider how to go about updating the gauge field. Firstly consider generating a trial configuration by updating just one link at a time. One must recompute the action on this trial configuration in order to determine ΔS and due to the form of, *e.g.* , (2.16) this requires a complete recomputation of the fermion determinant. Obviously this represents a source of great computational expense and furthermore the difference between $S[\Phi_n]$ and $S[\Phi_{n+1}]$ using this scheme will be negligible leading to a high acceptance rate and highly correlated configurations.

An alternative scheme would be to sweep through the entire lattice updating the links. Whilst it would naïvely appear that this would lead to sufficiently independent configurations it does not since the update typically leads to large values of ΔS which causes a low acceptance rate in the accept/reject step.

3.2.3 Molecular Dynamics

An alternative to randomly sweeping through the lattice would be to evolve the gauge field using classical equations of motion using techniques from molecular dynamics (MD) [59]. If one considers the coordinate to be the position in configuration space U_i and introduces a momentum field $\pi_{i,\mu}$ canonically conjugate to it then one can define the Hamiltonian for our system

$$H\left(\pi, U, \psi, \overline{\psi}\right) = \frac{1}{2}\pi^2 + S_{\text{fermion}}[U, \psi, \overline{\psi}] + S_{\text{gauge}}[U] \tag{3.7}$$

which should be conserved throughout the evolution, *i.e.* $\dot{H} \equiv 0$.

In order to evolve these coordinates through phase space one must first equip oneself with derivatives of both π and U. One does this by introducing a fictitious time coordinate τ, referred to as *molecular dynamics time*. One then integrates the expressions for $\dot{\pi}$ and $\dot{U}$ (the derivatives of π and U respectively with respect to τ) in order to evolve the coordinates (U, π).

In deriving an expression $\dot{\pi}$ one must take the derivative of the matrix kernel $\mathcal{M}$ with respect to the gauge links. For Wilson-type fermions and naïve staggered fermions this is a relatively straightforward procedure. For Asqtad however the inclusion of various

taste-symmetry improvement terms into the action makes this particularly non-trivial[2].

With these derivatives in hand one is in a position to integrate Hamilton's equations and evolve the gauge fields. One may use any area preserving integration scheme for this purpose — considering the leapfrog integrator it can be shown that it fails to conserve energy exactly; it has finite stepsize errors $\mathcal{O}(\delta\tau^2)$, where $\delta\tau$ is the integrator timestep. In order to obtain a fixed-point distribution even close to that of the physical theory one must use a very small value for $\delta\tau$ and since at each timestep one must recompute the Hamiltonian (and therefore the actions) this represents an unacceptable cost.

The MD approach as outlined so far is in principle ergodic, given a long enough evolution in MD time. One can attempt to improve the ergodicity, or at least the rate at which phase space is explored, by drawing the momenta π from a Gaussian heatbath $P(\pi) \propto \exp(-\frac{\pi^2}{2})$ [60,61] at given points in the molecular dynamics evolution (for example once per unit time τ). One may also refresh the pseudofermion fields ϕ using Gaussian noise η, such that $\phi \propto M^\dagger\eta$ where η is drawn from the distribution $P(\eta) \propto \exp(-\frac{\eta^2}{2})$.

3.2.4 Hybrid Monte Carlo

As noted above the molecular dynamics approach forces us to use very small integrator timesteps. In order to allow us to integrate on more acceptable timesteps the HMC algorithm [62] introduces a Metropolis accept/reject test at the end of each trajectory

$$P_{\text{acc}} = \min\left(1, e^{-\delta H}\right) \tag{3.8}$$

where $\delta H = H_{\text{f}} - H_{\text{i}}$ (H_{i} being the Hamiltonian at the beginning of the trajectory and H_{f} being that at the end). This accept/reject test stochastically corrects for the finite stepsize errors introduced by the integrator making the algorithm exact. This allows the integration to be performed with arbitrarily large timesteps, although in practice one must tune $\delta\tau$ such that the Metropolis acceptance rate matches the optimal acceptance for the integration scheme used. For the accept/reject test to be valid one must use a reversible and area preserving integrator — again the leapfrog integrator suffices.

By computing the fermionic part of the action using the positive-definite kernel $\mathcal{M}$ this is also what appears in the fermion force term. Since $\mathcal{M}$ represents two degenerate species of fermion the HMC algorithm fails when attempting to simulate uneven or non-integral numbers of fermions, in particular it fails for 2+1 flavour Wilson type simulations, and for all staggered simulations where the fourth-root trick has been applied to the sea quarks (see below).

[2]Indeed the situation is worse for highly-improved staggered quarks — coding the HMC force term for the HISQ action was a significant investment on behalf of UKQCD.

3.2.5 The R Algorithm

Since the fermion determinant encapsulates the number of flavours represented by the matrix M one runs into difficulties for staggered fermions — the determinant of M represents four degenerate tastes of fermion and the determinant of $\mathcal{M}$ two degenerate flavours in four degenerate tastes each. In order to reduce this multiplicity one takes the fourth-root of the determinant. This fourth-rooting procedure is a source of a great controversy surrounding the staggered fermion formalism — whilst it certainly appears to be valid in the perturbative framework, amounting to a division of each sea quark loop by four, its validity in the non-perturbative regime is disputed by both sides ([63–66] and [67–70]).

Putting such disputes aside one requires a way to treat this non-integral power of the matrix kernel $\mathcal{M}$. Since there is no analytic expression for $\mathcal{M}^{1/4}$ one cannot differentiate it with respect to its constituent gauge links in order to derive the force term. The R algorithm [71] makes use of the matrix identity that for a positive Hermitian matrix $\mathcal{M}$

$$\det \mathcal{M}^{\alpha} \equiv \exp(\alpha \mathrm{Tr} \ln \mathcal{M}) \tag{3.9}$$

which allows the determinants to be absorbed into an effective action such that one may rewrite the partition function for a theory describing 2+1 flavours of staggered fermions as

$$Z = \int \mathcal{D}U e^{-(S_{\mathrm{gauge}} - \frac{1}{2}\mathrm{Tr} \ln \mathcal{M}_{\mathrm{l}} - \frac{1}{4}\mathrm{Tr} \ln \mathcal{M}_{\mathrm{s}})} \quad . \tag{3.10}$$

The computation of the derivative of the trace in the fermionic part of the force term now involves computing the explicit matrix inverse of $\mathcal{M}$ at each step timestep of the molecular dynamics integration. One can replace this explicit inverse by using a noisy estimator of the trace which requires the computation of $\mathcal{M}^{-1}M^{\dagger}\eta$, where η is complex and Gaussianly distributed. Due to the use of a noisy estimator this algorithm is neither reversible nor energy preserving so one cannot use the accept/reject test at the end of each trajectory, making the R algorithm an inexact algorithm. With the second order leapfrog integrator the error can be shown to be $\mathcal{O}(\delta\tau^2)$.

3.2.6 Rational Hybrid Monte Carlo

In order to be able to apply HMC like algorithms to simulations of staggered fermions with 2+1 flavours it is clear that a method of approximating the matrix kernels $\mathcal{M}_{\mathrm{l}}^{1/2}$ and $\mathcal{M}_{\mathrm{s}}^{1/4}$ is required. The polynomial HMC (PHMC) algorithm [72, 73] is one such algorithm and is used extensively in Wilson type simulations [74–76] and has even been used with naïve staggered fermions [77]. However matrix polynomial approximations typically need to be of very high order to be accurate and as such introduce a great deal of computational cost into the already expensive Asqtad force term.

The pseudofermion action for 2+1 flavours of staggered fermions can be written

$$S_{\mathrm{f}} = \phi_{\mathrm{l}}^{\dagger} \mathcal{M}_{\mathrm{l}}^{-1/2} \phi_{\mathrm{l}} + \phi_{\mathrm{s}}^{\dagger} \mathcal{M}_{\mathrm{s}}^{-1/4} \phi_{\mathrm{s}} \quad . \tag{3.11}$$

The rational Hybrid Monte Carlo (RHMC) algorithm [78–80] replaces the matrix kernels with their optimal rational approximations in order to obtain

$$S_{\mathrm{f}}^{\mathrm{mc}} = \phi_{\mathrm{l}}^{\dagger} \left[r_{\mathrm{l}}^{\mathrm{mc}}(\mathcal{M}_{\mathrm{l}}) \right]^2 \phi_{\mathrm{l}} + \phi_{\mathrm{s}}^{\dagger} \left[r_{\mathrm{s}}^{\mathrm{mc}}(\mathcal{M}_{\mathrm{s}}) \right]^2 \phi_{\mathrm{s}} \tag{3.12}$$

where $r_{\mathrm{l}}^{\mathrm{mc}}$ and $r_{\mathrm{s}}^{\mathrm{mc}}$ are the rational approximations to $\mathcal{M}_{\mathrm{l}}^{-1/4}$ and $\mathcal{M}_{\mathrm{s}}^{-1/8}$ respectively — we use $[r_{\mathrm{l/s}}^{\mathrm{mc}}(\mathcal{M}_{\mathrm{l/s}})]^2$ in the action so that one is able to refresh the pseudofermion fields using the heatbath method as described earlier. These approximations must be correct to machine precision in order for the algorithm to be exact.

The rational approximations to a kernel $\mathcal{M}$ are generated using the Remez algorithm [81] and can be written in partial fraction form as

$$r(\mathcal{M}) = \alpha_0 + \sum_{k=1}^{n} \frac{\alpha_k}{\mathcal{M} + \beta_k} \tag{3.13}$$

where n is the degree of the rational approximation. For the rational approximations we will face (*i.e.* $\mathcal{M}^{\alpha}$ for $|\alpha| < 1$) the poles β_k are positive allowing us to apply the inverse of the rational approximation to the pseudofermions using a multishift solver [82, 83].

In order to perform the MD evolution we must take the derivative of (3.12). As it stands this involves using $[r_{\mathrm{l/s}}^{\mathrm{mc}}(\mathcal{M}_{\mathrm{l/s}})]^2$ resulting in twice the number of inversions per timestep. We can instead generate direct approximations $r_{\mathrm{l/s}}^{\mathrm{md}}$ to the kernels in (3.11), and due to the accept/reject test at the end of each evolution it is acceptable, and sensible, to generate these at a lower degree than the Monte Carlo approximations since the smallest pole increases with reducing approximation degree leading to fewer CG iterations per solve

$$S_{\mathrm{f}}^{\mathrm{md}} = \phi_{\mathrm{l}}^{\dagger} r_{\mathrm{l}}^{\mathrm{md}}(\mathcal{M}_{\mathrm{l}}) \phi_{\mathrm{l}} + \phi_{\mathrm{s}}^{\dagger} r_{\mathrm{s}}^{\mathrm{md}}(\mathcal{M}_{\mathrm{s}}) \phi_{\mathrm{s}} \tag{3.14}$$

3.2.7 Improved RHMC

Clark and Kennedy reformulated the RHMC algorithm in a series of papers [84, 85] in which several pre-existing techniques were applied to the specific case of staggered fermions in order to reduce the computational cost.

Mass Preconditioning

The cost of inverting the matrix kernel $\mathcal{M}$ is governed by the ratio of its largest to its smallest eigenvalue — the condition number κ. This can become large for Wilson type

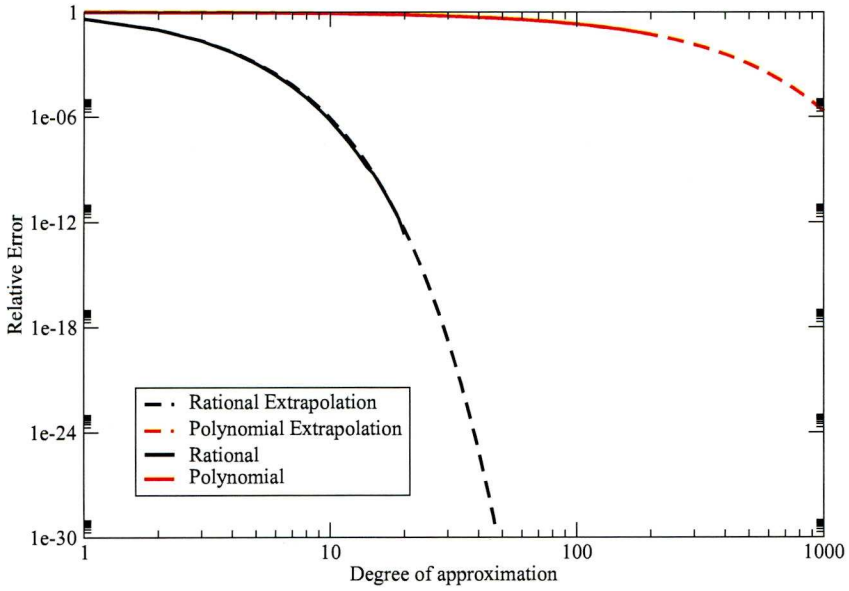

Figure 3.1: Comparison of the accuracy of the optimal rational and polynomial approximations to $x^{-1/2}$ for a spectral range corresponding to $m = 0.025$ in the staggered formalism vs their degree. Figure from [78].

formalisms where the lack of chiral symmetry results in a spectrum unbounded from below, resulting in a premature onset of the 'Berlin Wall' scenario [86–88]. Although staggered fermions are protected from this by their residual chiral symmetry it is still desirable to improve the condition number in order to approach physical pion masses with the minimum of effort.

By introducing an auxiliary matrix Q and corresponding pseudofermion field χ we can rewrite the determinant [89] of $\mathcal{M}$ as

$$\det \mathcal{M} \equiv \det(Q^\dagger Q) \frac{\det \mathcal{M}}{\det(Q^\dagger Q)} \tag{3.15}$$

where this can be computed using the usual pseudofermion method (3.6) with the pseudofermions χ and ϕ. The kernel for the pseudofermion ϕ is replaced by $Q^\dagger \mathcal{M}^{-1} Q = (MQ^{-1})^{-1\dagger}(MQ^{-1})^{-1}$, so by choosing a suitably well-conditioned Q we can improve the condition number of the matrix we must now apply to the pseudofermion field.

In the case of 2+1 flavour simulations we already have a matrix kernel and pseudofermion field corresponding to the strange quark, and since the strange quark mass is typically an order of magnitude larger than the light quark mass we can use the strange kernel to precondition the light, *i.e.*

$$\det \mathcal{M}_\mathrm{l}^{1/2} \det \mathcal{M}_\mathrm{s}^{1/4} = \left(\frac{\det \mathcal{M}_\mathrm{l}}{\det \mathcal{M}_\mathrm{s}} \right)^{1/2} \det \mathcal{M}_\mathrm{s}^{3/4} \tag{3.16}$$

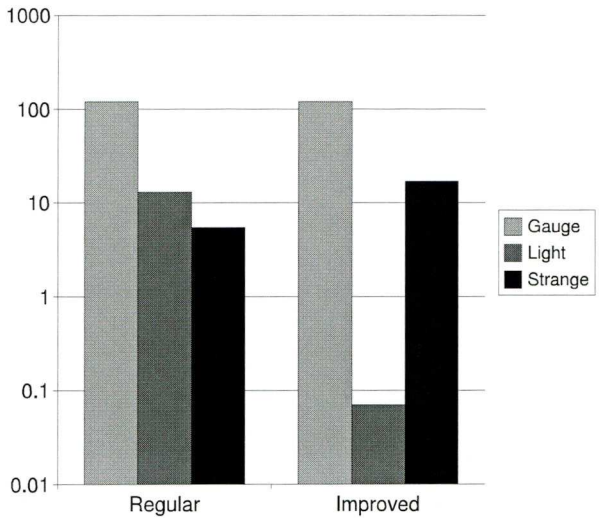

Figure 3.2: A comparison of the L_∞-norm of the force terms for the gauge field, and light and strange pseudofermions before (regular) and after (improved) preconditioning. Figure from [85] (4^4, $\beta = 6.76$ and Asqtad with $m_{l/s} = 0.01/0.05$.)

which, by using the additive mass property of the staggered kernel $\mathcal{M}_s = \mathcal{M}_l + \delta m^2$, where $\delta m^2 = 4\left(m_s^2 - m_l^2\right)$, allows us to write our pseudofermion action as

$$S_f = \phi_l^\dagger \left(\frac{\mathcal{M}_l + \delta m^2}{\mathcal{M}_l}\right)^{1/2} \phi_l + \phi_s^\dagger \mathcal{M}_s^{-3/4} \phi_s \tag{3.17}$$

where as before we use rational approximations to approximate the kernels.

When performing the integration using *e.g.* the standard second-order leapfrog integrator one has to choose the timestep such that the integration is stable under the largest contribution to the force — in this case the gauge field. Given the cost of computing the fermionic force-terms this is obviously a far from satisfactory way to proceed. One can instead split the integrator so that the evolutions occur on multiple timesteps [90], placing the gauge field on a small timestep and the fermionic fields on larger timesteps. Having preconditioned the light kernel we see from Fig. 3.2 that the force due to the light kernel is an order of magnitude less than that due to the strange kernel allowing us to place the light force integration on a long timestep and the strange force on some intermediate timestep.

Multiple-Pseudofermion Trick

By using pseudofermions to compute the determinant the estimate of the force is thereby subject to noise which can trigger instabilities in the integration earlier than

one might expect. One can trivially rewrite the determinant as

$$\det \mathcal{M} = \left(\det \mathcal{M}^{1/n}\right)^n \tag{3.18}$$

and, by introducing a separate pseudofermion field ϕ_i for each contribution, the pseudofermionic estimator of the determinant can be written

$$\det \mathcal{M} = \prod_{i=1}^{n} \int \mathcal{D}\phi_i^\dagger \mathcal{D}\phi_i \exp\left(-\phi_i^\dagger \mathcal{M}^{-1/n} \phi_i\right) \quad . \tag{3.19}$$

This is referred to in the literature as the "n^{th}-root trick".

Further Improvements

It was observed [91] that the contributions to the MD rational approximation corresponding to the lightest shifts, despite being the most expensive to invert, contributed the least to the total. In light of this it was suggested that the CG inverter tolerance be set on a shift-by-shift basis: loosened for the smallest contributions and left tight for the largest.

Having brought the integrator instability under control through the use of multiple pseudofermions and allowed the use of larger timesteps we are now able to implement higher order integrators. The finite stepsize errors introduced into the total Hamiltonian by the second-order leapfrog integrator occur at $\mathcal{O}(\delta\tau^2)$ which, in order to maintain an acceptable acceptance rate, require us to keep $\delta\tau$ small. Takaishi and de Forcrand [92] have explored the use of a class of minimum-norm (MN) integrators, developed by Omelyan *et al.* [93], in lattice QCD. Their formulation is different to the leapfrog integrator in that they explicitly minimise the finite stepsize errors allowing for accurate integrators of arbitrary order[3]. The second-order MN (2MN) integrator is shown to perform better than the second-order leapfrog (2LF) despite the extra computational cost involved per timestep. We choose to use the fourth-order minimum-norm integrator with five force evaluations (4MN5FV, where the V indicates that we integrate over the momentum field first) as advocated in [84].

3.2.8 Tuning the RHMC Algorithms

In order to make use of the various improvements described above a great deal of tuning must be carried out. There are many degrees of freedom to consider, namely[4]:

- The gauge stepsize and the (possibly different) fermionic stepsizes

[3] This is in contrast to the normal constructions of higher order leapfrog integrators which are built by recursing the leapfrog integrator.

[4] There is one remaining degree of freedom which is how often to perform the accept reject test (i.e. the value of τ)

- The integrator used
- The number of extra pseudofermion fields used in the n^{th}-root trick (i.e. the value of n)
- The approximation degrees for both the molecular dynamics evolution and the Metropolis test
- The CG tolerances per shift

This is worsened by the fact that the Hamiltonian is extensive in the volume somewhat limiting our ability to perform meaningful tests on small lattices. As noted above we choose to fix the integrator and use the 4MN5FV, and also fix the number of pseudofermion fields used for the strange kernel to 3 (both as in [84]).

Our key requirement in implementing the improvements was that the time taken for the generation of a $24^3 \times 64$ configurations should reduce, based on an expected speed up of 50%. We attempted a series of small volume (4^4) test runs but found the parameters carried poorly across to the larger lattices, as one might expect from the extensivity of the Hamiltonian and the sensitivity of the acceptance to $\delta\tau$. These were however instructive in determining how best to perform the tuning.

After several iterations of tuning on the $24^3 \times 64$ lattices we achieved no more than a speed up of 16% (there were a number of parameter sets which gave larger absolute improvements but at the cost of decreased acceptance). An outline of the parameters used for the generation of the fine ensemble is given below.

- A timestep of $\tau/\delta\tau = 6$, for $\tau = 1$, was used. The integrators were embedded such that the gauge was on a timestep of $\frac{1}{3}\delta\tau$ and the fermions on a timestep of $\delta\tau$.
- The molecular dynamics rational approximation for the light quarks were computed with 5 poles, whilst that for the triple strange was computed with 6 poles. The higher order approximations for the accept/reject test are computed with 6 and 10 poles for the light and strange respectively.
- Tuning the residual tolerances on a per-pole was found to be reasonably ineffective for the light quarks[5], whilst for the strange MD approximation the zeroth and first poles were set to a tolerance of 10^{-5}, with the higher poles having tolerances $\sim 10^{-7}$.

[5]Indeed since in Fig. 3.3 the light quark is shown to have a lower overall L_∞ norm this is hardly surprising.

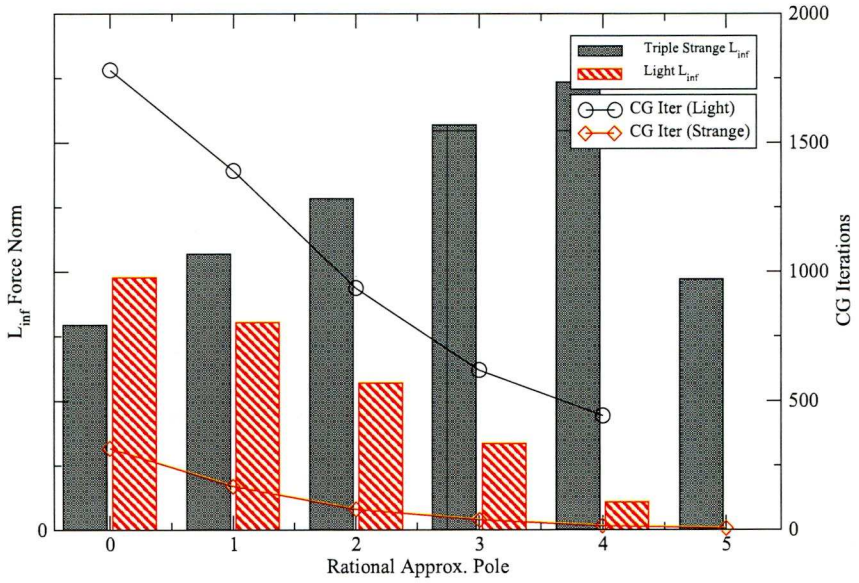

Figure 3.3: The L_∞ force for each pole of the rational approximation and the number of CG iterations required. $24^3 \times 64$ lattice, $am_{l/s} = 0.006/0.03$.

Whilst we do not have measures of the fermionic forces before the change in parameters we show the L_∞ norm of the contributions to the fermionic forces from each pole of the rational approximations in Fig 3.3. The triple-strange force, integrated over all poles, seems to be considerably higher than the light force which is consistent with expectations and Fig. 3.2

3.3 Ensembles

In order to study singlet quantities on the lattice a large number of configurations is required due to their sensitivity to gluonic and fermionic noise. Central to attaining accurate determinations of singlet quantities is the generation of ensembles containing a large number of molecular dynamics trajectories. We have chosen our initial physics parameters such that our physical results should be directly comparable to those from the MILC collaboration once finite-stepsize errors due to their use of the R-algorithm are taken into account. It is for this reason we have chosen to use RHMC — with such a large number of molecular dynamics trajectories the stepsize using the R-algorithm would have to be prohibitively small. We have generated the ensembles detailed in Table 3.1 using the UKQCD's QCDOC [94] and refer to them as the *coarse* and *fine* ensembles. The plaquette and acceptance for the duration of the fine run are shown against the molecular dynamics trajectory in Fig. 3.4

	N_f	β	$L^3 \times T$	$am_{l/s}$	am_π	N_{cfg}	N_{traj}
Coarse	2+1	6.75	$24^3 \times 64$	0.006/0.03	0.183(1)	5237	31422
Fine	2+1	7.095	$32^3 \times 64$	0.00775/0.031	0.1632(7)	2867	17202

Table 3.1: UKQCD Asqtad Ensembles generated for the scalar and pseudoscalar singlet studies

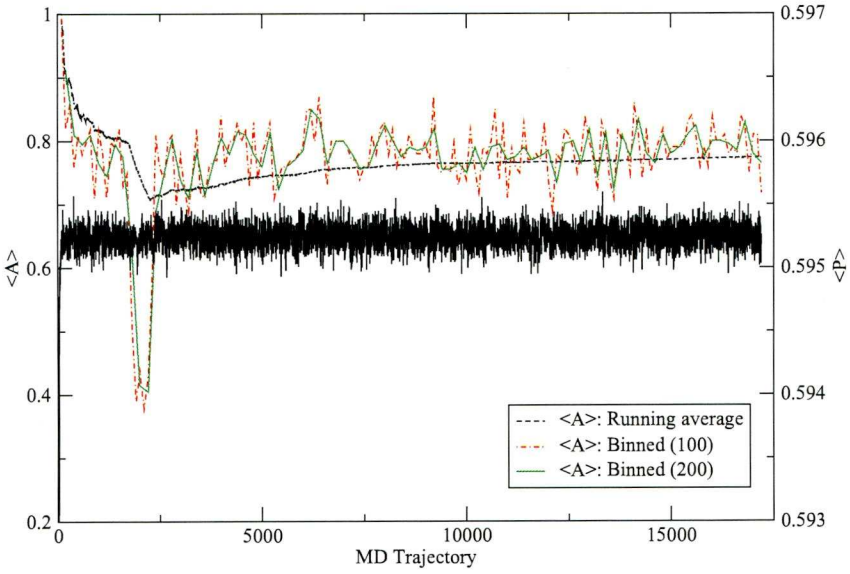

Figure 3.4: The acceptance, unbinned and binned (100 trajectories per bin and 200 trajectories per bin), and the average spacetime plaquette versus the molecular dynamics trajectory. A dip in acceptance is observable $\sim$ trajectory 1600 due to a change in the molecular dynamics timestep

3.4 Setting the Scale

When we use the lattice as a method of regularising our field theory we introduce the lattice spacing a as a cutoff for the theory. This corresponds directly to an energy scale and in order to extract physical quantities from the lattice we must determine this energy scale. In principle this can be done by comparing quantities such as the hyperfine splitting of the charmonium system to predictions from lattice perturbation theory [95], although in our case this requires the costly computation of states in which we have little direct interest. A more common method is to use the static quark potential to determine the lattice spacing.

3.4.1 Static Quark Potential

The potential between a pair of infinitely heavy static quarks and antiquarks is well modelled by phenomenological approaches to hadron physics [96–98]. The form of the

effective potential used [99] is

$$V(\vec{r}) = C + \sigma r + \frac{\alpha}{r} \tag{3.20}$$

where r is the separation of the quark and antiquark and σ is the 'string tension' corresponding to the linear behaviour of the potential at large r. In actions where rotational invariance is severely damaged one can include a term $V_{\text{tree}}(\vec{r})$ modelled on the tree-level one gluon exchange propagator in order to correct for these violations. However in the case of the one-loop tadpole improved Lüscher-Weisz gauge action rotational symmetry violations are found to be relatively weak [100] and as such we do not consider such corrections.

Furthermore when dynamical quarks are taken into account there are complications at large r related to string breaking effects. Studies have been performed [101] in which a basis of both gluonic and mesonic operators is used in order to detect such effects. Whilst we do not attempt to study this phenomenon directly we are conscious of its existence and therefore limit our fit range such that it can be safely neglected.

In a procedure following [99] we measure the potential on the lattice by measuring Wilson loops of various sizes (both on- and off-axis). The gauge field is iteratively smeared using 16 applications of the APE smearing technique [35] in order to obtain a 2×2 basis for a variational analysis.

Wilson loops of dimension $R \times S \times T$ (where R and S are the on-axis and off-axis spatial dimensions of the loop and T is its length in the temporal direction) can be written in terms of the static quark potential $V(r)$ ($r = \sqrt{R^2 + S^2}$) as

$$W(R, S, T) = \sum_i C_i(r) \exp(-V_i(r)T) \tag{3.21}$$

The potential $V(r)$ can then be computed via the large-time limit of the ratio

$$V_{\text{eff}}(R, S, T) = -\ln \frac{W(R, S, T+1)}{W(R, S, T)} \tag{3.22}$$

i.e.

$$V(r) = \lim_{T \to \infty} V_{\text{eff}}(R, S, T) \tag{3.23}$$

Non-planar loops (those with $S \neq 0$) are used to obtain values for non-integer r which provide more fitting points. Also, since there are certain (different) values of (R, S) that give the same value for r, we may use the static quark potential as a measure of rotational invariance violations.

Sommer [102] introduced the definition $r_0^2 F(r_0) = 1.65$, where $F(r) = \frac{dV}{dr}(r)$. The solution r_0 corresponds to a physical distance of ~ 0.5 fm. This can be a large source of systematic error as the physical value of r_0 is not particularly well defined — it

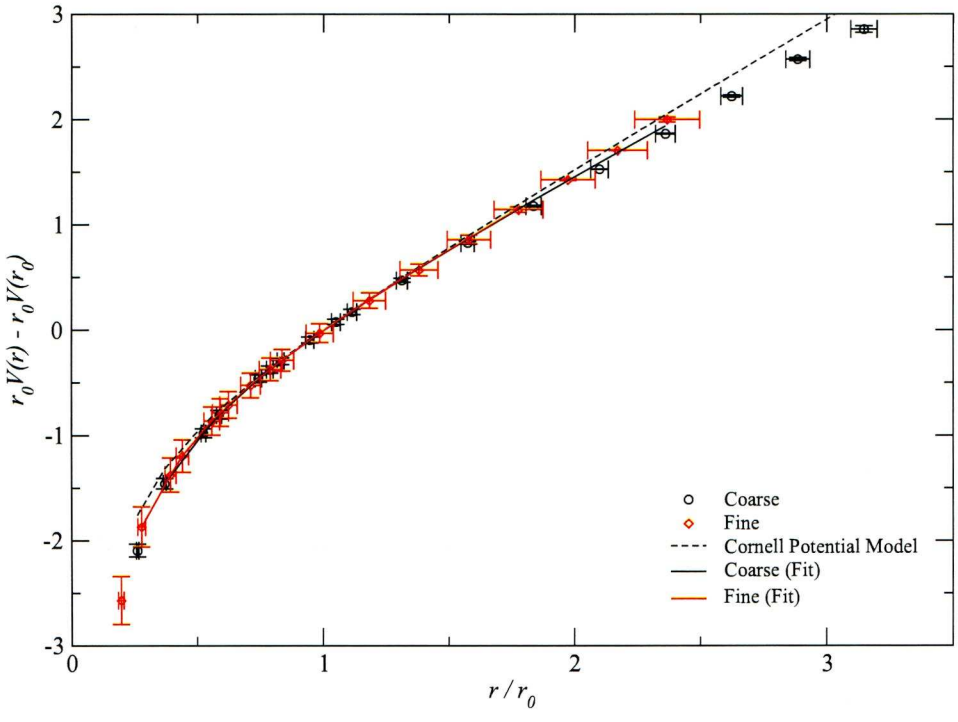

Figure 3.5: $(V(r) - V(0))\, r_0$ vs $\frac{r}{r_0}$ for the fine and coarse lattices. The dotted line corresponds to the predictions of the Cornell phenomenological potential model and the solid lines to fits to (3.20) for both the coarse and fine measurements.

is taken to be within the range 0.45 — 0.5 fm, the uncertainty due to the use of different phenomenological models as well as sea quark effects. In principle one can use any solution of $r^2F(r) = c$ (where c is constant) to set the scale, indeed the MILC collaboration use the quantity r_1 (defined by $r_1^2F(r_1) = 1$) instead of r_0 [100] citing a lower relative error in their determination of the spacing. We have, however, stuck with the majority of the literature and use r_0 with a choice of 0.467 fm as the physical value to set the scale.

Our determinations of r_0/a and the lattice spacings a are presented for both the coarse and fine ensembles in Table 3.2 and the static quark potentials for both are shown in Fig. 3.5. The lattice spacings obtained are close to the MILC ensembles with which we aim to compare.

Ensemble	r_0/a	a [fm]
Coarse	3.8122(74)	0.12250(24)
Fine	5.059(10)	0.09231(18)

Table 3.2: Measurements of r_0/a and the lattice spacing a, determined using $r_0^{\text{phys}} = 0.467$ fm.

Chapter 4

Data Analysis

Once one has generated an ensemble or several ensembles of configurations and has measured quantities of interest one must extract the best possible estimate of the physical observable to which they correspond. Intrinsic to this analysis is the extraction of a meaniningful estimate of the uncertainty; this is perhaps one of the most artful parts of lattice QCD as whilst one wishes their mass estimate, for example, to be as accurate as possible this must be balanced against the cost of having generated the ensemble in the first place.

4.1 Error Estimation

Due to our necessarily finite number of configurations there will be a *statistical error* associated with any quantitity measured using these lattices. For a quantity which is a function of the gauge fields such as the average plaquette P, a so called *primary variable*, one can estimate the sample mean and the sample variance using the standard formulae

$$\overline{\mathcal{O}} = \frac{1}{N_{\text{cfg}}} \sum_{i=1}^{N_{\text{cfg}}} \mathcal{O}_i \tag{4.1}$$

and

$$\sigma^2 = \frac{1}{N_{\text{cfg}} - 1} \sum_{i=1}^{N_{\text{cfg}}} \left(\mathcal{O}_i - \overline{\mathcal{O}}\right)^2 \tag{4.2}$$

where the use of $N_{\text{cfg}} - 1$ instead of N_{cfg} in the variance corrects for the bias introduced by the finite sample size. One can then compute the *standard error on the mean* $\overline{\mathcal{O}}$, ϵ using

$$\epsilon = \frac{\sigma}{\sqrt{N_{\text{cfg}}}} \quad . \tag{4.3}$$

4.1.1 Resampling Techniques

In the case of secondary variables which are functions of the means of primary variables we are restricted having a single estimate of the quantity over the entire ensemble. For a concrete example we take the effective mass (§4.3) defined as

$$am_{\text{eff}} = \ln \frac{C(t)}{C(t+1)} \quad . \tag{4.4}$$

Since the correlator C is only meaningful when we look at the mean over the entire ensemble this restricts us to a single estimate of the effective mass thus equation (4.2) is no longer applicable. Instead one applies resampling techniques [103] in order to obtain estimates of the variance of the mean — the most often used being the single-elimination jackknife and bootstrap methods.

In the single-elimination jackknife procedure one builds a set of N_{cfg} biased estimates $x_{J,i}$ of the quantity x by eliminating the contribution from a single randomly selected configuration to the primary variable and computing the secondary variable $x_{J,i}$ on the jackknife sample. From this set one can compute the biased mean

$$\overline{x}_J = \frac{1}{N_{\text{cfg}}} \sum_{i=1}^{N_{\text{cfg}}} x_{J,i} \tag{4.5}$$

and the jackknife estimate of the variance

$$\sigma_J^2 = \frac{N_{\text{cfg}}}{N_{\text{cfg}}-1} \sum_{i=1}^{N_{\text{cfg}}} (x_{J,i} - \overline{x}_J)^2 \quad . \tag{4.6}$$

The bootstrap method is rather similar in spirit to the jackknife method. One constructs N_{BS} biased estimates $x_{B,i}$ of the quantity x by constructing pseudoensembles of N_{cfg} randomly selected configurations from the entire set of N_{cfg} configurations and measuring x on each of these. Again, one computes the biased mean

$$\overline{x}_B = \frac{1}{N_{\text{BS}}} \sum_{i=1}^{N_{\text{BS}}} x_{B,i} \tag{4.7}$$

and the bootstrap estimate of the variance

$$\sigma_B^2 = \frac{1}{N_{\text{BS}}-1} \sum_{i=1}^{N_{\text{BS}}} (x_{B,i} - \overline{x}_B)^2 \quad . \tag{4.8}$$

In order to obtain a reasonable estimate of the variance one typically chooses $N_{\text{BS}} \approx 100$.

One should note for both the jackknife and bootstrap estimates of variance that this is actually the variance of the mean, rather than the variance of the data sample about the mean, and therefore the standard error on the mean ε is simply given by σ_J

rather than by an application of equation (4.3). There is very little difference between the two methods in terms of results but where computational effort is required, for example in cases where one must recompute the vacuum subtraction on a resample by resample basis, the bootstrap method is preferred due to the typically smaller number of resamplings required.

4.1.2 Systematic vs. Statistical Errors

We have discussed the methods for determining the statistical errors above but the majority of quantities which one computes on the lattice carry with them *systematic errors*. These can stem from attempting to convert lattice quantities into physical units, usually due to uncertainty in the value of a determined using the methods described in Section 3.4, or may be due to a fundamental uncertainty in the analysis — for example sensitivity to fit ranges, etc. In cases where chiral extrapolations are performed there are systematic issues pertaining to the model used to perform the extrapolation, similar issues arising in the case of continuum and infinite volume extrapolations.

In Chapters 5 and 6 where quantities are given with a single error, e.g. $am = 0.0554(21)$, this is taken to be the statistical error — in this particular example a central value of $am = 0.0554$ with a statistical error of 0.0021. Where systematic errors are included their origins will be explained.

4.2 Autocorrelations

As hinted at in Section 3.2 consecutive configurations can be highly correlated due to the nature of the evolution algorithm employed. Thus, when one measures physical observables on these lattices these too will show correlation in molecular dynamics time, which we refer to as *autocorrelation*.

The formula for calculating the variance presented in (4.2) assumes that each measurement is independent of every other measurement — in cases where autocorrelations are present this will be a biased estimate (it will be systematically lower). One can attempt to correct for this bias by measuring the autocorrelation function

$$\rho(\tau) = \frac{1}{N_{\text{cfg}}} \sum_{\tau'=1}^{N_{\text{cfg}}-\tau} \left(\mathcal{O}(\tau') - \overline{\mathcal{O}}\right)\left(\mathcal{O}(\tau'+\tau) - \overline{\mathcal{O}}\right) \quad , \tag{4.9}$$

where τ is the position in molecular dynamics time, from which we can compute the *integrated autocorrelation time* $\tau_{\text{AC}}^{\text{int}}$:

$$\tau_{\text{AC}}^{\text{int}} = 1 + 2\sum_{\tau=1}^{N_{\text{cfg}}} \left(1 - \frac{\tau}{N_{\text{cfg}}} \frac{\rho(\tau)}{\rho(0)}\right) \tag{4.10}$$

which allows us to compute the true variance σ^2 from the naïve variance σ^2_{naive} using

$$\sigma^2 = \tau^{\text{int}}_{\text{AC}} \sigma^2_{\text{naive}} \quad . \tag{4.11}$$

Of course, due to the definition of the autocorrelation function in (4.9), $\tau^{\text{int}}_{\text{AC}}$ is different for different observables. This is partially due to algorithmic issues — for instance some algorithms [104] explore topological sectors rather slowly and thus topological quantities, such as the topological charge Q have long autocorrelation times.

One can attempt to remove the bias due to the autocorrelations without computing the autocorrelation time by blocking the data. Rather than taking the variance of an observable to be the variance over all measurements one blocks or *bins* the measurements from n_b successive configurations into a single bin (where the value of the binned measurement is the mean of its elements). One can now compute the variance of the binned measurement and observe its behaviour as one increases n_b — the variance should plateau at the true variance, although unfortunately since the uncertainty on σ increases with n_b this is a self limiting process.

4.3 Effective Mass

In cases where the correlator has a well-defined groundstate which is split from the first excited state by an appreciable gap the *effective mass*[1]

$$am_{\text{eff}}(t) = \ln \frac{C(t)}{C(t+1)} \tag{4.12}$$

is a useful quantity to study.

Due to the form of the correlation function one can show that

$$am_{\text{eff}}(t) \overset{t\to\infty}{\longrightarrow} am_0 \quad , \tag{4.13}$$

where m_0 is the mass of the ground-state contributing to the correlator. This asymptotic behaviour can be observed as a plateauing of the effective mass and the success of this method is strongly dependent on a number of factors. Firstly we require that the state of interest is indeed the groundstate — this is often not the case when studying states with open decay channels where the groundstate is the total mass of the lightest decay products. Secondly noise limits how far in time we can extend our effective mass and thus we require the excited states contribution to the correlation function to decay more rapidly than that of the groundstate. In cases where the splitting between m_1 and m_0 is small the efficacy of this method is lessened.

[1] Note for the purposes of this discussion we will presume that we are dealing with momentum-zero states unless otherwise specified.

Furthermore for states in which the signal to noise ratio of the correlator is poor one often finds that the effective mass gives way to noise before exhibiting any clear plateauing. One can ameliorate this situation by using anisotropic lattices in which $a_t \ll a_s$ (where a_t and a_s are the temporal and spatial lattice spacings respectively). This provides an improved resolution in the temporal direction without introducing further finite volume effects, allowing one to perform more accurate fits before losing the signal to noise. There is a strong history of using anisotropic lattices for glueball studies in the quenched approximation [105–107] and progress is being made in dynamical studies [108].

4.3.1 Weighted Average

In order to extract an estimate of the mass from the plateau region of the effective mass we compute the *weighted average* of the effective mass over the plateau region. The weighted average of $am_{\text{eff}}(t)$ over the region $[t_1, t_2]$ is defined as

$$\overline{am} = \frac{\sum_{t=t_1}^{t_2} w(t) am_{\text{eff}}(t)}{\sum_{t=t_1}^{t_2} w(t)} \tag{4.14}$$

where $w(t) \doteq \frac{1}{\varepsilon(t)}$, $\varepsilon(t)$ being the standard error on the mean $am_{\text{eff}}(t)$. Whilst it is possible to use the weights to define the variance of $\overline{am}$ [109] we found this to be an unreliable method and chose instead use the bootstrap method in order to determine the variance.

4.4 Variational Method

In cases where one has a basis of different operators measured on individual timeslices $\mathcal{O}_i(t)$ one can form a matrix of correlators $C_{ij}(t) = \langle \mathcal{O}_i(\tau)\mathcal{O}_j(\tau + t)\rangle$ (where we presume any vacuum contributions have been dealt with). Whilst great effort goes into constructing optimal interpolating operators it is unlikely that our operators $\mathcal{O}_i$ form a truly optimal basis for the space of states we wish to study. The *variational method* [110, 111] is used extensively in the literature to improve this basis, particularly in the cases of baryon spectroscopy [112], charmonium studies [113] and studies of excited states [114, 115]. The variational method is primarily used in glueball studies [110, 116–118] in order to project out the groundstate as accurately as possible and have typically been unable to obtain accurate estimates of the second contributing state.

The variational method consists of finding the eigenvectors u_i, u_j which maximise

$$u_i C_{ij}(t) u_j \tag{4.15}$$

for a fixed

$$u_i C_{ij}(t_0) u_j \quad . \tag{4.16}$$

One can show that this leads to the generalised eigenvalue problem (GEVP)

$$C_{ij}(t)u_j^\alpha(t,t_0) = \lambda^\alpha C_{ij}(t_0)u_j^\alpha(t,t_0) \quad \text{for } t > t_0 \tag{4.17}$$

where $\alpha = 0 \ldots N-1$, $\alpha = 0$ corresponding to the ground state; one must choose appropriate values of t and t_0 at which to solve the GEVP (which we call 'setting the basis'). For certain classes of improved actions, such as the construction given in §2.3.2, the transfer matrix is no longer Hermitian and one must take care to avoid setting the basis at small (t, t_0) where the contributions due to the imaginary eigenvalues are non-negligible. Lüscher and Weisz [12] have shown that for sufficiently large times one can still consider the spectral decomposition of the transfer matrix without difficulties. Of course we come full circle here — since we solve the eigenvalue problem by taking the inverse of $C_{ij}(t_0)$ one cannot choose t_0 too large without the inversion becoming numerically unstable so one typically chooses $t_0 \sim 1, 2$ whilst bearing the above caveat in mind.

One can construct a new matrix of variational correlators $\bar{C}_{\alpha\beta}$ using these eigenvectors

$$\bar{C}_{\alpha\beta}(t) = u_i^\alpha C_{ij}(t) u_j^\beta \tag{4.18}$$

where the element $\bar{C}_{00}(t)$ corresponds to the groundstate correlator, $\bar{C}_{11}(t)$ to the first excited, etc. Since the eigenvectors provide an orthogonal basis for C_{ij} at t and t_0 the matrix $\bar{C}_{\alpha\beta}$ is diagonal at these times. One can show that the eigenvalues obtained are related to the mass by

$$\lambda^\alpha(t,t_0) = e^{-m_\alpha(t-t_0)} \tag{4.19}$$

where one can compute leading order corrections to this [111] by setting the basis at various t values and observing the variation of the eigenvalues.

One can use the variational eigenvalues to define an *eigenvalue extrapolated effective mass* — by modelling the correlator as a sum of two exponentials [119] one can use the ratio of the first and zeroth eigenvalues in order to reduce the contamination, resulting in

$$am_0(t) \approx \frac{a\bar{m}_{\text{eff}}(t) - a\frac{\lambda^1}{\lambda^0}\bar{m}_{\text{eff}}(t-1)}{1 - \frac{\lambda^1}{\lambda^0}} \tag{4.20}$$

where $a\bar{m}_{\text{eff}}(t)$ is the effective mass defined in (4.12) with $\bar{C}_{00}(t)$ substituted for $C(t)$. This model relies on the assumption that the contribution of the excited state to the correlator is small and as such is not always applicable.

In practice there are states propagating backwards in time with a contribution $\sim e^{-m_i(T-t)}$. Whilst these are not expected to cause a problem in the case of glueball spectroscopy – one loses the signal to noise before they can be resolved – they can be clearly observed in the spectroscopy of the π, ρ etc. and therefore one must set the

basis before the backward propagating state's contribution becomes significant [120]. Furthermore in spectroscopy using staggered fermions there is a further artefact due to the staggered fermion construction which introduces a parity partner whose contribution oscillates in time — in this case one cannot apply the variational method without first removing the oscillating contribution.

4.5 Fitting

In cases where it is not possible to extract an accurate mass estimate using the effective mass technique one must seek to obtain estimates directly from the correlation function itself. One can do this by performing a fit to the correlation function using some model function. We choose the form

$$\mathcal{C}(\rho, t) = \sum_{i=0}^{N-1} A_i e^{-m_i t} \tag{4.21}$$

to reflect the physical correlation function where the amplitudes A_i can be considered as the overlap of our operators with the transfer matrix eigenstate with mass m_i, and one chooses the value of N such that one is attempting to include all physical states likely to contribute significantly in the chosen fitting region yet is not overparameterising the fit based on the number of data points avaliable to us; in order to have confidence in our mass estimate one typically wishes to include at least one state above the state of interest when this is possible.

We must now use our data in order to determine the set of parameters $\rho = \{A_0, m_0, \ldots, A_{N-1}, m_{N-1}\}$ which best describes our data. In order to do this we define the correlated-χ^2 statistic as

$$\chi^2 = \sum_{t,t'=t_{\text{min}}}^{t_{\text{max}}} (\mathcal{C}(\rho, t) - \overline{C}(t)) N V_{tt'}^{-1} (\mathcal{C}(\rho, t') - \overline{C}(t')) \tag{4.22}$$

where $V_{tt'}^{-1}$ is the inverse of the covariance matrix $V_{tt'}$

$$V_{tt'} = \frac{1}{N_{\text{cfg}} - 1} \sum_{i=1}^{N_{\text{cfg}}} \left(C_i(t) - \overline{C}(t)\right) \left(C_i(t') - \overline{C}(t')\right) \tag{4.23}$$

and in a slight abuse of notation $\overline{C}$ corresponds to the mean correlator defined via (4.1) rather than the variational correlator as defined in (4.18).

By minimising (4.22) with respect to our parameters ρ we obtain a set of parameters that are deemed to describe our data well — a value of $\chi^2 \approx n_{\text{dof}}$, where n_{dof} is the number of data points used minus the number of independent parameters, is deemed acceptable. A detailed discussion of fitting correlated data is given in [121, 122].

In general one wishes the fit parameters, corresponding to physical amplitudes and masses as they do, to be stable with respect to both the time range over which one fits and the operators used to form the correlators. To address the first point one usually plots the mass of the state of interest at fixed t_{max} whilst varying t_{min} — a plateau here indicates that the state we are observing truly is the groundstate and contamination from the next states is minimised.

Choosing an appropriate value of N in (4.21) is, as mentioned, critical to obtaining a good fit: if one chooses N too small then there are not enough degrees of freedom to resolve the physics of the system properly; on the other hand if one chooses N too large then there are too many degrees of freedom and the fit becomes unstable, often resorting to choosing unphysical or degenerate masses. Since the fitting range is limited by the quality of data available so too is the maximum possible value of N — for example if one can only fit up to $t = 8$ then one can choose N no greater than 3.

4.6 Factorising Fitting

By fitting to several correlators simultaneously one can extend the amount of data available to resolve the fit parameters. One can write the correlation function as a sum over transfer matrix eigenstates

$$\begin{aligned} C_{ij}(t) &= \langle 0 \,|\mathcal{O}_j(\tau + t)\mathcal{O}_i(\tau)|\, 0\rangle \\ &= \sum_{\alpha} \langle 0 \,|\mathcal{O}_j(\tau + t)|\, n\rangle \langle n \,|\mathcal{O}_i(\tau)|\, 0\rangle e^{-m_\alpha t} \end{aligned} \tag{4.24}$$

thus one can consider the physically motivated fitting matrix

$$[F(t)]_{ij} = f_{ij}(t) = \sum_{\alpha=0}^{N-1} c_i^\alpha c_j^\alpha e^{-m_\alpha t} \tag{4.25}$$

where we have truncated the infinite sum over eigenstates to a sum over N and c_i^α is the overlap of the operator $\mathcal{O}_i$ with the α^{th} state. One then performs the usual chi-squared minimisation where all overlaps and masses are determined simultaneously. This procedure is referred to as a *factorising* or *multichannel* fit.

Since there will be correlations between the correlators formed from different combinations of operators as well as between those on different timeslices we must now define our covariance matrix as

$$V_{\alpha\beta;\alpha'\beta';tt'} = \frac{1}{N_{\text{cfg}} - 1} \sum_{i=1}^{N_{\text{cfg}}} \left(C_{\alpha\beta}(t) - \overline{C}_{\alpha\beta}(t)\right) \left(C_{\alpha'\beta'}(t') - \overline{C}_{\alpha'\beta'}(t')\right) \tag{4.26}$$

and our correlated-χ^2 correspondingly as

$$\chi^2 = \sum_{\alpha\beta;\alpha'\beta'} \sum_{tt'=t_{\text{min}}}^{t_{\text{max}}} \left(C_{\alpha\beta}(\rho, t) - \overline{C}_{\alpha\beta}(t)\right) N V^{-1}_{\alpha\beta;\alpha'\beta';tt'} \left(C_{\alpha'\beta'}(\rho, t') - \overline{C}_{\alpha'\beta'}(t')\right) \quad . \tag{4.27}$$

A discussion of the utility of this method will be given on a case by case basis.

Chapter 5

Glueball Measurement

5.1 Introduction

The non-abelian nature of the $SU(3)$ gauge group used in QCD introduces non-vanishing gluon field interactions in the latter part of (1.10) which are predicted [123], in the strong coupling limit, to manifest themselves as colour-singlet bound states — *glueballs*. Some of the earliest pure gauge (*i.e.* simulations in which fermionic degrees of freedom are ignored completely) simulations of both $SU(2)$ and $SU(3)$ lattice gauge theory focussed on the spectrum of these glueball states [36, 116, 118, 124, 125], finding $M_G(0^{++})$ in the range $1.5-1.7$ GeV. While there is no *a priori* reason that the glueball spectrum of pure gauge $SU(3)$ should agree with that of fully dynamical lattice QCD — dynamical quarks mix the glueball with the mesonic states — we take this as a guide. Thus when we aim to study the 'glueball' spectrum in fully dynamical QCD we are actually studying the spectrum of glue-rich states which for convenience we refer to as glueballs.

The current experimental status of glueballs is unclear; there are a number of experiments actively engaged [126] or soon to be become engaged [127, 128] in the study of glueballs but as with lattice QCD studies results are complicated by strong mixing effects. The primary method for identifying glueball candidates is by observing their production in glue-rich decay channels, such as the decays of J/ψ. Detailed reviews of the situation are given in [129, 130].

The most commonly considered phenomenological scenario is that the three generally accepted 0^{++} states between 1 and 2 GeV are caused by the mixing of two $q\overline{q}$ meson states with a scalar glueball. Of the three observed[1] isoscalar 0^{++} states in this region — $f_0(1370)$, $f_0(1500)$ and $f_0(1710)$ — the $f_0(1710)$ is thought to be an $s\overline{s}$ state, due to its dominant decay into $K\overline{K}$ and its absence in $p\overline{p}$ annihilation. The $f_0(1370)$ decays predominantly into multi-π final states and thus is thought to be primarily $u\overline{u} + d\overline{d}$.

[1] There is a fourth state, the $f_0(1790)$, claimed by BES [131] but it is unobserved elsewhere and is not yet recognised by the PDG [132].

Whilst in recent years the availability of teraflop and petaflop supercomputers has meant that the production of fully dynamical ensembles has become widespread in the lattice QCD community [74,133,134] these ensembles have mainly focussed on accessing a wide range of quark masses, lattice spacings and volumes in order to fully explore chiral extrapolations, lattice artefacts and finite-size effects and as such the statistics, whilst fine for the purpose, are lower than is necessary to clearly measure the glueball spectrum.

As described in chapter 3 we have generated two fully dynamical ensembles with large statistics and pion masses $2 - 2.5$ times heavier than the physical pion mass. These near-physical pion masses allow a realistic chance for studying glueball decay into two pseudoscalars (particularly the $\pi\pi$ channel) and it is hoped the large number of configurations in each ensemble will allow for an accurate determination of the vacuum subtraction as well as fits to larger times.

Furthermore the pseudoscalar glueball has received scant attention in recent years as quenched lattice studies showed it to be heavy ($M > 2.0$ GeV) [106, 125]. Recent phenomenological mixing studies [135,136] predict its mass to be much lower, ~ 1.4 GeV — this is close to the mass of the $\eta(1405)$, formerly known as ι and a strong pseudoscalar glueball candidate [137, 138]. It is therefore important to measure the pseudoscalar glueball mass with fully dynamical ensembles.

5.1.1 Unquenching Effects on the Scalar Glueball

As mentioned the inclusion of dynamical quarks in our simulations causes mixing between the glueball states of pure gauge $SU(3)$ and $q\overline{q}$ states. An interesting question is how strong is this mixing and how does it effect the masses of the states we observe. There have been several studies of glueballs in dynamical QCD with inconsistent results.

One particular phenomenon that was observed in early dynamical lattice QCD studies of the glueball spectrum [117] was a large reduction in the mass of the scalar glueball accompanied by a minimal change in the mass of the tensor glueball when compared to quenched studies. This phenomenon is referred to as the scalar dip and has been explained [117] as being due to the clover term introducing an effectively adjoint piece to the action, enhancing the strength of an already present bulk phase transition [139] in the fundamental-adjoint plane of the Wilson gauge action. A more recent study using clover fermions with an improved gauge action in which the strength of the phase transition is expected to be reduced showed a similar reduction in the scalar glueball mass [140] which the authors argue is not due to the phase transition. A recent study using staggered fermions [141] showed results more consistent with those of quenched simulations.

It is evident that the effects of unquenching on the scalar glueball mass are far from understood and therefore we hope that the use of high statistics will allow us to get an accurate determination of the scalar glueball mass with dynamical quarks to be compared with quenched measurements.

5.2 Glueball Operators

Since the $SO(4)$ rotational invariance of the continuum theory is broken to the cubic rotation group O_h by the lattice discretisation procedure the operators which we must construct to study glueballs on the lattice lie in particular irreducible representations (irreps) of this group. A thorough treatment of this involved topic is given in [116] and as such we shall only give an overview.

5.2.1 0^{++} Operators

In order to study the 0^{++} glueball we construct operators using a combination of Wilson loops which is invariant under the A_1^{++} irrep[2] of O_h. The simplest such combination is the sum of spatial plaquettes P_4 over all spatial planes, *i.e.*

$$\mathcal{O}_i^{A_1^{++}}(\mathbf{p},t) = \mathrm{Tr}\sum_{\vec{x}}\left(P^i_{4,xy}(\vec{x},t) + P^i_{4,yz}(\vec{x},t) + P^i_{4,zx}(\vec{x},t)\right)e^{\frac{2\pi i}{L}\mathbf{p}\cdot\vec{x}} \tag{5.1}$$

where the Fourier transform ensures that our operator couples to the state with the correct definite momentum (in this study we will consider $|\mathbf{p}| = 0$ and $|\mathbf{p}| = 1$ states only) and the superscript i refers to the Teper-blocking level, as described below.

The construction given in (5.1) is the simplest operator satisfying the requirements of being invariant under both parity and charge conjugation, as well as having the correct rotational symmetries. However by using elementary plaquettes we have a limited projection onto the glueball wavefunction — the plaquettes have a spatial extent equal to the lattice spacing (in this study ~ 0.1fm), and studies have shown [142] that the 0^{++} glueball wavefunction has an effective radius $r_0 \sim 0.3$fm ($r_0 \sim 0.6$fm for the 2^{++}). This, as well as decreasing the vacuum noise, motivates us to extend our basis of operators by using the Teper blocking procedure [36]. We denote the n-times blocked plaquette P_4 by P_4^n.

5.2.2 Teper Blocking

This procedure was developed precisely for the reasons outlined above. It consists of increasing the extent of the glueball operator's spatial extent whilst maintaining the spatial density of links (in contrast, for example, to using plaquettes of increasing size

[2] Actually the O_h irrep is A_1^+ (where this positive refers to evenness under parity conjugation) and the additional positive in the text above refers to the state's evenness under charge conjugation.

on an unblocked lattice). The blocking procedure is rather simple and is easily carried out iteratively — indeed one achieves better results by blocking a number of times as demonstrated in [36].

The links on an $N+1$ times blocked lattice are formed from those of an N times blocked lattice by combining the product of 2 spatial "links" (since on an already blocked lattice these are rather complicated structures) and the sum of the spatial staples, *i.e.*

$$U_\mu^{N+1}(x) \leftarrow P\Bigg[U_\mu^N(x)U_\mu^N(x+\hat{\mu}) + \sum_{\substack{\pm\nu\neq\mu \\ \nu\neq 4}} U_\nu^N(x)U_\mu^N(x+\hat{\nu})U_\mu^N(x+\hat{\nu}+\hat{\mu})U_\nu^{N\dagger}(x+2\hat{\mu})\Bigg] \tag{5.2}$$

where the operation P denotes projection back onto the nearest element of $SU(3)$ (this projection is not carried out in [36]). As with APE smearing we do not block in the temporal direction as we wish to keep the structure of the transfer matrix intact. Each application of the blocking procedure reduces the number of useable links in the spatial directions of the lattice by a factor of two which limits the number of times the procedure can be applied.

5.2.3 2^{++} Operators

To study the tensor 2^{++} state we construct operators which are invariant under either of the doubly degenerate E_1^{++} and T_2^{++} irreps. We choose the E_1^{++} irrep which allows for the use of basic plaquettes and form 2 combinations of spatial plaquettes:

$$\mathcal{O}_i^{E_1^{++}}(t) = \mathrm{Tr}\sum_{\vec{x}}\left(P_{4,xy}^i(\vec{x},t) - P_{4,yz}^i(\vec{x},t)\right) \tag{5.3}$$

and

$$\mathcal{O}_i'^{E_1^{++}}(t) = \mathrm{Tr}\sum_{\vec{x}}\left(P_{4,xy}^i(\vec{x},t) + P_{4,yz}^i - 2P_{4,zx}^i(\vec{x},t)\right) \quad . \tag{5.4}$$

Note that here we do not include the Fourier factor as we did for the 0^{++} operators as the boosting causes mixing between the E_1 and T_2 irreps.

5.2.4 0^{-+} Operators

In order to study the pseudoscalar glueball (or indeed any parity negative state) we require an operator which flips under a parity inversion to an operator which cannot be obtained by rotations alone. We can immediately see that this is not possible using planar operators such as the plaquettes above as they are incapable of capturing the behaviour of the third axis under a flip of a single axis. We must instead use non-planar

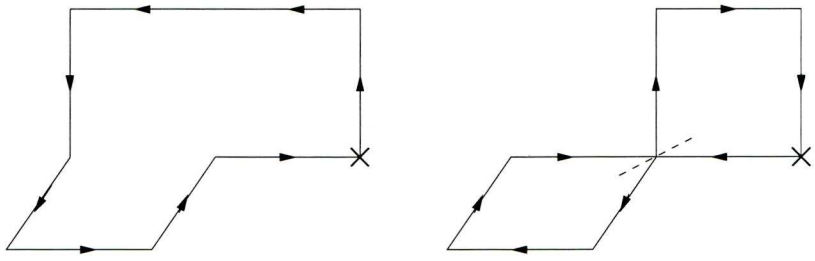

Figure 5.1: Schematics of the hand (left) and butterfly (right) operators which can be used to study the pseudoscalar glueball.

operators with an intrinsic handedness such as the hand and butterfly loops shown in Fig. 5.1.

For technical reasons we choose to use the hand operator only, which we denote by H_8. As H_8 is parity-odd we must make the distinction between the left-handed and right-handed versions and we do this by adding L and R to the subscript, respectively.

Obtaining parity-oddness is not the end of the story, however — we must now ensure that we combine our $H_{8,\{L,R\}}$ correctly in order to obtain the correct A_1 rotational symmetry. This is done similarly to $\mathcal{O}^{A_1^{++}}$, and we obtain our pseudoscalar glueball operator

$$\begin{aligned}\mathcal{O}_i^{A_1^{-+}}(t) = \mathrm{Tr}\sum_{\vec{x}}\Big(&\left(H^i_{8,L,xy}(t) + H^i_{8,L,yz}(t) + H^i_{8,L,zx}(t)\right)\\ &- \left(H^i_{8,R,xy}(t) + H^i_{8,R,yz}(t) + H^i_{8,R,zx}(t)\right)\Big) \ .\end{aligned} \tag{5.5}$$

We can also use our H_8 loops to construct A_1^{++} operators by considering our parity-even requirement. Pairing this with the fact that $H_{8,R} = \mathcal{P}\left(H_{8,L}\right)$ we can simply flip the sign on the $H_{8,R}$ term of equation 5.5 in order to obtain an alternative A_1^{++} operator

$$\begin{aligned}\mathcal{O}_i'^{A_1^{++}}(t) = \mathrm{Tr}\sum_{\vec{x}}\Big(&\left(H^i_{8,L,xy}(t) + H^i_{8,L,yz}(t) + H^i_{8,L,zx}(t)\right)\\ &+ \left(H^i_{8,R,xy}(t) + H^i_{8,R,yz}(t) + H^i_{8,R,zx}(t)\right)\Big) \ .\end{aligned} \tag{5.6}$$

5.2.5 Torelon Operators

On a periodic spatial lattice tubes of colour-flux can wrap around the spatial torus and form closed loops. At low temperature these states will be stable and are referred to as *torelons*, with a mass given by

$$am_\tau = a^2\sigma L - \frac{\pi}{3L} \ . \tag{5.7}$$

We can use Polyakov loops as interpolating operators for these states as has been done in previous studies [117,143]. However, given the spatial extent of our lattices the mass

of the torelon will be far greater than that of the groundstate scalar glueball and as such we consider them no further.

5.2.6 Spin Ambiguity

In the continuum where the full Lorentz group exists a spin-zero state is invariant under rotation through any angle θ about its spatial axes. However, as has been discussed, symmetries of the full Lorentz group are broken to a discrete subgroup on the lattice — the smallest rotation one can perform is one of $\frac{\pi}{2}$ about its spatial axes. It becomes evident on the lattice that a spin-4 state will be indistinguishable from a spin-zero state — that is to say the operator in equation (5.1) is invariant under the $\frac{\pi}{2}$ rotations that we would usually use to define a spin-4 state. In the case of the $PC = ++$ states we know from Regge trajectory arguments that the lightest 0^{++} is lighter than the lightest 4^{++} state so we do not expect that they will be confused in our fits. However it has been pointed out that the lightest 4^{-+} state is in fact lighter than the lightest 0^{-+} state [144] and this could lead to a misidentification of spin in the pseudoscalar sector. Constructions that introduce further approximate symmetries (which become exact in the continuum limit) to our operators have been developed [145] in order to differentiate between ambiguous states, however we choose not to employ them.

5.2.7 Measured Operators

We have measured the scalar glueball operator $\mathcal{O}^{A_1^{++}}$ as defined in (5.1) at four levels of Teper blocking (0,1,2 and 3), where the Teper blocking has been applied to a gauge field which has been APE smeared twice with $c = 2.5$ (thus the operators $\mathcal{O}_0^{A_1^{++}}(t)$ are measured on this APE smeared field) for both the coarse and fine lattices at both $|\vec{p}| = 0$ and $|\vec{p}| = 1$. The tensor operators $\mathcal{O}^{E_1^{++}}$ and $\mathcal{O}'^{E_1^{++}}$ have been measured using the same parameters, although on a subset of the ensemble.

The pseudoscalar operators $\mathcal{O}^{A_1^{-+}}$ and the alternative scalar operators $\mathcal{O}'^{A_1^{++}}$ have been measured at Teper blocking levels 0,1 and 2 (as discussed in §5.2.2 the doubling of "link" length with each application limits the number of applications) where again the gauge field has first been APE smeared twice with a smearing parameter $c = 2.5$. Again, these have been measured on a subset of the ensemble.

5.3 Structure of the Analysis

We will first present the analysis for the scalar glueball operators on the coarse lattices. This will be performed in several ways: by studying the effective mass as defined in (4.12); the effective mass computed using the variational correlators (which for convenience we label the *variational effective mass*); by studying the eigenvalues obtained

from the solution of the generalised eigenvalue problem (4.17); and by performing factorising fits to various bases of operators. This will be performed for both $|\vec{p}| = 0$ and $|\vec{p}| = 1$ correlators and will be followed by a similar analysis for the fine scalar glueball operators. Finally we will present the results for our pseudoscalar and tensor glueball operators on both the coarse and fine lattices.

5.4 Effective Mass Results

In Fig. 5.2 we show the effective mass as defined in (4.12) computed using a basis of the scalar glueball operators $\mathcal{O}^{A_1^{++}}$ at 4 levels of Teper blocking on the coarse lattices, along with the averages obtained by computing the weighted average between $t = 2 - 5$ on the diagonal entries of the matrix of correlators corresponding to $\mathcal{O}_2^{A_1^{++}}$ and $\mathcal{O}_3^{A_1^{++}}$ respectively; the values obtained are presented in Table 5.1. There appears to be a systematic difference between the estimates obtained using the 2×2 and the 3×3 correlators, although the large statistical errors on each mean that the estimates are statistically compatible.

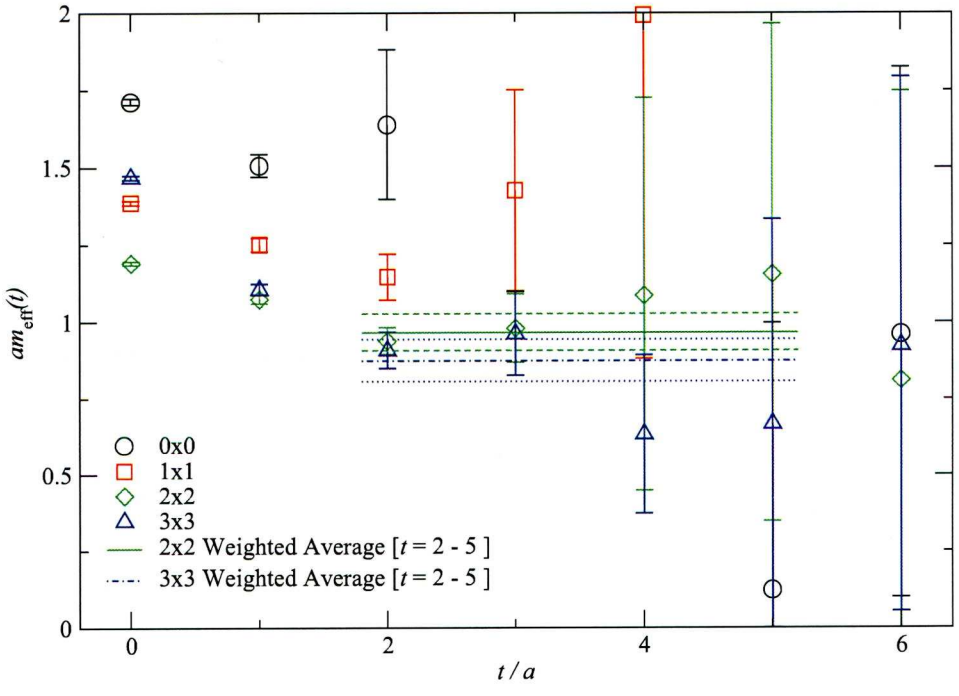

Figure 5.2: The effective mass for the diagonal entries of a 4×4 matrix of correlators formed using the $|\vec{p}| = 0$ operators $\mathcal{O}_i^{A_1^{++}}$ defined in (5.1), measured on the coarse lattices. The weighted averages for blocking levels 2 and 3 are shown, computed from $t = 2 - 5$.

In an attempt to study the dependence of the mass estimate on our choice of blocking level we present the weighted averages computed for different combinations of

operators (*i.e.* different blocking levels for the $\mathcal{O}^{A_1^{++}}$ operators) as well as over different t ranges in Fig. 5.3. There appears to be a dependence on the choice of operators used, the data showing an almost monotonic decrease in the weighted average as one increases the level of blocking at a fixed time range. This is not completely unexpected — the coupling of the lower blocking levels to excited states is likely to be larger by construction[3] and as such the plateau of their effective masses will onset later, if at all. This effect is clear in Fig. 5.2 where one can see that the effective masses of the 0×0 and 1×1 correlators fail to plateau before falling into noise.

Operators	t	am_{eff}
2×2	$2 - 5$	0.966(59)
2×2	$3 - 5$	1.01(13)
2×2	$3 - 6$	0.99(14)
3×3	$2 - 5$	0.875(69)
3×3	$3 - 5$	0.82(15)
3×3	$3 - 6$	0.83(12)

Table 5.1: Effective masses obtained from the weighted average of the effective mass computed using the correlator formed using the $|\vec{p}| = 0$ operators $\mathcal{O}^{A_1^{++}}$ measured on the coarse lattices. The blocking level combination is given in column one, and the averaging window in column two.

The dependence on the weighted averaging range appears to be weaker than the dependence on the basis — Figs. 5.3(a), 5.3(b) and 5.3(c) all show similar qualitative behaviour. In order to remove this dependence on basis we perform the variational projection as described in Section 4.4 in order to project out the eigenstates to which the operators couple.

5.4.1 Variational Effective Masses

Whilst we may use the varational method in order to project into an optimal basis of operators one must choose where to perform this projection, introducing a further degree of freedom. As discussed in Section 4.4 one must take care when performing this projection at small t/t_0 when certain improved gauge actions, including the Lüscher–Weisz gauge action, are used.

The effective masses for the variational ground state correlator $\bar{C}_{00}(t)$ where the projection has been performed at $t/t_0 = 1/0$, $2/1$ and $3/2$ are presented[4] in Fig. 5.4 along with the weighted averages for various t ranges for the $2/1$ projection. There appears to be minimal difference for the $2/1$ projection if one compares the qualitative behaviour to that observed in Fig. 5.2. For the $3/2$ projection the errors on the effective

[3] Or rather, lack thereof.

[4] For the $3/2$ projection we use $\bar{C}_{11}(t)$ since, as will be discussed, $\bar{C}_{00}(t)$ seems to correspond to a lower lying state.

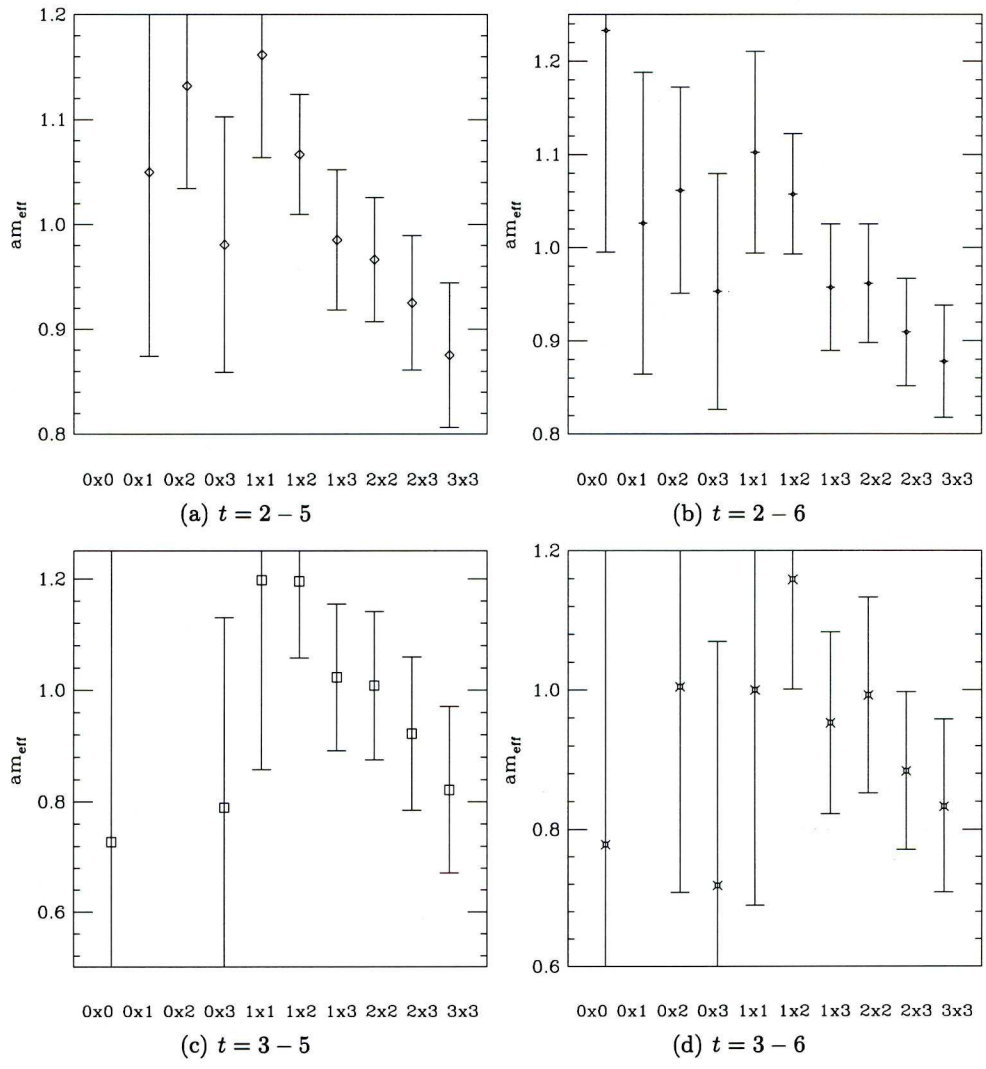

Figure 5.3: Weighted averages of the effective masses computed from the correlation functions $C_{ij}(|\vec{p}| = 0, t)$ computed using the scalar operators $\mathcal{O}_{i,j}^{A_1^{++}}(|\vec{p}| = 0)$ on the coarse lattices. $i \times j$ is used to denote the blocking level combination. The weighted averages are performed over different t ranges as specified in each subfigure caption.

mass are so large as to make the estimate consistent with zero which we believe to be due to an unstable variational projection. This is not unexpected, as discussed in Section 4.4, and one can see that this is indeed the case by studying the distribution of the eigenvalues obtained from the solution of the GEVP (4.17).

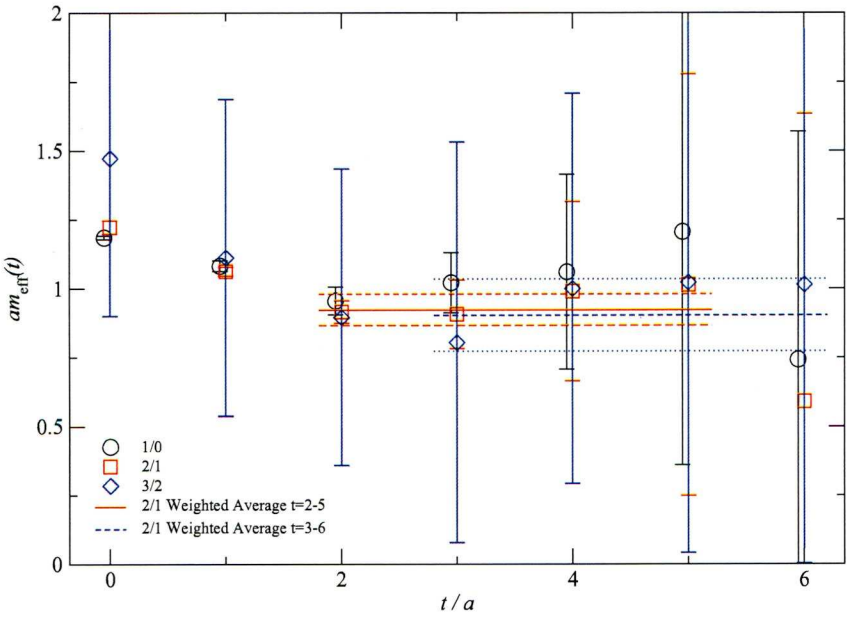

Figure 5.4: Effective masses computed using the variational correlator as defined in (4.18) for different choices of t/t_0, projecting from a 4×4 matrix of correlators constructed using $\{\mathcal{O}_0^{A_1^{++}}, \mathcal{O}_1^{A_1^{++}}, \mathcal{O}_2^{A_1^{++}}, \mathcal{O}_3^{A_1^{++}}\}$ measured on the coarse lattices with $|\vec{p}| = 0$. The effective masses for the 1/0 and 2/1 projections use $\bar{C}_{00}(t)$ whereas for the 3/2 projection we use $\bar{C}_{11}(t)$. The weighted averages are shown for the 2/1 projection, computed from $t = 2 - 5$ and $t = 3 - 6$ with the errors computed using a bootstrap procedure with $N_{\rm BS} = 50$.

In Table 5.2 we present the eigenvalues obtained from the solution of (4.17) for a 4×4 matrix of correlators formed using the basis of operators $\{\mathcal{O}_0^{A_1^{++}}(\vec{0}, t), \mathcal{O}_1^{A_1^{++}}(\vec{0}, t), \mathcal{O}_2^{A_1^{++}}(\vec{0}, t), \mathcal{O}_3^{A_1^{++}}(\vec{0}, t)\}$, with the errors computed using the variance of λ^α over 50 bootstrap samples. We can see that for the $t/t_0 = 1/0$ and 2/1 projections the eigenvalues up to and including λ^2 are reasonably well determined. For the 3/2 projection however not only is λ^0 inconsistent with the determinations from the 1/0 and 2/1 projections, but the errors are large and λ^1 is poorly determined. Of course one expects that λ^0 should change as one moves out in time since the eigenvalues reflect the spectral structure of the transfer matrix at the point at which the projection is performed — if the correlators which we use to solve (4.17) involve significant excited state contributions (beyond what can be accommodated comfortably by a 4×4 basis) then the eigenvalues are going to be artificially low and only when these excited states contribute less will we obtain satisfactory estimates of the eigenvalue spectrum.

One can follow a similar argument that if the correlators contain contributions from low lying states, *e.g.* a $\pi\pi$ state from the decay of a glueball, then one will only be able to fit this into our basis of states once excited state contributions are negligible — indeed this could be what we are observing for the 3/2 projection where λ^0 corresponds to a mass of $am_0 = 0.26(12)$ (*cf.* $2am_\pi = 0.366(2)$), however the large error and poor determination of the remaining eigenvalues do not allow us to draw firm conclusions.

t/t_0	λ^0	λ^1	λ^2	λ^3
1/0	0.2996(60)	0.132(25)	0.061(34)	0.042(37)
2/1	0.3371(68)	0.165(26)	0.114(33)	0.029(45)
3/2	1.30(43)	0.43(44)	0.06(47)	-2.03(64)
2/0	0.1023(21)	0.021(12)	0.006(14)	0.001(15)
3/0	0.0399(9)	0.0053(50)	0.0004(57)	-0.0031(62)
3/1	0.1384(29)	0.0769(93)	0.002(19)	-0.048(26)
4/2	6(3)	0(3)	0(3)	-2(3)

Table 5.2: Eigenvalues obtained from the solution of the GEVP at the specified t/t_0. Coarse 4×4 basis of $|\vec{p}| = 0$ $\mathcal{O}^{A_1^{++}}$ operators.

Basis Experimentation

If the poor determination of the eigenspectrum and thus of the variational effective mass for large bases of operators is due to attempting to resolve a large eigenspace using noisy data then one ought to look at trying to resolve smaller eigenspaces. To this end we perform a variational analysis using a 3×3 matrix of correlators formed using the operators $\{\mathcal{O}_0^{A_1^{++}}, \mathcal{O}_2^{A_1^{++}}, \mathcal{O}_3^{A_1^{++}}\}$, concentrating on the eigenvalue spectrum and present the results in Table 5.3. It is apparent that not only is the distribution of the eigenvalues narrower for the 3/2 projection using the 3×3 matrix but also the determination of λ^1 seems reliable. Furthermore since $\lambda^1(3,2) \approx \lambda^0(2,1)$ this lends credence to our argument that by performing the projection at larger t/t_0 pairs one may be observing decay products. The variational weighted average for the 2/1 projection on this basis of operators computed between $t = 2 - 5$ is presented in Fig. 5.5, where the error on the weighted average of the 3/2 projection, computed between $t = 2 - 4$ are rather large due to the need to use the first excited state correlator.

t/t_0	λ^0	λ^1	λ^2
1/0	0.2994(60)	0.119(27)	0.061(35)
2/1	0.3383(69)	0.152(27)	0.099(35)
3/2	0.522(21)	0.349(33)	-0.28(12)

Table 5.3: Eigenvalues obtained from the solution of the GEVP at the specified t/t_0. Coarse 3×3 matrix of correlators formed using $\{\mathcal{O}_0^{A_1^{++}}, \mathcal{O}_2^{A_1^{++}}, \mathcal{O}_3^{A_1^{++}}\}$ for $|\vec{p}| = 0$.

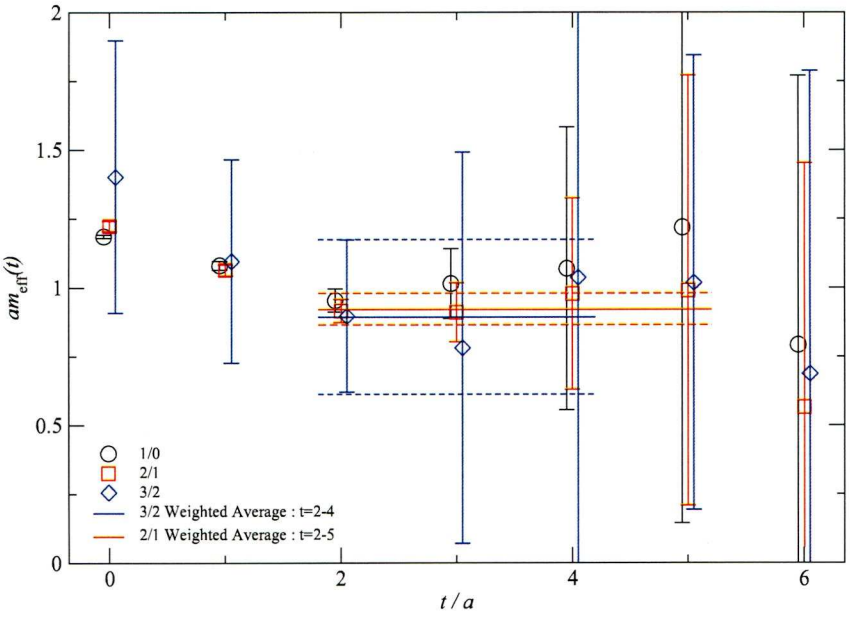

Figure 5.5: Effective masses computed using the variational correlator as defined in (4.18) for different choices of t/t_0, projecting from a matrix of correlators constructed using $\{\mathcal{O}_0^{A_1^{++}}, \mathcal{O}_2^{A_1^{++}}, \mathcal{O}_3^{A_1^{++}}\}$ measured on the coarse lattices with $|\vec{p}| = 0$. The effective masses for the $1/0$ and $2/1$ projections use $\bar{C}_{00}(t)$ whereas the $3/2$ projection uses $\bar{C}_{11}(t)$. The weighted averages are shown for the $2/1$ and $3/2$ projections, computed between $t = 2-5$ and $t = 2-4$ respectively. All errors are computed using a bootstrap procedure with $N_{\rm BS} = 50$.

5.5 Effective Mass Results: $|\vec{p}| = 1$

When computing the scalar glueball correlators one must bear in mind that there is a significant contribution from the vacuum. One can either take this into account when fitting by including an additive constant or, as is more often carried out, perform a vacuum subtraction; this is necessary if one wishes to study effective masses but can be a source of physical noise. Furthermore the vacuum contribution is large and thereby numerical errors may creep in. The vacuum subtraction is only necessary for the $|\vec{p}| = 0$ operators and as such by studying the $|\vec{p}| = 1$ correlators we sidestep these issues.

5.5.1 $|\vec{p}| = 1$ Correlators

When studying correlators of boosted operators one is studying a boosted spectrum and therefore the masses extracted by whatever means are in fact energies. In order to estimate the masses from these energies one must use the dispersion relation; one can either use the continuum dispersion relation [4] or the lattice dispersion relation

$$a^2 E^2(\mathbf{p}) = a^2 m^2 + \sum_{\mu=1}^{3} \sin^2\left(\frac{2\pi p_\mu}{L}\right) \quad . \tag{5.8}$$

Since we are working with large spatial extents and choose only to study states with $|\vec{p}| \leq 1$ where the difference between the continuum and lattice dispersion relations is negligible we choose, following [117] and [146], to use the lattice dispersion relation (5.8). For convenience we will refer to the effective energies as effective masses except where to do so would cause confusion, indeed in most cases we present the effective mass such that a comparison with the $|\vec{p}| = 0$ results can be made readily.

We present the weighted averages of the effective masses for correlators of $\mathcal{O}_i^{A_1^{++}}(|\vec{p}| = 1)$ and $\mathcal{O}_j^{A_1^{++}}(|\vec{p}| = 1)$ at different blocking levels with $i = j$ in Table 5.4. A subset of these are presented in Fig. 5.6. The reduction in the weighted average of the the effective mass between the 2×2 and 3×3 correlators, observed for the $|\vec{p}| = 0$, is less evident here although the increased statistical errors would mask any effect there may be. The $|\vec{p}| = 0$ and $|\vec{p}| = 1$ results are shown side by side in Fig. 5.7.

Operators	t	aE_{eff}	am_{eff}
1×1	$2-5$	1.01(16)	0.98(17)
1×1	$2-6$	1.01(16)	0.98(17)
2×2	$2-5$	0.98(11)	0.95(11)
2×2	$2-6$	0.96(11)	0.92(12)
2×2	$3-5$	0.86(24)	0.82(25)
2×2	$3-6$	0.82(23)	0.78(24)
3×3	$2-5$	1.02(16)	0.99(17)
3×3	$2-6$	0.98(18)	0.94(19)
3×3	$3-5$	0.90(38)	0.86(40)
3×3	$3-6$	0.81(39)	0.77(41)

Table 5.4: Effective masses obtained from the weighted average of the effective mass computed using the correlator formed using the $|\vec{p}| = 1$ scalar operators $\mathcal{O}^{A_1^{++}}$ measured on the coarse lattices. The blocking level combination is given in column one, and the averaging window in column two.

5.5.2 Variational Effective Masses

As with the momentum-zero effective masses we should look at the variational results in order to project out the groundstate. The variational effective masses for different projections using the basis of operators $\{\mathcal{O}_0^{A_1^{++}}, \mathcal{O}_1^{A_1^{++}}, \mathcal{O}_2^{A_1^{++}}, \mathcal{O}_3^{A_1^{++}}\}$ are presented in Fig. 5.8 along with the weighted average between $t = 1$ and 4 for the projection performed at $t/t_0 = 2/1$. Again we face potential stability issues — the 3/2 projection is not shown since the first two contributing states are low lying states and the statistical error on the third is large, such that for $t > 1$ the effective mass is statistically consistent with zero. By examining the eigenvalue distribution one can show that the projection is indeed unstable for the 3/2 projection.

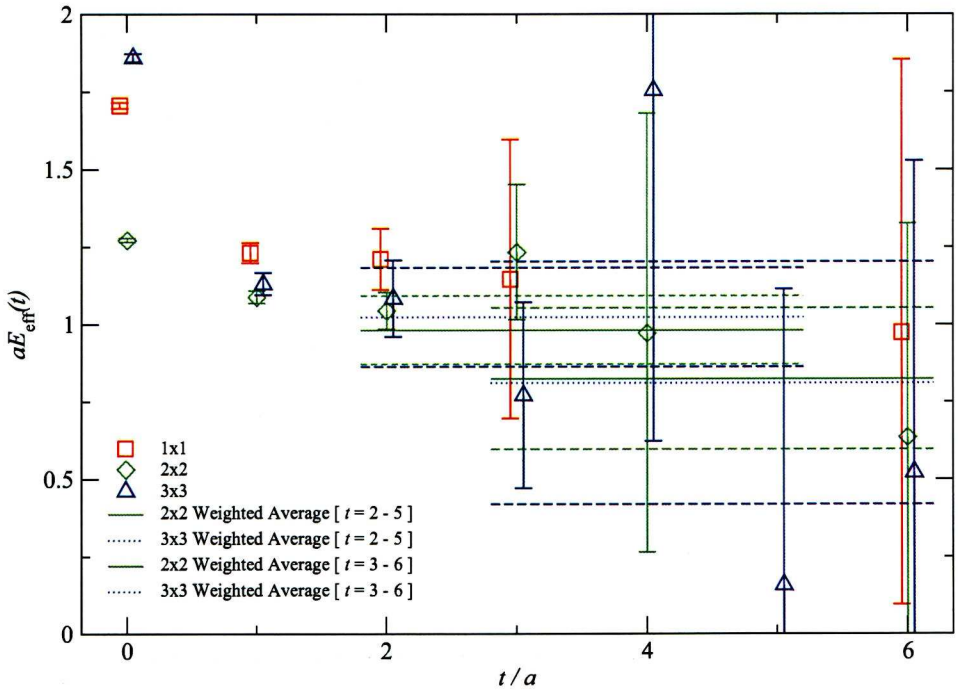

Figure 5.6: The effective mass for the diagonal entries of a 4×4 matrix of correlators formed using the $|\vec{p}| = 1$ operators $\mathcal{O}_i^{A_1^{++}}$ defined in (5.1), measured on the coarse lattices. The weighted averages for blocking levels combinations 2×2 and 3×3 are shown, computed from $t = 2 - 5$ and $t = 3 - 6$.

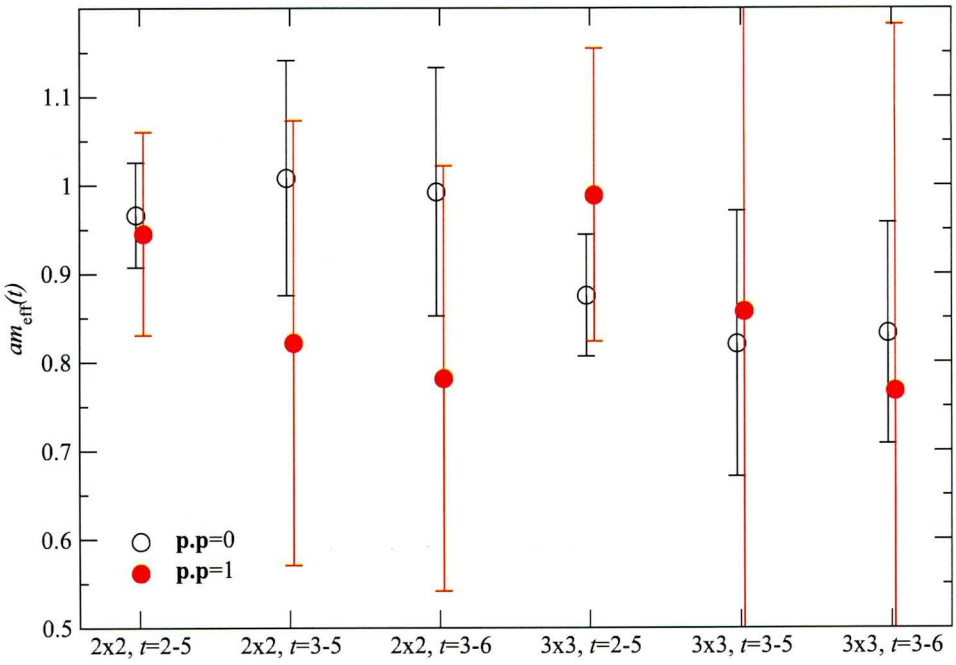

Figure 5.7: A comparison of the weighted averages of the effective masses computed using the 2×2 and 3×3 correlators of $\mathcal{O}_i^{A_1^{++}}$ at both $|\vec{p}| = 0$ and $|\vec{p}| = 1$. The labels denote the blocking levels and weighted averaging range used.

Basis Experimentation

We have experimented using smaller bases of operators in order to improve the variational projection. In the case of the $|\vec{p}| = 1$ operators the $\{\mathcal{O}_1^{A_1^{++}}, \mathcal{O}_2^{A_1^{++}}, \mathcal{O}_3^{A_1^{++}}\}$ basis was found to be the most stable, compared to $\{\mathcal{O}_0^{A_1^{++}}, \mathcal{O}_2^{A_1^{++}}, \mathcal{O}_3^{A_1^{++}}\}$ for the $|\vec{p}| = 0$; there is no *a priori* reason that the optimal basis should be the same for non-zero and zero-momentum operators. The eigenvalue spectra for the variational projections using this basis, performed at different values of t/t_0, are presented in Table 5.5.

t/t_0	λ^0	λ^1	λ^2
1/0	0.2715(55)	0.087(27)	0.031(35)
2/1	0.3175(67)	0.188(21)	0.112(31)
3/2	0.596(54)	0.286(70)	-0.10(12)

Table 5.5: Eigenvalues obtained from the solution of the GEVP at the specified t/t_0. Coarse 3×3 basis of $\{\mathcal{O}_1^{A_1^{++}}, \mathcal{O}_2^{A_1^{++}}, \mathcal{O}_3^{A_1^{++}}\}$ for $|\vec{p}| = 1$.

The eigenvalues obtained from the projection of the $|\vec{p}| = 0$ basis $\{\mathcal{O}_0^{A_1^{++}}, \mathcal{O}_2^{A_1^{++}}, \mathcal{O}_3^{A_1^{++}}\}$ and the $|\vec{p}| = 1$ basis $\{\mathcal{O}_1^{A_1^{++}}, \mathcal{O}_2^{A_1^{++}}, \mathcal{O}_3^{A_1^{++}}\}$ are converted into masses using (4.19) and (5.8) and are presented in Fig. 5.9. There is a strong consistency between the $|\vec{p}| = 0$ and $|\vec{p}| = 1$ eigenvalues corresponding to the ground and excited states for all projections shown. Furthermore for the 3/2 projection the first excited mass is consistent

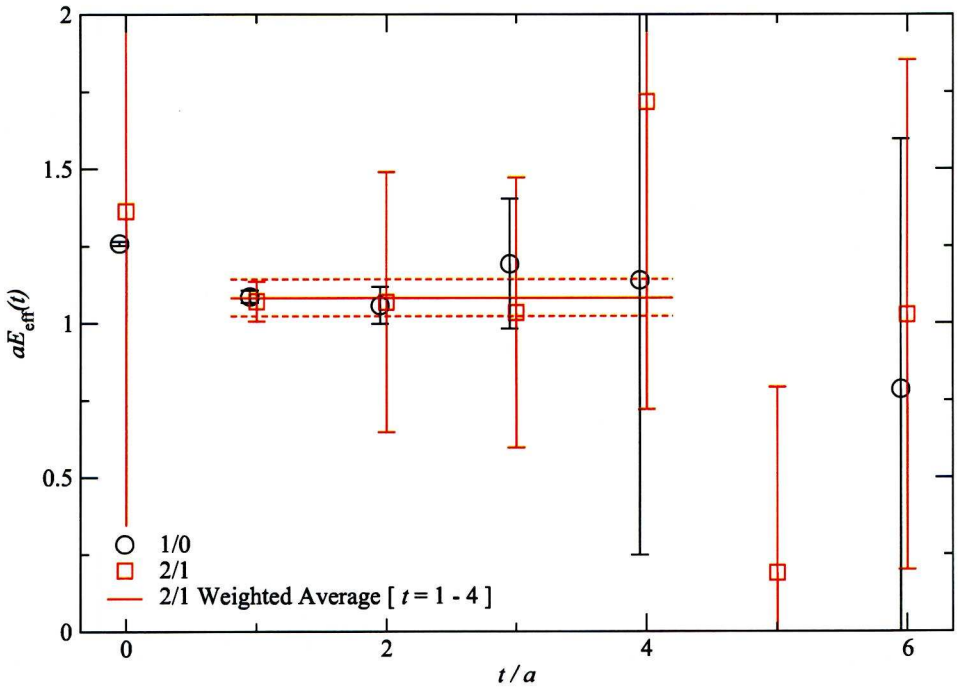

Figure 5.8: The effective masses computed using the variational correlators obtained using a projection on a 4×4 basis of operators $\{\mathcal{O}_0^{A_1^{++}}, \mathcal{O}_1^{A_1^{++}}, \mathcal{O}_2^{A_1^{++}}, \mathcal{O}_3^{A_1^{++}}\}$ with $|\vec{p}| = 1$ at the specified t/t_0. The weighted average between $t = 1$ and $t = 4$ is shown for the $2/1$ basis.

with the groundstate masses for the other two bases, the groundstate lying lower. This gives us reason to believe that this reduction in mass for the largest t/t_0 projection observed previously may indeed be the result of some underlying physics such as glueball decay.

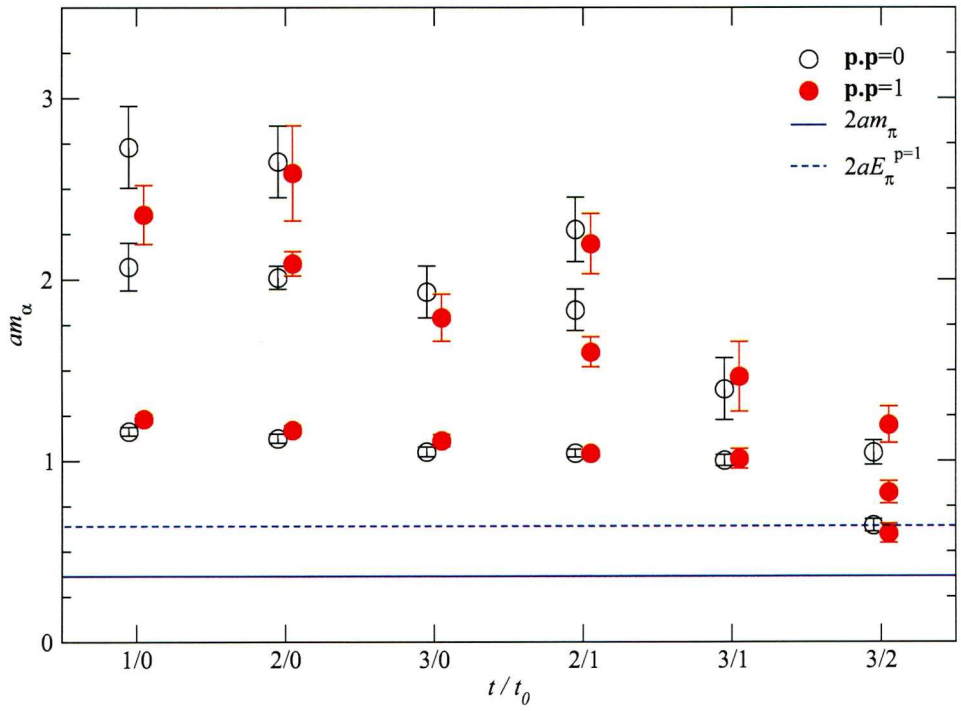

Figure 5.9: The masses extracted from the variational eigenvalues for different t/t_0 using the $|\vec{p}| = 0$ basis of operators $\{\mathcal{O}_0^{A_1^{++}}, \mathcal{O}_2^{A_1^{++}}, \mathcal{O}_3^{A_1^{++}}\}$ and the $|\vec{p}| = 1$ basis of operators $\{\mathcal{O}_1^{A_1^{++}}, \mathcal{O}_2^{A_1^{++}}, \mathcal{O}_3^{A_1^{++}}\}$ on the coarse lattices. The errors are obtained using a bootstrap procedure with $N_{\mathrm{BS}} = 50$. Missing points correspond to negative or very poorly determined eigenvalues. The energies corresponding to a $\pi\pi$ state with $|\vec{p}| = 0$ and $|\vec{p}| = 1$ are drawn for comparision.

We present the effective masses computed using the correlators obtained from the variational projection at various t/t_0 using a basis of operators $\{\mathcal{O}_1^{A_1^{++}}, \mathcal{O}_2^{A_1^{++}}, \mathcal{O}_3^{A_1^{++}}\}$ in Fig. 5.10. The effective energy obtained from taking the weighted average of the effective mass for the 2/1 projection from $t = 1 - 4$ is $aE_{\mathrm{eff}} = 1.080(23)$, which is statistically compatible with the effective energy obtained from the same weighted averaging range using the 2/1 projection from the 4×4 $|\vec{p}| = 1$ basis of $aE_{\mathrm{eff}} = 1.084(60)$.

5.5.3 Alternative Operators

As mentioned in §5.2.4 one may use the handed shape H_8 shown in Fig. 5.1 to form the scalar glueball operator $\mathcal{O}'^{A_1^{++}}$ given in (5.6). We briefly present the results obtained using this operator and compare them to those obtained using the $\mathcal{O}^{A_1^{++}}$ operators.

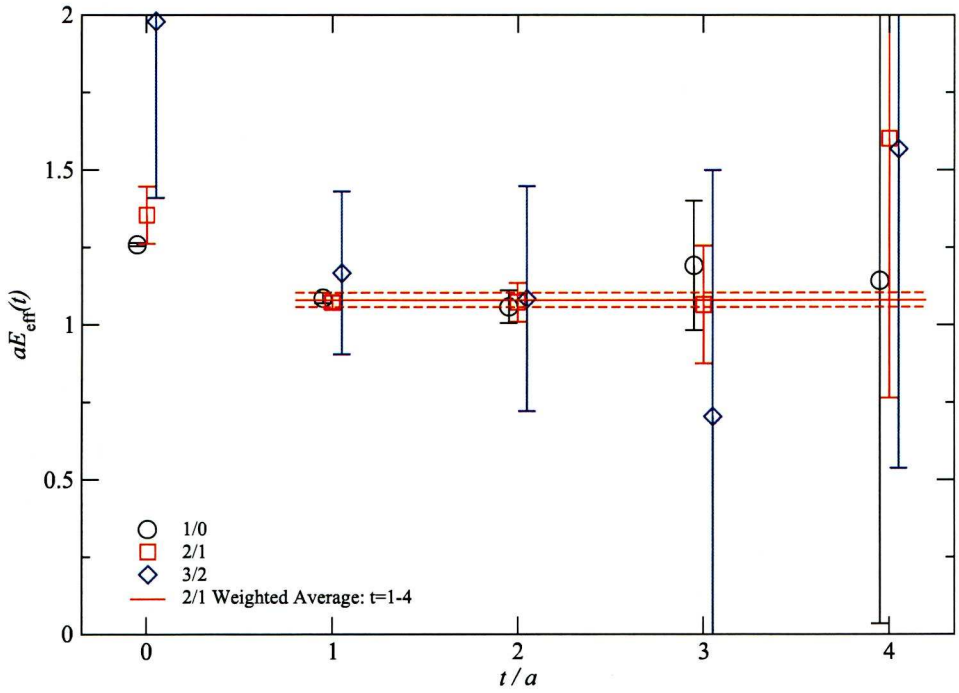

Figure 5.10: Effective masses computed using the variational correlator as defined in (4.18) for different choices of t/t_0, projecting from a matrix of correlators constructed using $\{\mathcal{O}_1^{A_1^{++}}, \mathcal{O}_2^{A_1^{++}}, \mathcal{O}_3^{A_1^{++}}\}$ measured on the coarse lattices with $|\vec{p}| = 1$. The effective masses for the $1/0$ and $2/1$ projections use $\bar{C}_{00}(t)$ whereas the $3/2$ projection uses $\bar{C}_{11}(t)$. The weighted average is shown for the $2/1$ projection, where the errors are computed using a bootstrap procedure with $N_{\rm BS} = 50$.

In Fig. 5.11 we show the variational effective masses for the basis of $|\vec{p}| = 0$ operators $\{\mathcal{O}_0'^{A_1^{++}}, \mathcal{O}_1'^{A_1^{++}}, \mathcal{O}_2'^{A_1^{++}}\}$ projected at various t/t_0 and the weighted average for the 2/1 projection between $t = 2$ and $t = 4$, obtaining $am = 1.002(75)$. This appears to be consistent with the masses obtained using the standard plaquette-like operators as well as those obtained from the eigenspectra of variational projections for both the $\mathcal{O}^{A_1^{++}}$ and $\mathcal{O}'^{A_1^{++}}$ operators, comparisons of which are shown in Fig. 5.12.

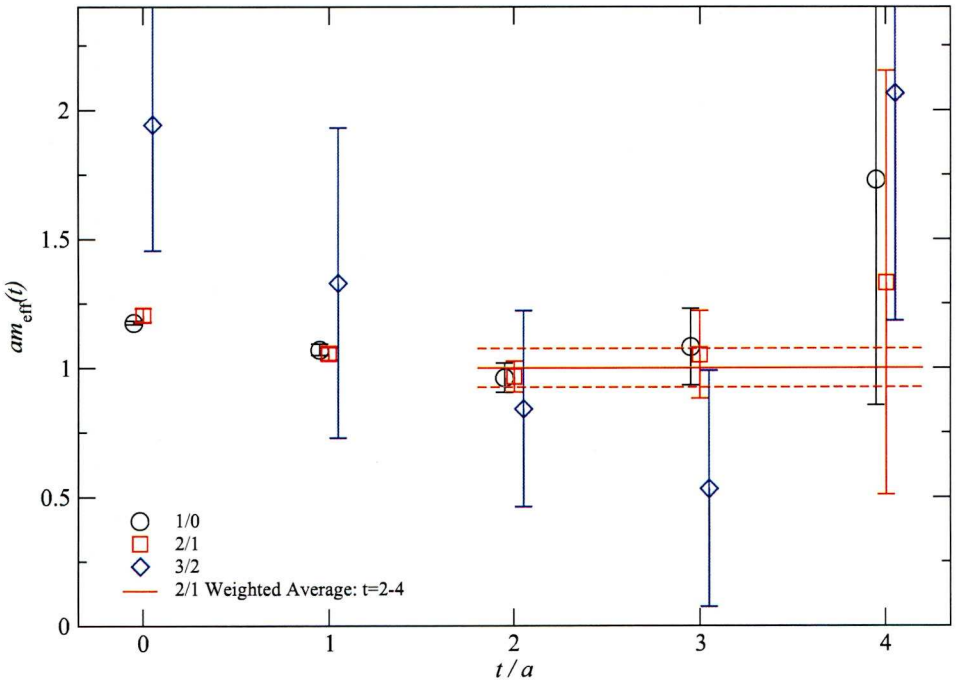

Figure 5.11: The effective masses computed using the variational correlators obtained using a projection on a 3×3 basis of operators $\{\mathcal{O}_0'^{A_1^{++}}, \mathcal{O}_1'^{A_1^{++}}, \mathcal{O}_2'^{A_1^{++}}\}$ with $|\vec{p}| = 0$ at the specified t/t_0. The weighted average between $t = 2$ and $t = 4$ is shown for the 2/1 basis.

5.5.4 Comparison of Mass Estimates

In Fig. 5.13 we present a comparison of various masses obtained so far. These are, from left to right:

- Weighted average $(t = 2 - 5)$ of the variational effective mass from the 2/1 projection on a 3×3 basis of $\{\mathcal{O}_0^{A_1^{++}}, \mathcal{O}_2^{A_1^{++}}, \mathcal{O}_3^{A_1^{++}}\}$ with $|\vec{p}| = 0$.
- Weighted average $(t = 1 - 4)$ of the variational effective mass from the 2/1 projection on a 4×4 basis of $\{\mathcal{O}_0^{A_1^{++}}, \mathcal{O}_1^{A_1^{++}}, \mathcal{O}_2^{A_1^{++}}, \mathcal{O}_3^{A_1^{++}}\}$ with $|\vec{p}| = 1$.
- Weighted average $(t = 1 - 4)$ of the variational effective mass from the 2/1 projection on a 3×3 basis of $\{\mathcal{O}_1^{A_1^{++}}, \mathcal{O}_2^{A_1^{++}}, \mathcal{O}_3^{A_1^{++}}\}$ with $|\vec{p}| = 1$.

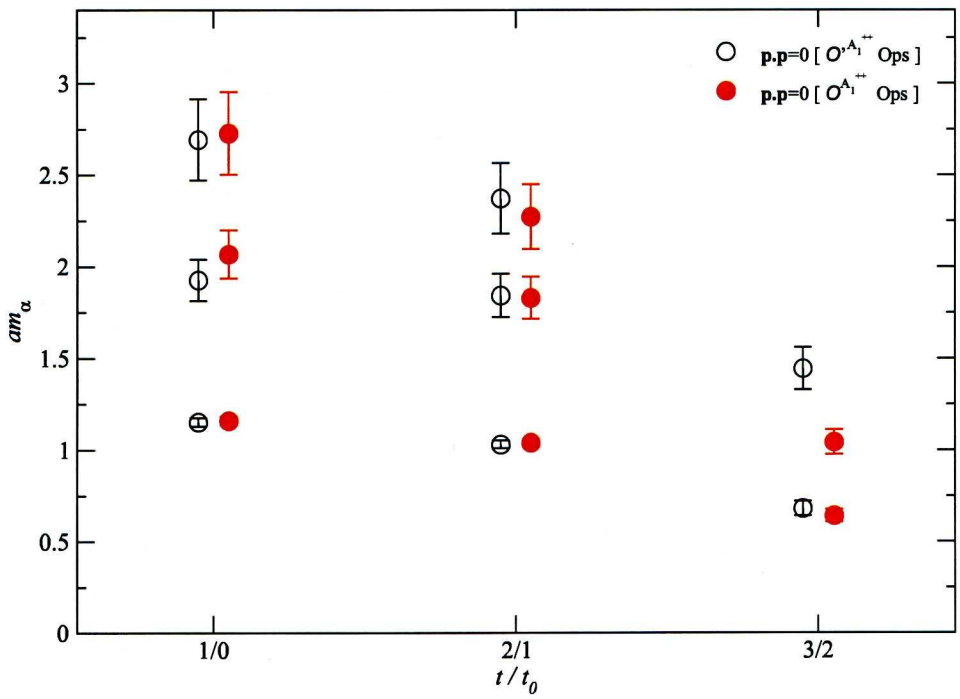

Figure 5.12: The masses extracted from the variational eigenvalues using (4.19) for different t/t_0. These are compared between those obtained from a projection on a basis of $\{\mathcal{O}_0'^{A_1^{++}}, \mathcal{O}_1'^{A_1^{++}}, \mathcal{O}_2'^{A_1^{++}}\}$ (empty circle) and those from a projection on the basis $\{\mathcal{O}_0^{A_1^{++}}, \mathcal{O}_2^{A_1^{++}}, \mathcal{O}_2^{A_1^{++}}\}$.

- Weighted average ($t = 2 - 4$) of the variational effective mass from the 2/1 projection on a 3×3 basis of $\{\mathcal{O}_0^{\prime A_1^{++}}, \mathcal{O}_1^{\prime A_1^{++}}, \mathcal{O}_2^{\prime A_1^{++}}\}$ with $|\vec{p}| = 0$.
- Mass extracted from the groundstate eigenvalue of the 2/1 projection of a 3×3 basis of $\{\mathcal{O}_0^{A_1^{++}}, \mathcal{O}_2^{A_1^{++}}, \mathcal{O}_3^{A_1^{++}}\}$ with $|\vec{p}| = 0$.
- Mass extracted from the groundstate eigenvalue of the 2/1 projection of a 3×3 basis of $\{\mathcal{O}_1^{A_1^{++}}, \mathcal{O}_2^{A_1^{++}}, \mathcal{O}_3^{A_1^{++}}\}$ with $|\vec{p}| = 1$.
- Mass extracted from the first excited state eigenvalue of the 3/2 projection of a 3×3 basis of $\{\mathcal{O}_0^{A_1^{++}}, \mathcal{O}_2^{A_1^{++}}, \mathcal{O}_3^{A_1^{++}}\}$ with $|\vec{p}| = 0$.
- Mass extracted from the first excited state eigenvalue of the 3/2 projection of a 3×3 basis of $\{\mathcal{O}_1^{A_1^{++}}, \mathcal{O}_2^{A_1^{++}}, \mathcal{O}_3^{A_1^{++}}\}$ with $|\vec{p}| = 1$.
- Mass extracted from the groundstate eigenvalue of the 2/1 projection of a 3×3 basis of $\{\mathcal{O}_0^{\prime A_1^{++}}, \mathcal{O}_1^{\prime A_1^{++}}, \mathcal{O}_2^{\prime A_1^{++}}\}$ with $|\vec{p}| = 0$.

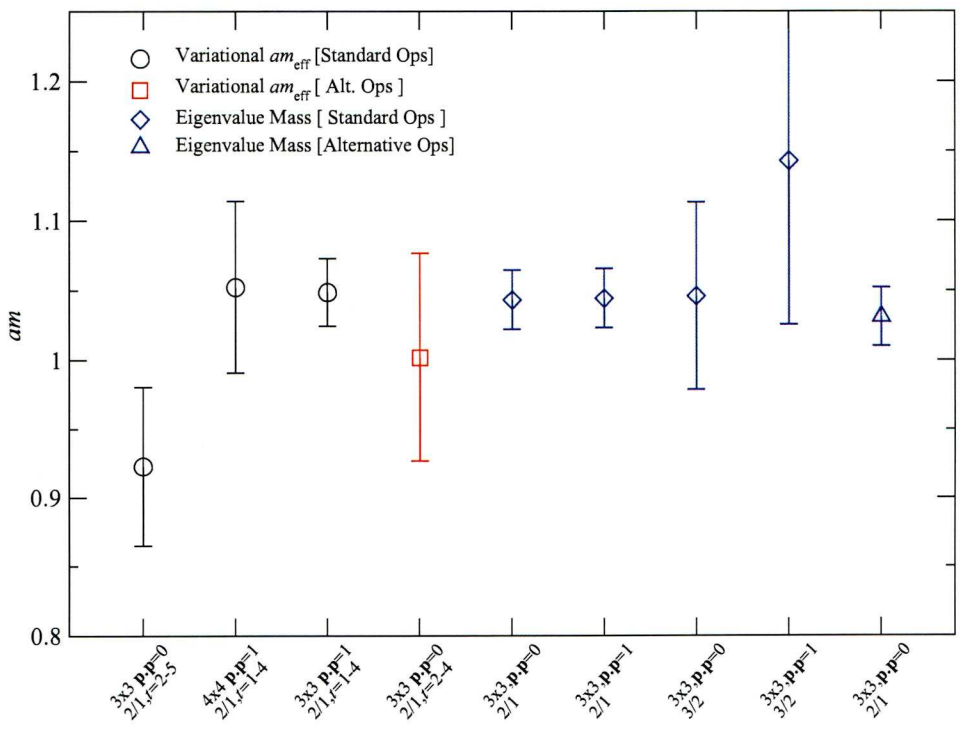

Figure 5.13: Comparison of mass estimates obtained for the scalar glueball using different methods (effective masses and variational eigenvalues). The points are described briefly on the axis and a more detailed description is given in the text (§5.5.4).

We note that there is good consistency between the different mass determinations from different sources. The estimate for the weighted average ($t = 2 - 5$) of the effective mass obtained using the variational groundstate correlator formed using the

2/1 projection on the $\{\mathcal{O}_0^{A_1^{++}}, \mathcal{O}_2^{A_1^{++}}, \mathcal{O}_3^{A_1^{++}}\}$ basis of operators does lie somewhat lower, although is statistically consistent with the other determinations at the 1σ level.

5.6 Factorising Fit Results

Since we have observed what we believe to be evidence of an open decay channel in the variational eigenvalue results we look to perform factorising fits as described in Section 4.6. In principle this should help us to resolve the "glueball" and decay channel states simultaneously, although one must remember that in the presence of decay channels our notion of a transfer matrix eigenstate no longer holds.

We begin by performing fully correlated factorising fits to a 4×4 matrix of correlators, using the basis of scalar glueball operators $\{\mathcal{O}_0^{A_1^{++}}, \mathcal{O}_1^{A_1^{++}}, \mathcal{O}_2^{A_1^{++}}, \mathcal{O}_3^{A_1^{++}}\}$ for both $|\vec{p}| = 0$ and $|\vec{p}| = 1$. We vary both the fit ranges and the value of N_{exp} in (4.25), *i.e.* the number of exponentials to which we fit. Our criteria for a good fit are that the χ^2/d.o.f. should be near to 1 and that the resulting parameters should be reasonably stable with respect to changes in the fit range.

In Fig. 5.14 and Table 5.6 we present the factorising fit results for this basis for both $N_{\text{exp}} = 2$ and $N_{\text{exp}} = 3$, with t_{max} fixed at $t = 6$ and a varying t_{min}. For $t_{\text{min}} \geq 2$ one can see good consistency between the two and three-exponential fits, however on closer inspection of the final fit parameters one can see that this is due to the mass m_2 favouring a very large value such that its contribution is essentially zero for all t — this not only gives us confidence that our vacuum subtraction has been performed sufficiently well[5] but also tells us that two-exponential fits ought to be sufficient.

One can see that groundstates obtained from the $|\vec{p}| = 0$ correlators show a downward trend as one increases t_{min}. This is consistent with the picture obtained from both the effective mass weighted averages (Fig. 5.7) and the masses extracted from the variational eigenvalues[6] (Fig. 5.9). That the trend is weaker for the $|\vec{p}| = 1$ correlators than for the $|\vec{p}| = 0$ correlators is inconsistent — the $|\vec{p}| = 1$ fits show no low lying state — although one must take into account the particularly poor χ^2/d.o.f. values for the $|\vec{p}| = 1$ fits.

In Fig. 5.15 and Table 5.7 we again present the factorising fit results for this basis for both $N_{\text{exp}} = 2$ and $N_{\text{exp}} = 3$, but with t_{max} fixed at $t_{\text{max}} = 7$ and a varying t_{min}. Again there is good consistency between the two and three-exponential fits, however this is again due to m_2 either becoming large or, in several cases, degenerate with m_1.

[5] If the vacuum subtraction had not removed the vacuum contribution completely there would be an additive constant which would result in any redundant mass parameters defaulting to zero in order to take this into account.

[6] The variational projection for Fig. 5.9 was carried out on the basis $\{\mathcal{O}_0^{A_1^{++}}, \mathcal{O}_1^{A_1^{++}}, \mathcal{O}_2^{A_1^{++}}\}$.

N_{exp}	$\lvert\vec{p}\rvert$	t_{min}	t_{max}	am_0	am_1	am_2	χ^2/d.o.f.
2	0	1	6	1.0336(29)	1.84(11)	—	3.176
		2	6	0.887(14)	1.332(47)	—	0.635
		3	6	0.62(13)	1.22(10)	—	0.349
2	1	1	6	1.0770(60)	1.70(14)	—	0.832
		2	6	1.034(36)	1.42(22)	—	0.301
		3	6	1.19(15)	3.30[−]	—	0.189
3	0	1	6	0.9409(43)	1.626(37)	18.04[−]	1.309
		2	6	0.32(15)	0.9495(57)	1.77[−]	0.607
		3	6	0.306(92)	1.016(17)	7.79[−]	0.327
3	1	1	6	1.0682(60)	1.623(75)	21.26[−]	0.329
		2	6	1.046(31)	1.41(20)	3.53[−]	0.173

Table 5.6: Fitted mass parameters for two and three-exponential factorising fits to a 4×4 matrix of correlators using a basis of operators $\{\mathcal{O}_0^{A_1^{++}}, \mathcal{O}_1^{A_1^{++}}, \mathcal{O}_2^{A_1^{++}}, \mathcal{O}_3^{A_1^{++}}\}$ with $|\vec{p}| = 0$ and $|\vec{p}| = 1$ for varying t_{min} with t_{max} fixed at $t = 6$. Where errors are quoted as [−] this indicates that the gradient in that direction of parameter space could not be determined, *i.e.* that the parameter is essentially free.

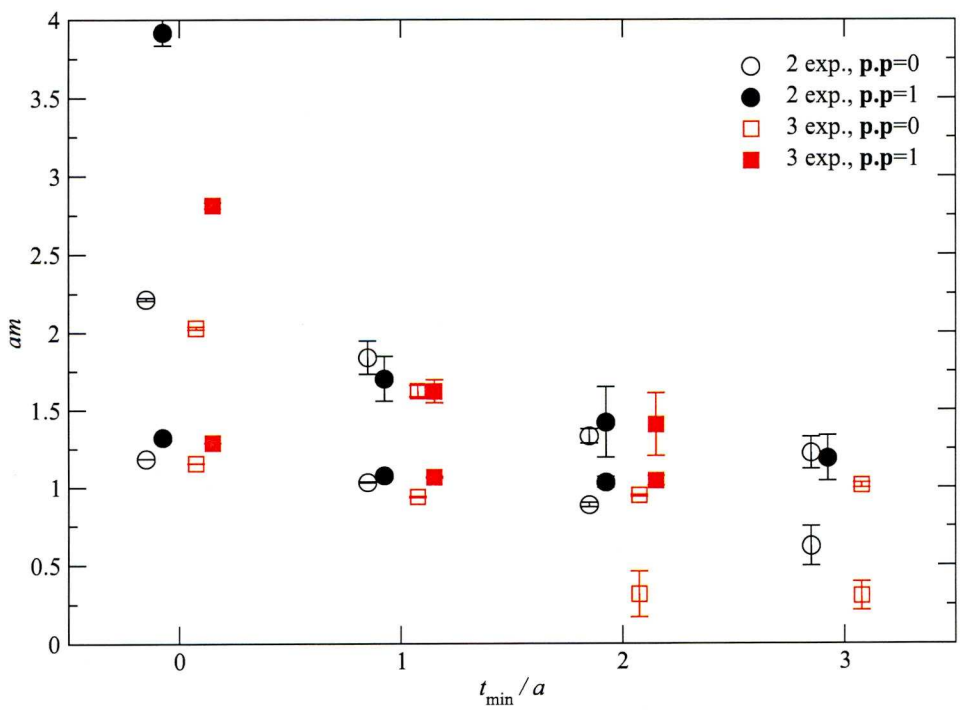

Figure 5.14: Results from factorising fits applied to the 4×4 basis of scalar glueball operators $\{\mathcal{O}_0^{A_1^{++}}, \mathcal{O}_1^{A_1^{++}}, \mathcal{O}_2^{A_1^{++}}, \mathcal{O}_3^{A_1^{++}}\}$. Both two and three-exponential fits are presented for the $|\vec{p}| = 0$ and $|\vec{p}| = 1$ correlators, with $t_{\text{max}} = 6$ and t_{min} allowed to vary. The two-exponential results are presented as circles, three-exponential results as squares, $|\vec{p}| = 0$ results open shapes and $|\vec{p}| = 1$ results filled shapes.

The same downward trend for the $|\vec{p}| = 0$ groundstate is observed, although in this case it appears to onset more gently (compare, for example, the three-exponential $|\vec{p}| = 0$ results for both). Although a low lying groundstate can be observed in the $|\vec{p}| = 1$ three-exponential fit for $t_{\text{min}} = 4$ we choose to ignore it due to the small χ^2/d.o.f. and the poor determination of the remaining masses.

N_{exp}	$\lvert\vec{p}\rvert$	t_{min}	t_{max}	am_0	am_1	am_2	χ^2/d.o.f.
2	0	1	7	1.0335(29)	1.84(11)	—	2.718
		2	7	0.886(14)	1.327(46)	—	0.532
		3	7	0.66(13)	1.24(13)	—	0.285
		4	7	0.423(56)	1.24(10)	—	0.176
2	1	1	7	1.0758(61)	1.70(14)	—	1.39
		2	7	0.97(12)	1.35(24)	—	1.0274
3	0	1	7	0.9405(43)	1.624(37)	11.40[−]	1.118
		2	7	0.887(14)	1.265(67)	1.359(23)	0.509
		3	7	0.467(67)	1.042(37)	8.295(42)	0.268
		4	7	0.423(56)	1.24(10)	8.46[−]	0.182
3	1	1	7	1.0665(61)	1.629(75)	14.55[−]	0.962
		2	7	1.055(28)	1.34(13)	1.42(18)	0.182
		3	7	1.09(15)	1.213(65)	9.17[−]	0.165
		4	7	0.70(13)	2.59[−]	12.25[−]	0.122

Table 5.7: Fitted mass parameters for two and three-exponential factorising fits to a 4×4 matrix of correlators using a basis of operators $\{\mathcal{O}_0^{A_1^{++}}, \mathcal{O}_1^{A_1^{++}}, \mathcal{O}_2^{A_1^{++}}, \mathcal{O}_3^{A_1^{++}}\}$ with $|\vec{p}| = 0$ and $|\vec{p}| = 1$ for varying t_{min} with t_{max} fixed at $t = 7$. Where errors are quoted as [−] this indicates that the gradient in that direction of parameter space could not be determined, *i.e.* that the parameter is essentially free.

One can see from both Tables 5.6 and 5.7 that whilst some fits prefer a groundstate with $am \sim 1.05$ others prefer a groundstate with $am \sim 0.9$ (we of course neglect those fits which appear to contain decay products) — this anomaly appears to be independent of N_{exp}, $|\vec{p}|$ and to some degree fit range. From Figs. 5.14 and 5.15 one can see that the decrease in the groundstate mass is monotonic with respect to t_{min} within each particular subset (*i.e.* $N_{\text{exp}} = 2, |\vec{p}| = 0$; $N_{\text{exp}} = 2, |\vec{p}| = 1$; $N_{\text{exp}} = 3, |\vec{p}| = 0$; and $N_{\text{exp}} = 3, |\vec{p}| = 1$), except for that corresponding to $[t_{\text{min}}, t_{\text{max}}] = [3, 6]$ for $N_{\text{exp}} = 2, |\vec{p}| = 1$ which due to the undetermined uncertainty on am_1 we discount as a poor fit. We therefore feel that the mass $am \sim 0.9$ is likely to be an artefact of the fitting procedure, however in order to clarify this we will check the dependence on t_{max} for a fixed t_{min}. Further to this we will use the $\mathcal{O}'^{A_1^{++}}$ operators in order to obtain a more independent cross-check.

5.6.1 t_{max} Dependence

In Figs. 5.16, 5.19 and 5.20 we present the t_{max} dependence of the factorising fits on a 4×4 matrix of correlators using the basis $\{\mathcal{O}_0^{A_1^{++}}, \mathcal{O}_1^{A_1^{++}}, \mathcal{O}_2^{A_1^{++}}, \mathcal{O}_3^{A_1^{++}}\}$ with both

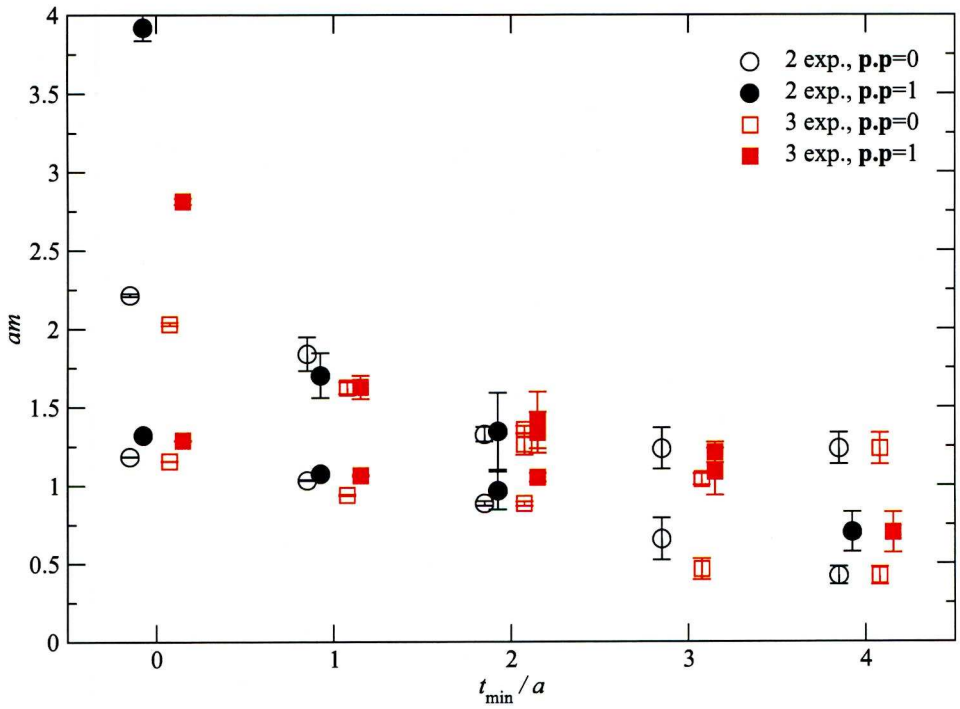

Figure 5.15: Results from factorising fits applied to the 4×4 basis of scalar glueball operators $\{\mathcal{O}_0^{A_1^{++}}, \mathcal{O}_1^{A_1^{++}}, \mathcal{O}_2^{A_1^{++}}, \mathcal{O}_3^{A_1^{++}}\}$. Both two and three-exponential fits are presented for the $|\vec{p}| = 0$ and $|\vec{p}| = 1$ correlators, with $t_{\text{max}} = 7$ and t_{min} allowed to vary. The two-exponential results are presented as circles, three-exponential results as squares, $|\vec{p}| = 0$ results open shapes and $|\vec{p}| = 1$ results filled shapes.

$|\vec{p}| = 0$ and $|\vec{p}| = 1$ for $t_{\text{min}} = 1$, 2 and 3 respectively. One can see instantly from Fig. 5.16 that the t_{max} dependence is virtually non-existent for $t_{\text{min}} = 1$, with all but the $N_{\text{exp}} = 3$, $|\vec{p}| = 0$ correlators favouring the $am \sim 1.05$ state.

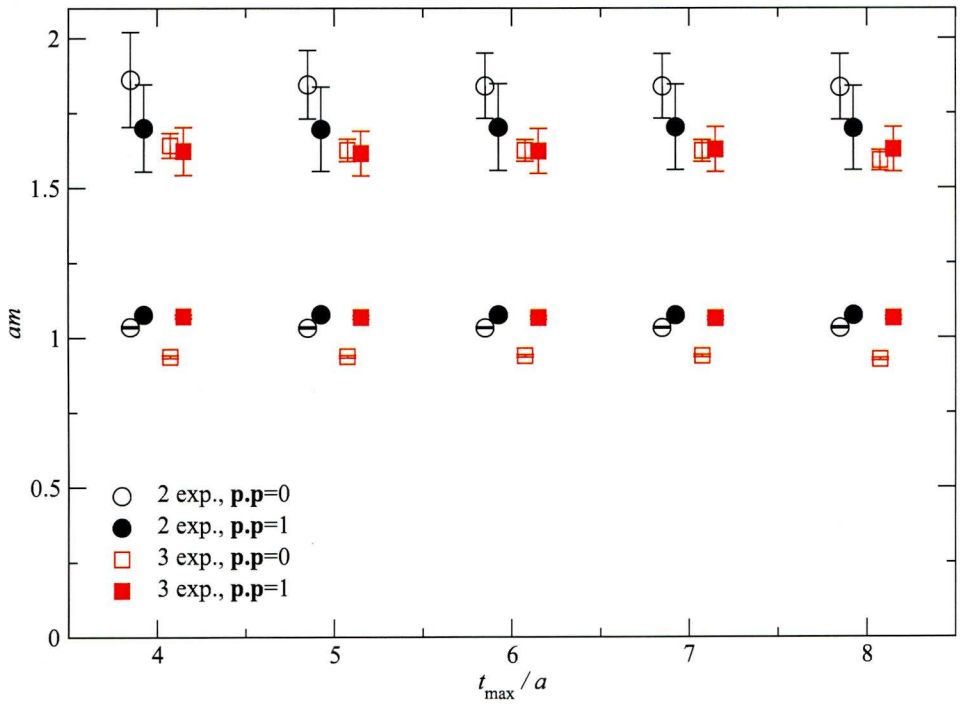

Figure 5.16: Results from factorising fits applied to the 4×4 basis of scalar glueball operators $\{\mathcal{O}_0^{A_1^{++}}, \mathcal{O}_1^{A_1^{++}}, \mathcal{O}_2^{A_1^{++}}, \mathcal{O}_3^{A_1^{++}}\}$. Both two and three-exponential fits are presented for the $|\vec{p}| = 0$ and $|\vec{p}| = 1$ correlators, with $t_{\text{min}} = 1$ and t_{max} allowed to vary. The two-exponential results are presented as circles, three-exponential results as squares, $|\vec{p}| = 0$ results open shapes and $|\vec{p}| = 1$ results filled shapes.

The goodness-of-fit values for the $t_{\text{min}} = 1$ fits are presented in Table 5.8 and it is not immediately obvious why there is an inconsistency between the different fits — most χ^2/d.o.f. values are good, with the exception of those corresponding to $N_{\text{exp}} = 2$, $|\vec{p}| = 0$, and the second mass is reasonably well determined. However since the third mass obtained using three-exponential fits is unphysically large (~ 16 GeV) we should be wary of using these fits. Furthermore from the correlators themselves (Fig. 5.17) we see that for $t > 6$ the signal appears to be unreliable and as such fits for $t_{\text{max}} > 6$ are likely to be misleading. Indeed if we discount these three-exponential fits there is no longer an inconsistency for the $t_{\text{min}} = 1$ results.

Turning to the $t_{\text{min}} = 2$ results in Table 5.9 and Fig. 5.19, concentrating on $N_{\text{exp}} = 2$ and $t_{\text{max}} < 7$, we see a statistically significant inconsistency between the $|\vec{p}| = 0$ and $|\vec{p}| = 1$ results. Here one must concede that the χ^2/d.o.f. for the $|\vec{p}| = 0$ fits are better than those for the $|\vec{p}| = 1$ fits as is the resolution of the second mass. The fitted

N_{exp}	$\lvert\vec{p}\rvert$	t_{min}	t_{max}	am_0	am_1	am_2	χ^2/d.o.f.
2	0	1	4	1.0364(33)	1.86(16)	—	4.512
		1	5	1.0339(29)	1.84(11)	—	3.772
		1	6	1.0336(29)	1.84(11)	—	3.177
		1	7	1.0335(29)	1.84(11)	—	2.718
		1	8	1.0328(29)	1.84(11)	—	3.318
2	1	1	4	1.0777(61)	1.70(15)	—	1.017
		1	5	1.0785(60)	1.70(14)	—	0.853
		1	6	1.0770(60)	1.70(15)	—	0.832
		1	7	1.0758(61)	1.70(15)	—	1.385
		1	8	1.0753(61)	1.70(14)	—	1.534
3	0	1	4	0.9379(47)	1.643(41)	10.82[−]	1.709
		1	5	0.9386(44)	1.627(37)	11.35[−]	1.509
		1	6	0.9409(43)	1.625(37)	18.03[−]	1.309
		1	7	0.9405(43)	1.625(37)	11.40[−]	1.118
		1	8	0.9283(47)	1.592(33)	11.38[−]	1.897
3	1	1	4	1.0721(60)	1.624(80)	2.35[−]	0.247
		1	5	1.0698(60)	1.616(74)	12.72[−]	0.251
		1	6	1.0682(59)	1.624(75)	21.25[−]	0.329
		1	7	1.0665(60)	1.629(75)	14.55[−]	0.962
		1	8	1.0657(61)	1.629(74)	13.62[−]	1.170

Table 5.8: Fitted mass parameters for two and three-exponential factorising fits to a 4×4 matrix of correlators using a basis of operators $\{\mathcal{O}_0^{A_1^{++}}, \mathcal{O}_1^{A_1^{++}}, \mathcal{O}_2^{A_1^{++}}, \mathcal{O}_3^{A_1^{++}}\}$ with $|\vec{p}| = 0$ and $|\vec{p}| = 1$ for varying t_{max} with t_{min} fixed at $t = 1$. Where errors are quoted as [−] this indicates that the gradient in that direction of parameter space could not be determined, *i.e.* that the parameter is essentially free.

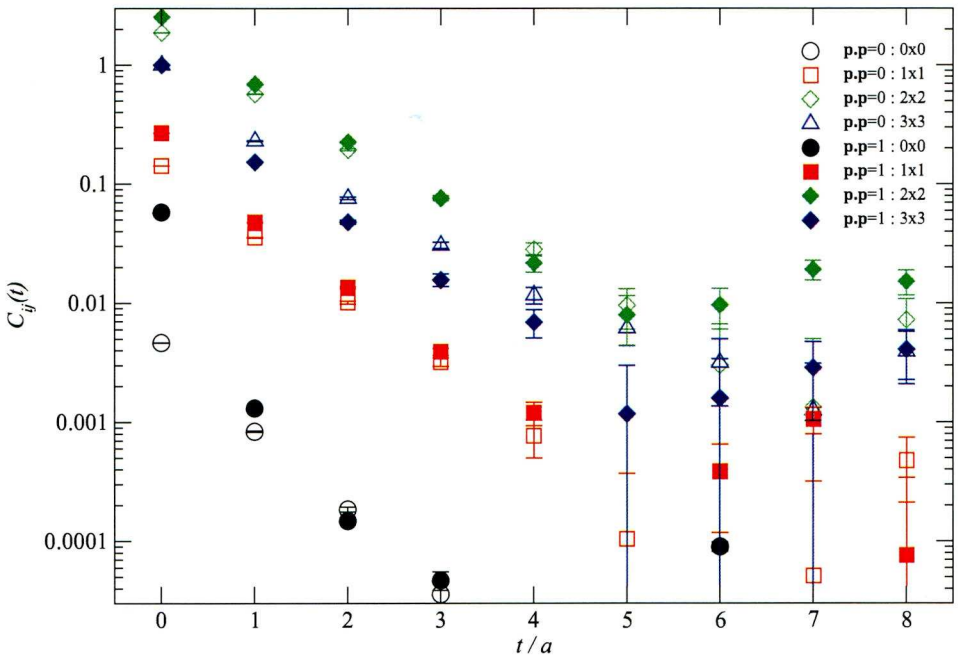

Figure 5.17: The diagonal entries of the 4×4 matrix of correlators formed using the basis of scalar glueball operators $\{\mathcal{O}_0^{A_1^{++}}, \mathcal{O}_1^{A_1^{++}}, \mathcal{O}_2^{A_1^{++}}, \mathcal{O}_3^{A_1^{++}}\}$. The $|\vec{p}| = 0$ results are presented as open shapes and the $|\vec{p}| = 1$ results presented as filled shapes.

correlators are plotted in Fig. 5.18, where the masses have be reconverted to energies for the $|\vec{p}| = 1$ correlators. Whilst one cannot make a direct comparison between the $|\vec{p}| = 0$ and $|\vec{p}| = 1$ results for exactly this reason we do notice that there is no observable difference between the quality of fit for the $|\vec{p}| = 0$ and $|\vec{p}| = 1$ correlators, certainly not one large enough to justify such a large difference in the mass estimates.

5.6.2 Alternative Operators

Since this inconsistency has arisen, and has not been resolved, using the $\mathcal{O}^{A_1^{++}}$ operators we shall perform factorising fits using the alternative scalar glueball operators $\mathcal{O}'^{A_1^{++}}$ which for the variational effective mass showed a value consistent with the $am \sim 1.05$ determinations. We have measured fewer handed operators, representing a reduction in statistics of one-half, and the largest basis we can construct is a 3×3 basis since one cannot construct the loops H_8 on a our lattices if more than two levels of Teper blocking have been applied, on top of APE smearing. The operators have been constructed for $|\vec{p}| = 0$ only.

We first performed fully correlated fits to the data with $N_{\rm exp} = 2$ however these gave unacceptably large values for χ^2/d.o.f. for all combinations of $t_{\rm min}$ and $t_{\rm max}$, possibly due to the reduction in statistics. We therefore performed uncorrelated fits for $t_{\rm max} = 6$

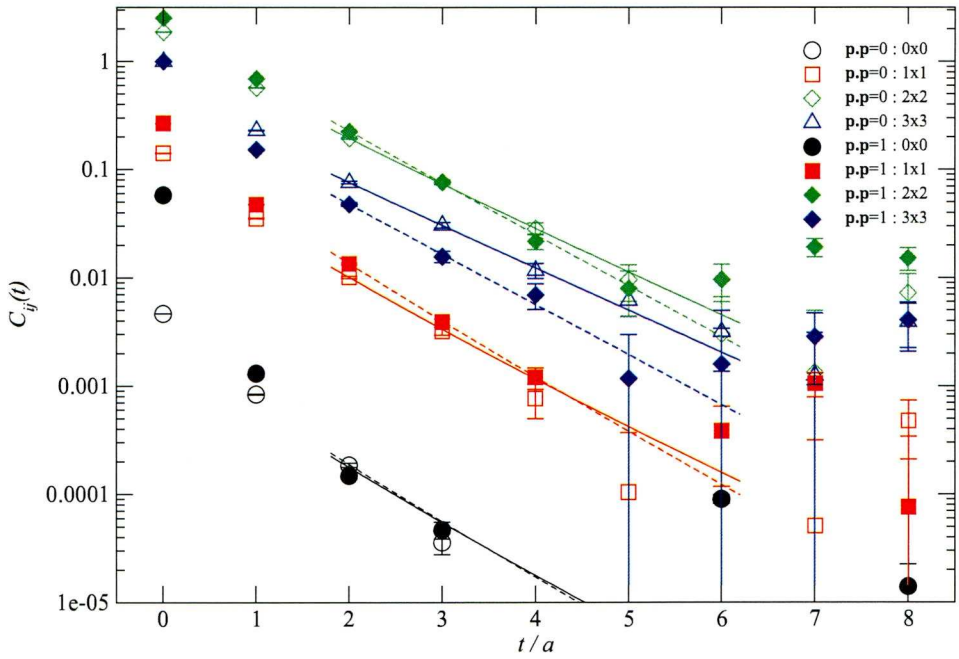

Figure 5.18: The diagonal entries of the 4×4 matrix of correlators formed using the basis of scalar glueball operators $\{\mathcal{O}_0^{A_1^{++}}, \mathcal{O}_1^{A_1^{++}}, \mathcal{O}_2^{A_1^{++}}, \mathcal{O}_3^{A_1^{++}}\}$. The $|\vec{p}| = 0$ results are presented as open shapes and the $|\vec{p}| = 1$ results presented as filled shapes. The factorising fits from $t_{\text{min}} = 2$ to $t_{\text{max}} = 6$ to the same basis are presented with the $|\vec{p}| = 0$ fits as solid lines and the $|\vec{p}| = 1$ as dashed lines.

N_{exp}	$\lvert\vec{p}\rvert$	t_{min}	t_{max}	am_0	am_1	am_2	χ^2/d.o.f.
2	0	2	5	0.888(14)	1.371(53)	—	0.688
		2	6	0.887(14)	1.332(47)	—	0.635
		2	7	0.887(14)	1.327(46)	—	0.532
		2	8	0.804(23)	1.1823(23)	—	1.456
2	1	2	5	1.053(27)	1.45(26)	—	0.195
		2	6	1.034(36)	1.42(23)	—	0.301
		2	7	0.96(12)	1.35(25)	—	1.027
		2	8	0.329(70)	1.139(25)	—	0.715
3	0	2	5	0.89[−]	1.31(18)	1.39[−]	0.657
		2	6	0.8875(15)	1.269(68)	1.368(22)	0.609
		2	7	0.886(14)	1.327(46)	38.03[−]	0.544
		2	8	0.805(23)	1.183(23)	34.43[−]	1.483
3	1	2	5	0.52(82)	1.079(17)	1.99(47)	0.174
		2	6	1.051(28)	1.44(24)	4.04[−]	0.173
		2	7	0.97(12)	1.35(25)	38.03[−]	1.050
		2	8	0.330(70)	1.139(25)	34.43[−]	0.729

Table 5.9: Fitted mass parameters for two and three-exponential factorising fits to a 4×4 matrix of correlators using a basis of operators $\{\mathcal{O}_0^{A_1^{++}}, \mathcal{O}_1^{A_1^{++}}, \mathcal{O}_2^{A_1^{++}}, \mathcal{O}_3^{A_1^{++}}\}$ with $|\vec{p}| = 0$ and $|\vec{p}| = 1$ for varying t_{max} with t_{min} fixed at $t = 2$. Where errors are quoted as [−] this indicates that the gradient in that direction of parameter space could not be determined, *i.e.* that the parameter is essentially free.

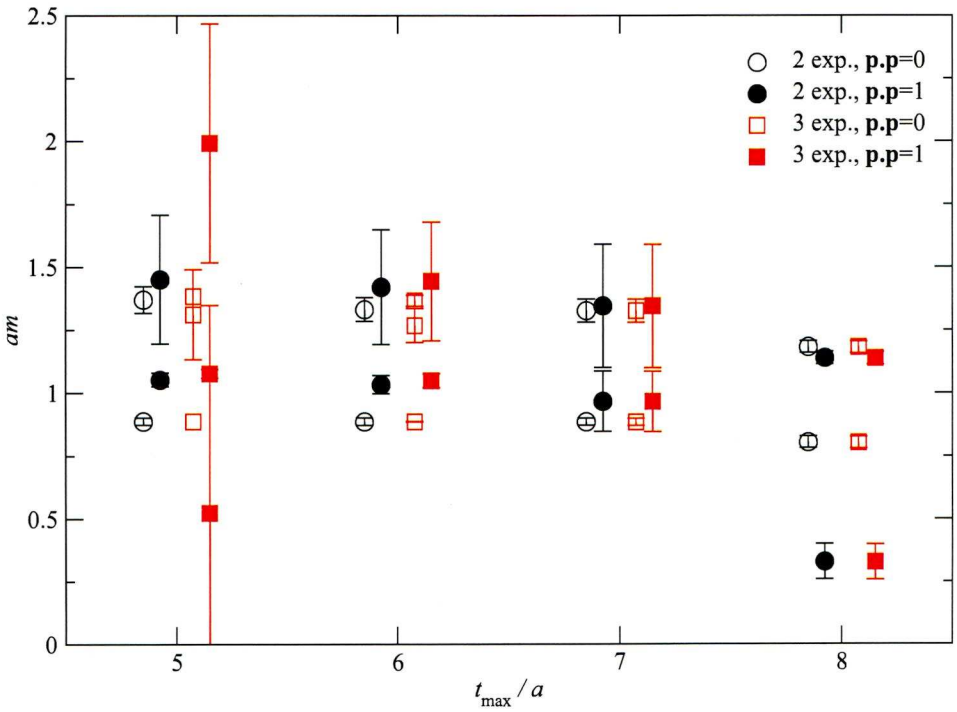

Figure 5.19: Results from factorising fits applied to the 4×4 basis of scalar glueball operators $\{\mathcal{O}_0^{A_1^{++}}, \mathcal{O}_1^{A_1^{++}}, \mathcal{O}_2^{A_1^{++}}, \mathcal{O}_3^{A_1^{++}}\}$. Both two and three-exponential fits are presented for the $|\vec{p}| = 0$ and $|\vec{p}| = 1$ correlators, with $t_{\text{min}} = 2$ and t_{max} allowed to vary. The two-exponential results are presented as circles, three-exponential results as squares, $|\vec{p}| = 0$ results open shapes and $|\vec{p}| = 1$ results filled shapes.

N_{exp}	$\lvert\vec{p}\rvert$	t_{min}	t_{max}	am_0	am_1	am_2	χ^2/d.o.f.
2	0	3	6	0.62(13)	1.22(10)	—	0.350
		3	7	0.66(13)	1.24(13)	—	0.285
2	1	3	6	1.19(15)	3.30[−]	—	0.189
		3	7	1.08[−]	1.24[−]	—	0.185
		3	8	0.12[−]	1.48[−]	—	0.377
3	0	3	6	0.62(13)	1.22(10)	14.24[−]	0.362
		3	7	0.467(67)	1.042(37)	7.970(43)	0.268
3	1	3	6	1.19(15)	2.78[−]	14.24[−]	0.195
		3	7	1.09(15)	1.213(65)	9.17[−]	0.165
		3	8	0.13[−]	0.63[−]	1.504(80)	0.346

Table 5.10: Fitted mass parameters for two and three-exponential factorising fits to a 4×4 matrix of correlators using a basis of operators $\{\mathcal{O}_0^{A_1^{++}}, \mathcal{O}_1^{A_1^{++}}, \mathcal{O}_2^{A_1^{++}}, \mathcal{O}_3^{A_1^{++}}\}$ with $|\vec{p}| = 0$ and $|\vec{p}| = 1$ for varying t_{max} with t_{min} fixed at $t = 3$. Where errors are quoted as [−] this indicates that the gradient in that direction of parameter space could not be determined, *i.e.* that the parameter is essentially free.

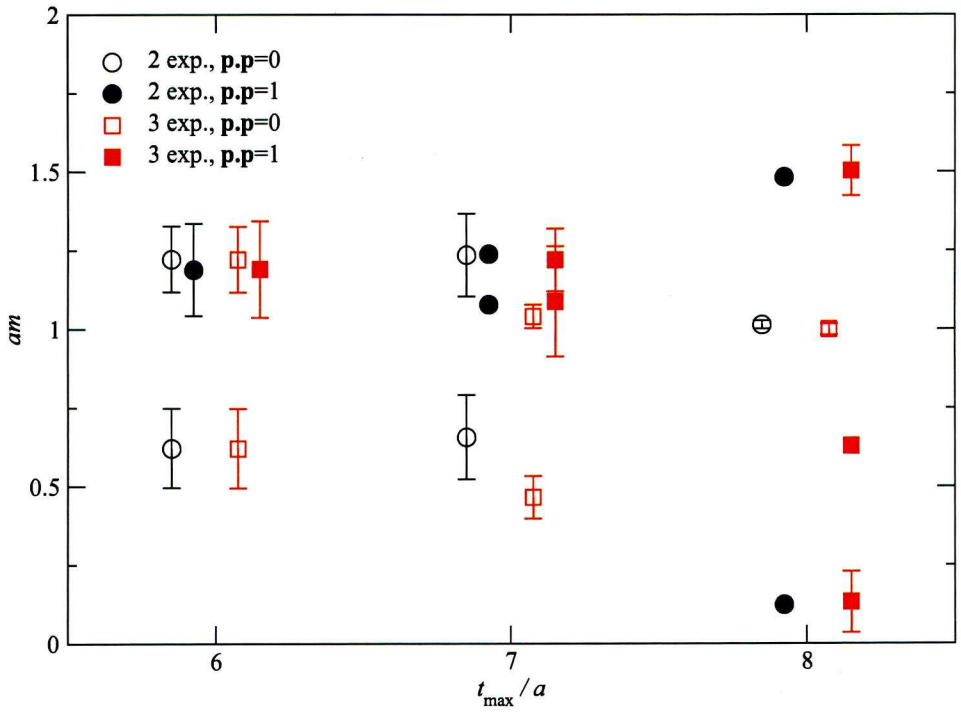

Figure 5.20: Results from factorising fits applied to the 4×4 basis of scalar glueball operators $\{\mathcal{O}_0^{A_1^{++}}, \mathcal{O}_1^{A_1^{++}}, \mathcal{O}_2^{A_1^{++}}, \mathcal{O}_3^{A_1^{++}}\}$. Both two and three-exponential fits are presented for the $|\vec{p}| = 0$ and $|\vec{p}| = 1$ correlators, with $t_{\text{min}} = 3$ and t_{max} allowed to vary. The two-exponential results are presented as circles, three-exponential results as squares, $|\vec{p}| = 0$ results open shapes and $|\vec{p}| = 1$ results filled shapes.

which appeared to give the most acceptable results — these are presented in Table. 5.11 and Fig. 5.21 in which we also present a direct comparison with the $t_{\max} = 6$ fits for the $\mathcal{O}^{A_1^{++}}$ operators.

We note that at $t_{\min} = 1$ there is good consistency between the groundstate mass determinations using the 3×3 basis of handed operators the 4×4 basis of plaquette operators — the former being 1.044(14) with χ^2/d.o.f. $= 0.433$ and the latter being 1.0336(29) with χ^2/d.o.f. $= 3.177$. Not only are the groundstate masses consistent within errors but the first-excited states are also compatible within errors: $am_1 =$ 1.98(18) for the $\mathcal{O}'^{A_1^{++}}$ correlators and $am_1 = 1.84(11)$ for the $\mathcal{O}^{A_1^{++}}$ correlators.

We feel this gives a strong indication that this is indeed the mass corresponding most directly to the scalar glueball state on the coarse lattices, the intermediate $am \sim 0.9$ state possibly due to metastabilities in the fits caused by the presence of a decay channel, and the lower masses ($am \sim 0.6$) representing decay products.

$t_{\min}$	$t_{\max}$	am_0	am_1	χ^2/d.o.f.
0	6	1.1508(39)	1.920(27)	5.123
1	6	1.044(14)	1.98(18)	0.433
2	6	1.044(25)	8(4)	0.474
3	6	1.289(79)	49[–]	0.358

Table 5.11: Fitted mass parameters for two-exponential uncorrelated factorising fits to a 3×3 matrix of correlators formed using the basis of handed scalar glueball operators $\{\mathcal{O}_0'^{A_1^{++}}, \mathcal{O}_1'^{A_1^{++}}, \mathcal{O}_2'^{A_1^{++}}\}$ with $t_{\max} = 6$ for varying $t_{\min}$. Where errors are quoted as [–] this means the gradient in that direction of parameter space could not be determined, *i.e.* that the parameter is essentially free.

5.6.3 Overall Average

Having made several measurements, using various different methods, of the scalar glueball mass which we believe to be accurate estimates we wish to find the average of these results. We choose to use the weighted averaging method used by the Particle Data Group (PDG) [132] for which we must determine the systematic errors on each determination. We choose to use the results from five methods:

- the weighted averages obtained from the variational effective masses computed on the following four projections : the 2/1 projection on a 3×3 basis of $\{\mathcal{O}_0^{A_1^{++}}, \mathcal{O}_2^{A_1^{++}}, \mathcal{O}_3^{A_1^{++}}\}$ with $|\vec{p}| = 0$, computed between $t = 2 - 5$; the 2/1 projection on a 4×4 basis of $\{\mathcal{O}_0^{A_1^{++}}, \mathcal{O}_1^{A_1^{++}}, \mathcal{O}_2^{A_1^{++}}, \mathcal{O}_3^{A_1^{++}}\}$ with $|\vec{p}| = 1$, computed between $t = 1 - 4$; the 2/1 projection on a 3×3 basis of $\{\mathcal{O}_1^{A_1^{++}}, \mathcal{O}_2^{A_1^{++}}, \mathcal{O}_3^{A_1^{++}}\}$ with $|\vec{p}| = 1$, computed between $t = 1 - 4$; and the 2/1 projection on a 3×3 basis of $\{\mathcal{O}_0'^{A_1^{++}}, \mathcal{O}_1'^{A_1^{++}}, \mathcal{O}_2'^{A_1^{++}}\}$ with $|\vec{p}| = 0$, computed between $t = 2 - 4$. The differences between these 4 estimates are used to determine the systematic error

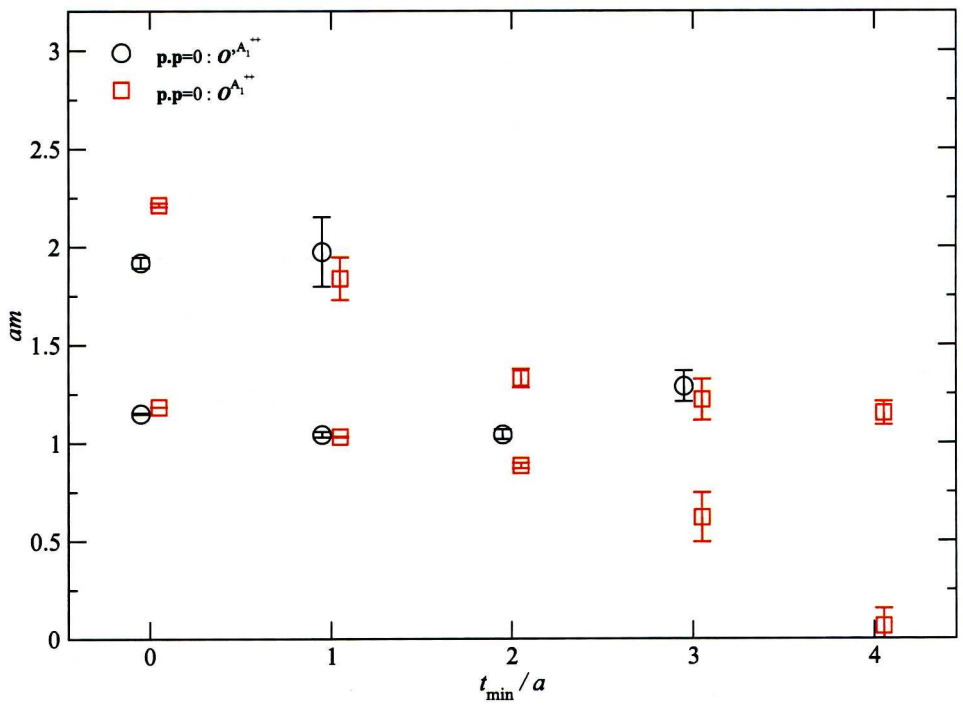

Figure 5.21: The ground and first-excited state for the two-exponential fits to a 4×4 basis of $\{\mathcal{O}_0^{A_1^{++}}, \mathcal{O}_1^{A_1^{++}}, \mathcal{O}_2^{A_1^{++}}, \mathcal{O}_3^{A_1^{++}}\}$ and a 3×3 basis of $\{\mathcal{O}_0'^{A_1^{++}}, \mathcal{O}_1'^{A_1^{++}}, \mathcal{O}_2'^{A_1^{++}}\}$ for $|\vec{p}| = 0$ with a varying t_{min} and t_{max} fixed at $t = 6$ for both. The fit to the $\mathcal{O}^{A_1^{++}}$ correlators was performed using a fully correlated method and the fit to the $\mathcal{O}'^{A_1^{++}}$ correlators using an uncorrelated method.

- the masses extracted from the variational eigenvalues for a 3×3 matrix of correlators formed using the bases of operators $\{\mathcal{O}_0^{A_1^{++}}, \mathcal{O}_2^{A_1^{++}}, \mathcal{O}_3^{A_1^{++}}\}$ and $\{\mathcal{O}_1^{A_1^{++}}, \mathcal{O}_2^{A_1^{++}}, \mathcal{O}_3^{A_1^{++}}\}$ for the $|\vec{p}| = 0$ and $|\vec{p}| = 1$ correlators respectively, where the projection is performed at $t/t_0 = 2/1$. We use the difference between the $|\vec{p}| = 0$ and $|\vec{p}| = 1$ results to estimate our systematic error.

- the masses extracted from the variational eigenvalues for a 3×3 matrix of correlators formed using the basis of handed operators $\{\mathcal{O}_0'^{A_1^{++}}, \mathcal{O}_1'^{A_1^{++}}, \mathcal{O}_2'^{A_1^{++}}\}$ projected at $t/t_0 = 2/1$. Here we have a statistical error only.

- the factorising fit results for two-exponential fits to a 4×4 basis of $|\vec{p}| = 0$ correlators formed using the operators $\{\mathcal{O}_0^{A_1^{++}}, \mathcal{O}_1^{A_1^{++}}, \mathcal{O}_2^{A_1^{++}}, \mathcal{O}_3^{A_1^{++}}\}$, and the same for $|\vec{p}| = 1$. The systematic error is computed as the standard error on the mean of the set of $|\vec{p}| = 0$ and $|\vec{p}| = 1$ results combined for $t_{\text{min}} = 1$ with $t_{\text{max}} = 4 - 8$.

- the factorising fit results for two-exponential fits to a 3×3 basis of handed operators $\{\mathcal{O}_0'^{A_1^{++}}, \mathcal{O}_1'^{A_1^{++}}, \mathcal{O}_2'^{A_1^{++}}\}$ for $|\vec{p}| = 0$. The systematic error is computed as the standard error on the mean of the fit results for $t_{\text{min}} = 1 - 2$ with $t_{\text{max}} = 6$.

These sources, along with their statistical and derived systematic errors (where appropriate), are presented in Tables 5.12, 5.13, 5.14, 5.15 and 5.16. Using the PDG weighted averaging procedure one obtains, using these five sources, the final value

$$am = 1.0468(75) \tag{5.9}$$

where the error is both statistical and systematic. This average is shown in Fig. 5.22 along with each of the four sources, where the statistical and systematic errors on the sources are combined.

The same procedure is carried out for the first-excited state, the sources shown in Fig. 5.23, obtaining a final value of

$$am^* = 1.875(87) \ . \tag{5.10}$$

The combined error obtained on the groundstate mass is noticeably small — less that 1% of the mass itself. Comparing this to the distribution of the sources as shown in Fig. 5.22 one might find this less than credibly small. The small error can be explained, however, by detailing the PDG weighted averaging procedure.

Source	Central Value	Statistical Error
2/1 proj., 3×3 basis $\{\mathcal{O}_0^{A_1^{++}}, \mathcal{O}_2^{A_1^{++}}, \mathcal{O}_3^{A_1^{++}}\}$, $\lvert\vec{p}\rvert = 0 : t = 2-5$	0.9229	0.0578
2/1 proj., 4×4 basis $\{\mathcal{O}_0^{A_1^{++}}, \mathcal{O}_1^{A_1^{++}}, \mathcal{O}_2^{A_1^{++}}, \mathcal{O}_3^{A_1^{++}}\}$, $\lvert\vec{p}\rvert = 1 : t = 1-4$	1.0525	0.0616
2/1 proj., 3×3 basis $\{\mathcal{O}_1^{A_1^{++}}, \mathcal{O}_2^{A_1^{++}}, \mathcal{O}_3^{A_1^{++}}\}$, $\lvert\vec{p}\rvert = 0 : t = 1-4$	1.0111	0.0246
2/1 proj., 3×3 basis $\{\mathcal{O}_0^{\prime A_1^{++}}, \mathcal{O}_1^{\prime A_1^{++}}, \mathcal{O}_2^{\prime A_1^{++}}\}$, $\lvert\vec{p}\rvert = 0 : t = 2-4$	1.0015	0.0752
Average$\pm$stat.$\pm$sys.		0.997$\pm$0.055$\pm$0.031

Table 5.12: The weighted averages on the variational effective masses for various bases of operators, as described in the text, along with a determination of the overall statistical and systematic errors.

Source	Central Value	Statistical Error
$\lvert\vec{p}\rvert = 0$ Eig.	1.04341	0.02120
$\lvert\vec{p}\rvert = 1$ Eig.	1.04462	0.02126
Average$\pm$stat.$\pm$sys.		1.044$\pm$0.021$\pm$0.009

Table 5.13: Masses extracted from the eigenvalues obtained from the solutions of the GEVP (4.17) for the 3×3 matrices of correlators formed using the bases of operators $\{\mathcal{O}_0^{A_1^{++}}, \mathcal{O}_2^{A_1^{++}}, \mathcal{O}_3^{A_1^{++}}\}$ and $\{\mathcal{O}_1^{A_1^{++}}, \mathcal{O}_2^{A_1^{++}}, \mathcal{O}_3^{A_1^{++}}\}$ for $\lvert\vec{p}\rvert = 0$ and $\lvert\vec{p}\rvert = 1$ respectively, at $t/t_0 = 2/1$.

Source	Central Value	Statistical Error
$\lvert\vec{p}\rvert = 0$ Eig.	1.044	0.020
Average$\pm$stat.$\pm$sys.		1.044$\pm$0.020$\pm-$

Table 5.14: Mass extracted from the eigenvalue obtained from the solution of the GEVP (4.17) for the 3×3 matrix of correlators formed using the basis of operators $\{\mathcal{O}_0^{\prime A_1^{++}}, \mathcal{O}_1^{\prime A_1^{++}}, \mathcal{O}_2^{\prime A_1^{++}}\}$ for $\lvert\vec{p}\rvert = 0$ at $t/t_0 = 2/1$.

Source	Central Value	Statistical Error
$\|\vec{p}\| = 0$, $t_{\max} = 4$	1.0364	0.0033
$\|\vec{p}\| = 0$, $t_{\max} = 5$	1.0339	0.0029
$\|\vec{p}\| = 0$, $t_{\max} = 6$	1.0336	0.0029
$\|\vec{p}\| = 0$, $t_{\max} = 7$	1.0335	0.0029
$\|\vec{p}\| = 0$, $t_{\max} = 8$	1.0328	0.0029
$\|\vec{p}\| = 1$, $t_{\max} = 4$	1.0777	0.0061
$\|\vec{p}\| = 1$, $t_{\max} = 5$	1.0785	0.0060
$\|\vec{p}\| = 1$, $t_{\max} = 6$	1.0770	0.0060
$\|\vec{p}\| = 1$, $t_{\max} = 7$	1.0758	0.0061
$\|\vec{p}\| = 1$, $t_{\max} = 8$	1.0753	0.0061
Average±stat.±sys.		1.0554±0.0045±0.0075

Table 5.15: Determination of systematic error on the groundstate mass for the two-exponential fits to a 4×4 matrix of correlators formed using the basis of operators $\{\mathcal{O}_0^{A_1^{++}}, \mathcal{O}_1^{A_1^{++}}, \mathcal{O}_2^{A_1^{++}}, \mathcal{O}_3^{A_1^{++}}\}$ with both $|\vec{p}| = 0$ and $|\vec{p}| = 1$ where the fits are performed with $t_{\min}$ fixed at $t = 1$.

Source	Central Value	Statistical Error
$\|\vec{p}\| = 0$, $t_{\min} = 1$	1.044	0.014
$\|\vec{p}\| = 0$, $t_{\min} = 2$	1.044	0.025
Average±stat.±sys.		1.044±0.012±−

Table 5.16: Determination of systematic error on the groundstate mass for the two-exponential fits to a 3×3 matrix of correlators formed using the basis of operators $\{\mathcal{O}_0'^{A_1^{++}}, \mathcal{O}_1'^{A_1^{++}}, \mathcal{O}_2'^{A_1^{++}}\}$ for $|\vec{p}| = 0$, where the fits are performed with $t_{\max}$ fixed at $t = 6$.

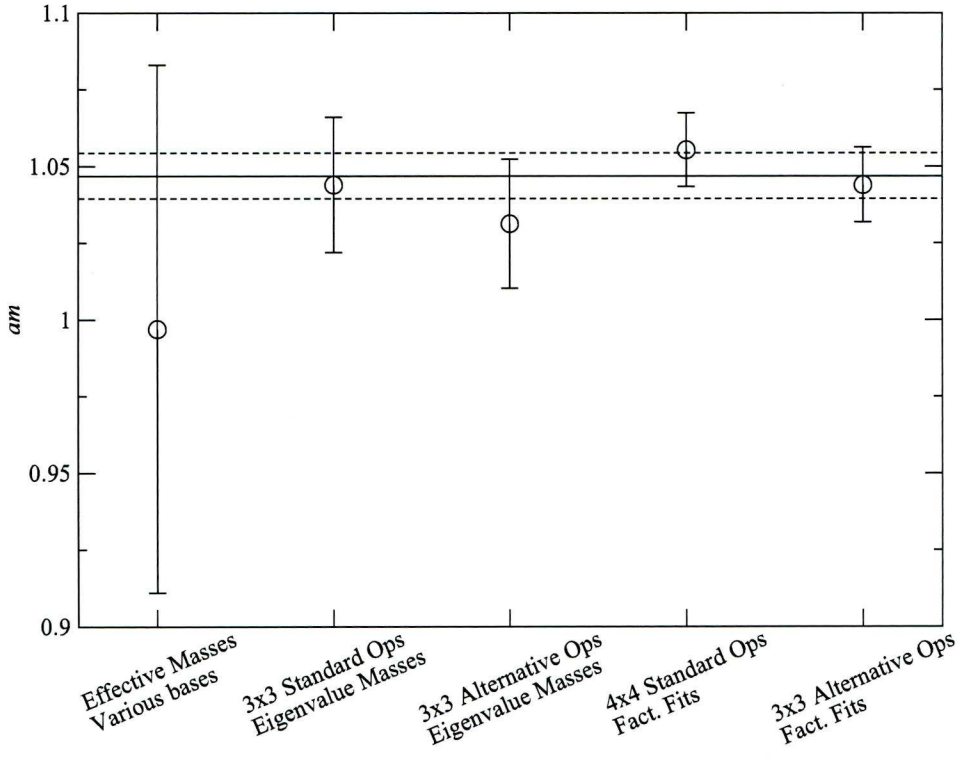

Figure 5.22: The overall average for the scalar glueball groundstate mass on the coarse lattices, computed as described in the text.

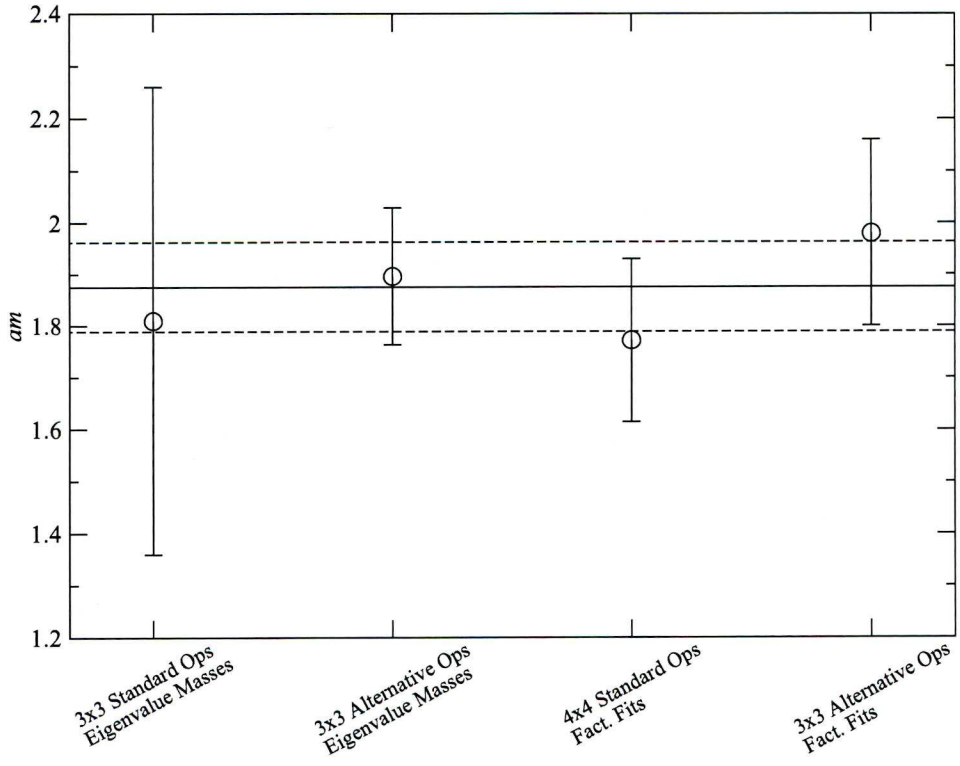

Figure 5.23: The overall average for the scalar glueball first excited-state mass on the coarse lattices, computed as described in the text.

Particle Data Group Weighted Averaging Procedure

The central value $\bar{x}$ of a set of N estimates x_i with associated overall statistical and systematic error δx_i is computed using

$$\bar{x} = \frac{\sum_i w_i x_i}{\sum_i w_i} \tag{5.11}$$

where the weights w_i are computed using $w_i = \frac{1}{(\delta x_i)^2}$, δx_i being the error on the ith estimate of x. The naïve error on $\bar{x}$, $\delta\bar{x}$, is simply computed as

$$\delta\bar{x} = \left(\sum_i^N w_i\right)^{-1/2} . \tag{5.12}$$

On then computes a value for $\chi^2 = \sum_i w_i(\bar{x} - x_i)^2$ which is compared with the expected value of $N - 1$.

- If $\chi^2/(N-1)$ is less than or equal to one then the error is accepted as is.
- If $\chi^2/(N-1)$ is large then the average and its error are taken to be poorly determined and should not be used or should be used with the utmost care.
- If $\chi^2/(N-1)$ is greater than one, but not large, then the average is still taken as it is but the error $\delta\bar{x}$ is multiplied by a scaling factor S which is computed as described below.

In the event that a scaling factor S is required and the errors on all sources are similar this is computed as

$$S = \left(\frac{\chi^2}{N-1}\right)^{1/2} . \tag{5.13}$$

If the sources have widely varying errors as in this case, χ^2 is recomputed with a threshold δ_0 for the maximum value of the error; data points with $\delta x_i > \delta_0$ are not used in the recomputation of χ^2. The scale S is then computed using this new χ^2 and an appropriately reduced value for N. Following [132] δ_0 is chosen to be $3N^{1/2}\delta\bar{x}$.

One should note that this thresholding procedure is only modifying the scaling factor S, preventing imprecise data from making S too large. A key assumption of the whole procedure is that the data is uncorrelated — as our estimates have all been computed using the same underlying configurations there will naturally be correlations between the estimates, however the degree to which this has effected the final error budget is left for further study.

One might also draw into question in the way in which seemingly systematic differences in results have been discarded — specifically those for the factorising fits in

Section 5.6. However we believe that we have presented enough evidence, particularly in §5.6.1, to show that the lower lying $am \sim 0.9$ masses were artefacts of poor quality fits and that to include them in an estimate of systematic error would be inappropriate.

Having obtained our value for the scalar glueball mass on the coarse lattices we now present the analysis for the scalar glueball correlators on the fine lattices.

5.7 Effective Mass Results

We proceed as for the coarse lattices and so present in Fig. 5.24 the effective masses for the diagonal entries of the 4×4 matrix of correlators formed using the basis of scalar glueball operators $\{\mathcal{O}_0^{A_1^{++}}, \mathcal{O}_1^{A_1^{++}}, \mathcal{O}_2^{A_1^{++}}, \mathcal{O}_3^{A_1^{++}}\}$ measured on the fine lattice with $|\vec{p}| = 0$. The weighted averages are shown for the correlators computed using $\mathcal{O}_2^{A_1^{++}}$ and $\mathcal{O}_3^{A_1^{++}}$, computed between $t = 2 - 5$ and $t = 3 - 6$.

The values (extended to include $t = 3 - 5$) are presented in Table. 5.17. Whilst the basis dependence certainly appears to be weaker than that exhibited by the coarse effective masses in Table 5.1 the dependence on the weighted averaging range seems to be slightly stronger.

Operators	t	am_{eff}
$\mathcal{O}_2^{A_1^{++}} \times \mathcal{O}_2^{A_1^{++}}$	$2 - 5$	0.736(30)
$\mathcal{O}_2^{A_1^{++}} \times \mathcal{O}_2^{A_1^{++}}$	$3 - 5$	0.646(60)
$\mathcal{O}_2^{A_1^{++}} \times \mathcal{O}_2^{A_1^{++}}$	$3 - 6$	0.624(63)
$\mathcal{O}_3^{A_1^{++}} \times \mathcal{O}_3^{A_1^{++}}$	$2 - 5$	0.716(30)
$\mathcal{O}_3^{A_1^{++}} \times \mathcal{O}_3^{A_1^{++}}$	$3 - 5$	0.638(53)
$\mathcal{O}_3^{A_1^{++}} \times \mathcal{O}_3^{A_1^{++}}$	$3 - 6$	0.653(58)

Table 5.17: Effective masses obtained from the weighted average of the effective mass computed using the correlator formed using the $|\vec{p}| = 0$ operators $\mathcal{O}^{A_1^{++}}$ measured on the fine lattices. The blocking level combination is given in column one, and the averaging window in column two.

5.7.1 Variational Effective Masses

We proceed immediately to study the eigenvalue spectrum of the variational projections using various bases of operators. As with the coarse lattices we look for the most stable projections, indicated by well determined spectra, and use the correlators constructed in these variationally projected bases to compute the effective mass. Furthermore we shall also use the eigenvalues to determine the masses using (4.19).

The eigenvalues obtained from various variational projections on a 4×4 matrix of correlators using a basis of operators $\{\mathcal{O}_0^{A_1^{++}}, \mathcal{O}_1^{A_1^{++}}, \mathcal{O}_2^{A_1^{++}}, \mathcal{O}_3^{A_1^{++}}\}$ are presented

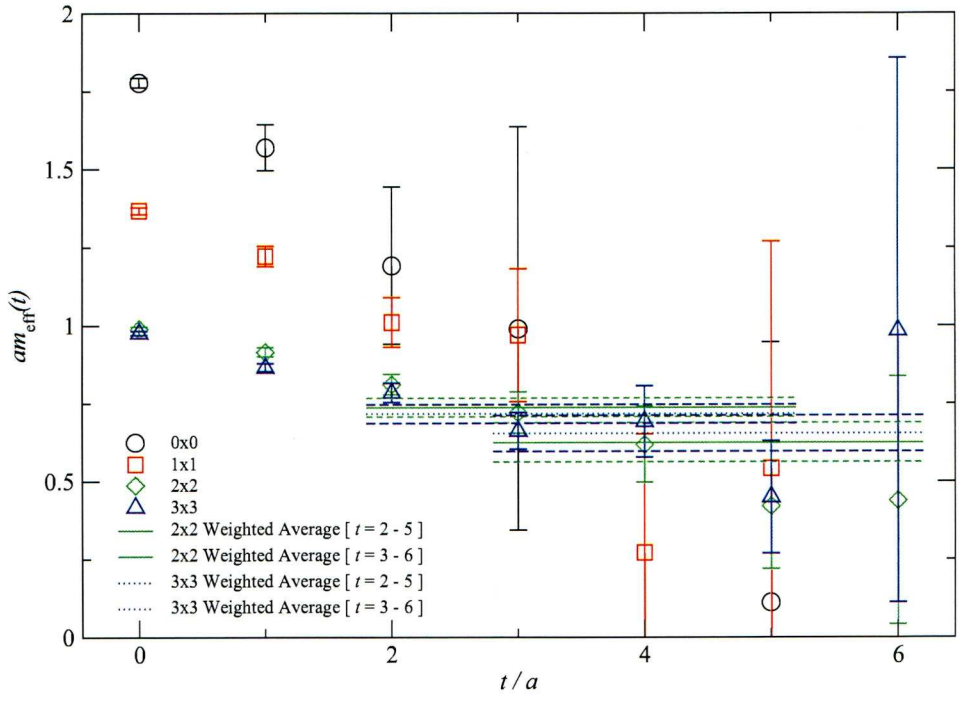

Figure 5.24: The effective masses for the diagonal entries of a 4×4 matrix of correlators formed using the $|\vec{p}| = 0$ operators $\mathcal{O}_i^{A_1^{++}}$ on the fine lattices. The weighted averages for blocking levels 2 and 3 are shown, computed from $t = 2 - 5$ and $t = 3 - 6$.

in Table 5.18, where the errors are determined by a bootstrapping procedure over 50 samples. Here we see that the stability is certainly improved for both the 1/0 and 2/1 projections, although one must bear in mind that these correspond to smaller physical distances on the fine lattice than they do on the coarse ($2a \sim 0.18$ fm on the fine lattices, *cf.* 0.24 fm on the coarse). That the 3/2 projection on the fine lattices appears to be more unstable than the 3/2 projection on the coarse lattices, primarily due to the poor determination of λ^0, is perhaps a reflection of the reduction in statistics. Of course we must bear in mind the effects of self-averaging here — whilst there are certainly fewer configurations in the fine ensemble than in the coarse due to the larger spatial extent we have more determinations of the glueball operators per timeslice (at the zeroth Teper blocking level the sum over $\vec{x}$ in (5.1) takes in 32^3 sites per timeslice on the fine lattices, compared to 24^3 on the coarse). One might expect that this self-averaging would serve to cancel out any sample-size difference, if not even go as far as to improve our signal.

The effective masses using the correlators obtained from the 1/0, 2/1 and 3/1 projections are presented in Fig. 5.25, as are the weighted averages of the effective masses for the 2/1 and 3/1 projections computed from $t = 3 - 5$: $am = 0.641(57)$ and $am = 0.635(55)$ respectively. If one compares these to the masses extracted from the eigenvalues presented in Table 5.19 these seem quite low — the eigenvalue masses seem to favour a value $am \sim 0.88$. The lowest mass obtained from the eigenvalue spectrum,

t/t_0	λ^0	λ^1	λ^2	λ^3
1/0	0.3879(83)	0.2001(50)	0.1278(33)	0.0608(26)
2/1	0.415(10)	0.247(12)	0.187(24)	0.064(32)
3/2	9(1)	0.48(11)	0.27(27)	0.20(69)
2/0	0.3879(83)	0.2000(50)	0.1248(33)	0.0608(26)
3/0	0.0740(27)	0.0099(23)	0.0001(2)	-0.003(2)
3/1	0.1890(77)	0.069(15)	0.003(15)	-0.094(30)
4/1	0.097(11)	0.088(21)	0.005(15)	-0.015(18)
4/2	2(2)	0.258(62)	0.10(12)	0(10)

Table 5.18: Eigenvalues obtained from the solution of the GEVP at the specified t/t_0. Fine 4×4 basis of $|\vec{p}| = 0$ $\mathcal{O}^{A_1^{++}}$ operators.

$am_0 = 0.32(28)$, corresponds to the 4/2 projection and compares well with the mass of a 2π state on the fine lattices ($2am_\pi = 0.3264(14)$) although the large statistical error obscures a direct comparison.

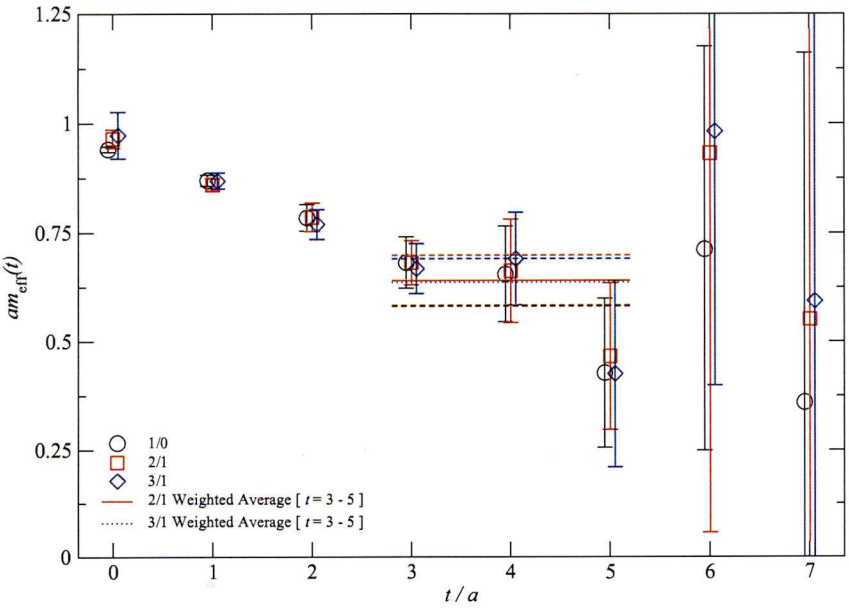

Figure 5.25: Effective masses computed using the variational correlator as defined in (4.18) for different choices of t/t_0, projecting from a 4×4 matrix of correlators constructed using $\{\mathcal{O}_0^{A_1^{++}}, \mathcal{O}_1^{A_1^{++}}, \mathcal{O}_2^{A_1^{++}}, \mathcal{O}_3^{A_1^{++}}\}$ measured on the fine lattices with $|\vec{p}| = 0$. The weighted averages are shown for the 2/1 and 3/1 projections where the errors are computed using a bootstrap procedure with $N_{\rm BS} = 50$.

Basis Experimentation

In order to attempt to resolve the lower lying states from the variational eigenvalue spectrum we perform the variational projection on smaller 3×3 bases of operators. We find the basis of operators $\{\mathcal{O}_1^{A_1^{++}}, \mathcal{O}_2^{A_1^{++}}, \mathcal{O}_3^{A_1^{++}}\}$ gives the most stable projection, with

t/t_0	$am(\lambda^0)$	$am(\lambda^1)$	$am(\lambda^2)$	$am(\lambda^3)$
1/0	0.947(20)	1.609(36)	2.081(45)	2.800(70)
2/1	0.879(22)	1.398(52)	1.68(16)	3(1)
3/2	2.21(39)	0.73(50)	1(1)	2(1)
2/0	0.908(21)	1.540(40)	2.011(79)	2.90(67)
3/0	0.878(20)	1.540(68)	2.30(39)	0(1)
3/1	0.833(24)	1.34(12)	2.87(45)	0(1)
4/1	0.776(37)	0.81(14)	1.74(55)	0(1)
4/2	0.32(28)	0.68(17)	1.15(58)	0(1)

Table 5.19: Masses extracted using (4.19) from the eigenvalues obtained from the solution of the GEVP at the specified t/t_0. Fine 4×4 basis of $|\vec{p}| = 0$ $\mathcal{O}^{A_1^{++}}$ operators.

the eigenvalues and masses determined from these presented in Table 5.20. Again the projections appear to become unstable as we increase t — whilst the $am = 0.60(10)$ state shown for the 4/2 projection could correspond to a decay channel the statistical error and poorly determined remaining masses prevent us from identifying it as such.

t/t_0	λ^0	$am(\lambda^0)$	λ^1	$am(\lambda^1)$	λ^2	$am(\lambda^2)$
1/0	0.3879(84)	0.947(20)	0.2011(46)	1.604(35)	0.1246(35)	2.082(45)
2/1	0.426(11)	0.854(22)	0.224(11)	1.496(52)	0.147(17)	1.91(14)
3/2	0.476(17)	0.742(34)	0.447(66)	0.80(25)	0.17(14)	2(1)
2/0	0.1632(40)	0.906(20)	0.0449(27)	1.551(40)	0.0160(21)	2.068(77)
3/0	0.0754(32)	0.862(21)	0.0128(27)	1.452(98)	0.0019(25)	1.73(92)
3/1	0.1951(78)	0.816(24)	0.049(11)	1.51(12)	0.016(18)	2(1)
4/1	0.0994(75)	0.770(28)	0.046(16)	1.03(29)	0(0)	2.51(87)
4/2	0.304(65)	0.60(10)	0.230(66)	0.74(34)	−0.08(8)	0.24(61)

Table 5.20: Eigenvalues obtained from the solution of the GEVP at the specified t/t_0, and masses extracted using (4.19). Fine 3×3 basis of $\{\mathcal{O}_1^{A_1^{++}}, \mathcal{O}_2^{A_1^{++}}, \mathcal{O}_3^{A_1^{++}}\}$ operators with $|\vec{p}| = 0$ measured on the fine lattices.

5.8 Effective Mass Results: $|\vec{p}| = 1$

In Table 5.21 we present the results for the weighted average computed over the ranges $t = 3-5$ and $t = 3-6$ for the correlators corresponding to the diagonal entries of a 4×4 matrix of correlators formed from the basis of $|\vec{p}| = 1$ operators $\{\mathcal{O}_0^{A_1^{++}}, \mathcal{O}_1^{A_1^{++}}, \mathcal{O}_2^{A_1^{++}}, \mathcal{O}_3^{A_1^{++}}\}$. The statistical errors on the effective masses computed using the correlators formed using the $\mathcal{O}_0^{A_1^{++}}$ and $\mathcal{O}_1^{A_1^{++}}$ operators are large, those corresponding to the $\mathcal{O}_0^{A_1^{++}}$ being consistent with zero. The results for the effective masses of the correlators formed using the $\mathcal{O}_2^{A_1^{++}}$ and $\mathcal{O}_3^{A_1^{++}}$ operators have more acceptable statistical errors and are consistent with their $|\vec{p}| = 0$ counterparts as shown in Fig. 5.26.

Operators	t	aE_{eff}	am_{eff}
$\mathcal{O}_0^{A_1^{++}} \times \mathcal{O}_0^{A_1^{++}}$	$3-5$	0.46(50)	0.42(55)
$\mathcal{O}_0^{A_1^{++}} \times \mathcal{O}_0^{A_1^{++}}$	$3-6$	0.33(44)	0.27(55)
$\mathcal{O}_1^{A_1^{++}} \times \mathcal{O}_1^{A_1^{++}}$	$3-5$	0.98(38)	0.96(39)
$\mathcal{O}_1^{A_1^{++}} \times \mathcal{O}_1^{A_1^{++}}$	$3-6$	0.82(35)	0.80(36)
$\mathcal{O}_2^{A_1^{++}} \times \mathcal{O}_2^{A_1^{++}}$	$3-5$	0.745(81)	0.719(84)
$\mathcal{O}_2^{A_1^{++}} \times \mathcal{O}_2^{A_1^{++}}$	$3-6$	0.703(87)	0.676(91)
$\mathcal{O}_3^{A_1^{++}} \times \mathcal{O}_3^{A_1^{++}}$	$3-5$	0.670(66)	0.641(69)
$\mathcal{O}_3^{A_1^{++}} \times \mathcal{O}_3^{A_1^{++}}$	$3-6$	0.631(67)	0.600(70)

Table 5.21: Effective masses obtained from the weighted average of the effective masses computed using the correlators formed using the $|\vec{p}| = 1$ operators $\mathcal{O}^{A_1^{++}}$ measured on the fine lattices. The operators used are given in column one, and the averaging window in column two.

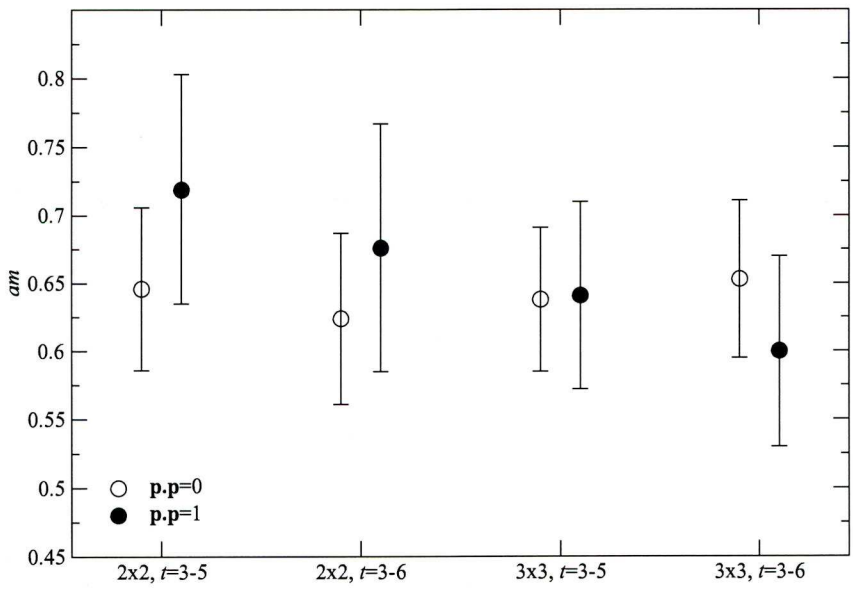

Figure 5.26: A comparison of the weighted averages of the effective masses computed using the 2×2 and 3×3 correlators of $\mathcal{O}_i^{A_1^{++}}$ at both $|\vec{p}| = 0$ and $|\vec{p}| = 1$. The labels denote the blocking levels and weighted averaging range used.

5.8.1 Variational Effective Masses

In an attempt to obtain a more reliable plateau we perform variational projections from the 4×4 matrix of correlators, formed using the basis of operators $\{\mathcal{O}_0^{A_1^{++}}, \mathcal{O}_1^{A_1^{++}}, \mathcal{O}_2^{A_1^{++}}, \mathcal{O}_3^{A_1^{++}}\}$ with $|\vec{p}| = 1$, at various t/t_0. The results of these projections are presented in Fig. 5.27, where it appears that for $t_0 > 0$ the projections are particularly unstable (the eigenvalues are presented in Table. 5.22). There is no *a priori* reason variational projections using $|\vec{p}| = 1$ correlators should be any less stable than those using $|\vec{p}| = 0$ correlators, although we note that in the case of the coarse lattices we were unable to use the 3/2 projection for the $|\vec{p}| = 1$ correlators, in contrast to the $|\vec{p}| = 0$ correlators. It has been found for both the coarse ($|\vec{p}| = 0$ and $|\vec{p}| = 1$) and fine lattices ($|\vec{p}| = 0$) that variational projections using 3×3 matrices are more stable and we therefore attempt a variational analysis using such a basis.

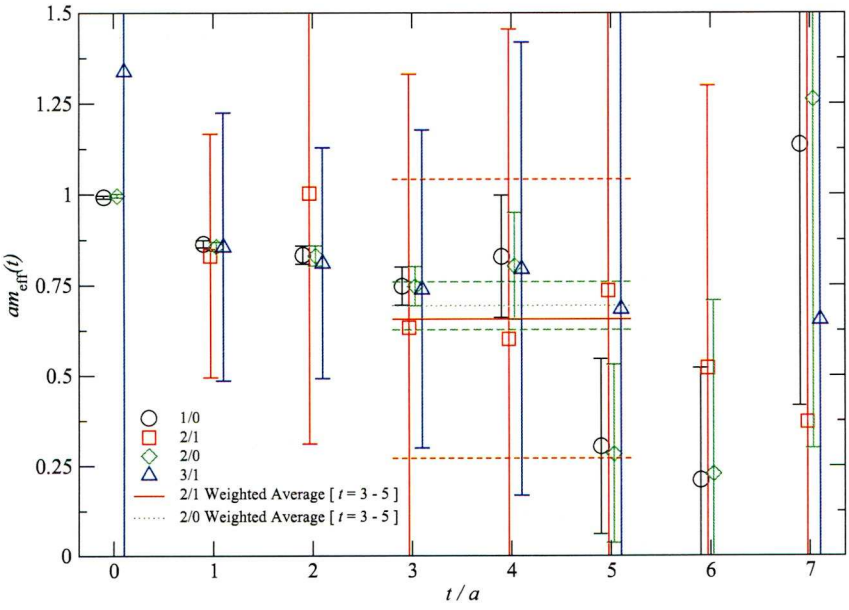

Figure 5.27: Effective masses computed using the variational correlator as defined in (4.18) for different choices of t/t_0, projecting from a 4×4 matrix of correlators constructed using $\{\mathcal{O}_0^{A_1^{++}}, \mathcal{O}_1^{A_1^{++}}, \mathcal{O}_2^{A_1^{++}}, \mathcal{O}_3^{A_1^{++}}\}$ measured on the fine lattices with $|\vec{p}| = 1$. The weighted averages are shown for the 2/1 and 2/0 projections where the errors are computed using a bootstrap procedure with $N_{\text{BS}} = 50$.

t/t_0	λ^0	λ^1	λ^2	λ^3
1/0	0.3579(76)	0.1693(38)	0.0614(19)	0.0014(15)
2/1	0.42(56)	0.288(62)	0.127(78)	0(3)
3/2	0(13)	0.33(18)	0.25(24)	-1(2)
2/0	0.1483(35)	0.0439(19)	0(0)	0(0)

Table 5.22: Eigenvalues obtained from the solution of the GEVP at the specified t/t_0. Fine 4×4 basis of $|\vec{p}| = 1$ $\mathcal{O}^{A_1^{++}}$ operators.

Basis Experimentation

Variational projections were carried out on several 3×3 matrices of correlators (formed from the bases of $|\vec{p}| = 1$ operators $\{\mathcal{O}_0^{A_1^{++}}, \mathcal{O}_1^{A_1^{++}}, \mathcal{O}_2^{A_1^{++}}\}$, $\{\mathcal{O}_0^{A_1^{++}}, \mathcal{O}_1^{A_1^{++}}, \mathcal{O}_3^{A_1^{++}}\}$, $\{\mathcal{O}_0^{A_1^{++}}, \mathcal{O}_2^{A_1^{++}}, \mathcal{O}_3^{A_1^{++}}\}$ and $\{\mathcal{O}_1^{A_1^{++}}, \mathcal{O}_2^{A_1^{++}}, \mathcal{O}_3^{A_1^{++}}\}$) for a number of different t/t_0. The $\{\mathcal{O}_1^{A_1^{++}}, \mathcal{O}_2^{A_1^{++}}, \mathcal{O}_3^{A_1^{++}}\}$ basis of operators was again found to provide the most stable projections in terms of the eigenvalue distribution.

The eigenvalues and masses[7] extracted from them are presented in Table 5.23. One can see that these rapidly become unstable, although in order to make a direct comparison with the $|\vec{p}| = 0$ basis presented in Table 5.20 we present the masses $am(\lambda^\alpha)$ for both the $|\vec{p}| = 0$ and $|\vec{p}| = 1$ bases in Fig. 5.28 for a large number of t/t_0. Here not only is there good consistency between the $|\vec{p}| = 0$ and $|\vec{p}| = 1$ results for the same t/t_0 but the variation with increasing t/t_0 is relatively weak which, when compared with the coarse results presented in Fig. 5.9, appears to be consistent.

t/t_0	λ^0	$am(\lambda^0)$	λ^1	$am(\lambda^1)$	λ^2	$am(\lambda^2)$
1/0	0.3572(76)	1.011(21)	0.1726(39)	1.746(37)	0.0596(19)	2.815(62)
2/1	0.4083(96)	0.874(21)	0.257(11)	1.345(44)	0.071(26)	2.64(48)
3/2	1(5)	0.64(46)	0.43(10)	0.81(18)	0(5)	0(1)
2/0	0.1453(37)	0.944(21)	0.0471(20)	1.516(37)	0.002(1)	3.13(21)
3/0	0.0582(25)	0.927(22)	0.0140(17)	1.409(47)	0(0)	0(1)
3/1	0.1757(63)	0.847(23)	0.0943(97)	1.164(59)	-0.016(24)	0(1)
4/1	0.0804(53)	0.817(27)	0.0487(97)	0.989(84)	0(0)	2.52(91)

Table 5.23: Eigenvalues obtained from the solution of the GEVP at the specified t/t_0, and masses extracted using (4.19). Fine 3×3 basis of $\{\mathcal{O}_1^{A_1^{++}}, \mathcal{O}_2^{A_1^{++}}, \mathcal{O}_3^{A_1^{++}}\}$ operators with $|\vec{p}| = 1$ measured on the fine lattices.

5.8.2 Alternative Operators

In Fig. 5.29 we present the variational effective masses for the projection from the 3×3 matrix of correlators formed using the basis of $|\vec{p}| = 0$ operators $\{\mathcal{O}_0'^{A_1^{++}}, \mathcal{O}_1'^{A_1^{++}}, \mathcal{O}_2'^{A_1^{++}}\}$ performed at various t/t_0. The weighted averages computed for the 1/0 and 2/1 projections performed betweeen $t = 3$ and $t = 5$ are also shown: $am = 0.673(60)$ and $am = 0.690(81)$ respectively. These seem low when compared with the masses extracted from the eigenvalues, presented in Table 5.24 and shown against those obtained from the equivalent projections using the $|\vec{p}| = 0$ basis of operators $\{\mathcal{O}_1^{A_1^{++}}, \mathcal{O}_2^{A_1^{++}}, \mathcal{O}_3^{A_1^{++}}\}$ in Fig. 5.30.

[7] These have been converted from energies to masses using (5.8).

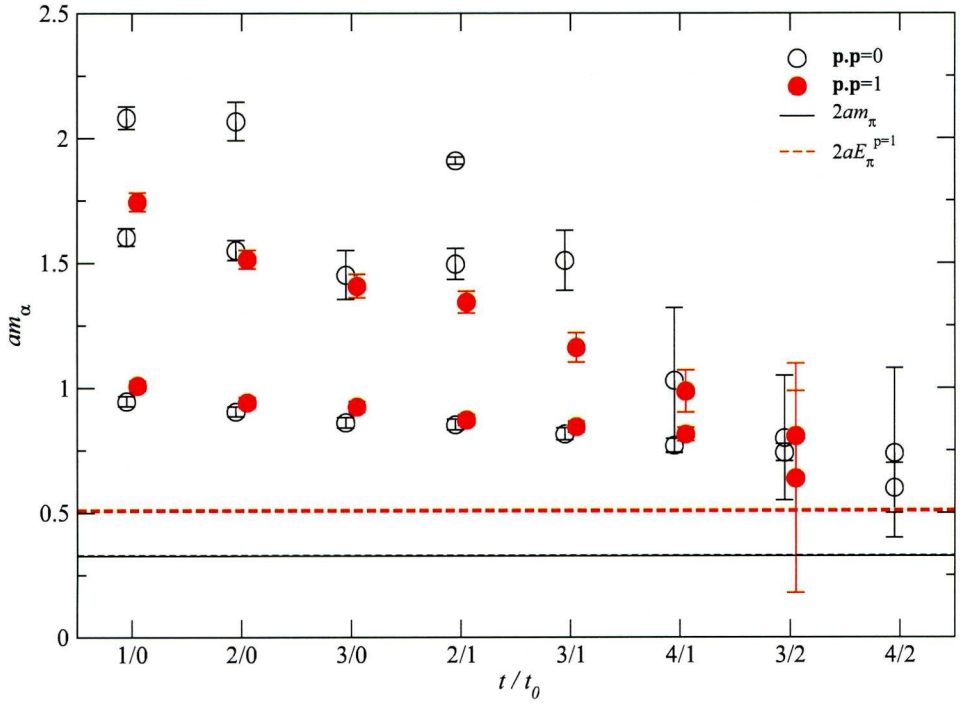

Figure 5.28: The masses extracted from the variational eigenvalues for different t/t_0 using the $|\vec{p}| = 0$ basis of operators $\{\mathcal{O}_1^{A_1^{++}}, \mathcal{O}_2^{A_1^{++}}, \mathcal{O}_3^{A_1^{++}}\}$ and the $|\vec{p}| = 1$ basis of operators $\{\mathcal{O}_1^{A_1^{++}}, \mathcal{O}_2^{A_1^{++}}, \mathcal{O}_3^{A_1^{++}}\}$ on the fine lattices. The errors are obtained using a bootstrap procedure with $N_{\mathrm{BS}} = 50$. Missing points correspond to negative or very poorly determined eigenvalues. The energies corresponding to a $\pi\pi$ state with $|\vec{p}| = 0$ and $|\vec{p}| = 1$ are drawn for comparision.

t/t_0	λ^0	$am(\lambda^0)$	λ^1	$am(\lambda^1)$	λ^2	$am(\lambda^2)$
1/0	0.3940(87)	0.932(21)	0.1826(49)	1.701(39)	0.0979(40)	2.324(64)
2/1	0.432(12)	0.838(25)	0.214(18)	1.543(92)	0.107(28)	2.24(31)
3/2	0.50(12)	0.70(19)	0.220(79)	1.52(26)	0(1)	4(1)
2/0	0.1668(47)	0.895(21)	0.0369(34)	1.650(56)	0.0074(25)	2.45(13)
3/0	0.0818(38)	0.834(23)	0.0105(33)	1.52(10)	0(0)	0(1)
3/1	0.1959(92)	0.815(26)	0.051(20)	1.49(14)	0.01(3)	2.4(9)
4/1	0.108(14)	0.742(47)	0.041(25)	1.07(20)	0(0)	0(1)

Table 5.24: Eigenvalues obtained from the solution of the GEVP at the specified t/t_0, and masses extracted using (4.19). Fine 3×3 basis of $\{\mathcal{O}_0'^{A_1^{++}}, \mathcal{O}_1'^{A_1^{++}}, \mathcal{O}_2'^{A_1^{++}}\}$ operators with $|\vec{p}| = 0$ measured on the fine lattices.

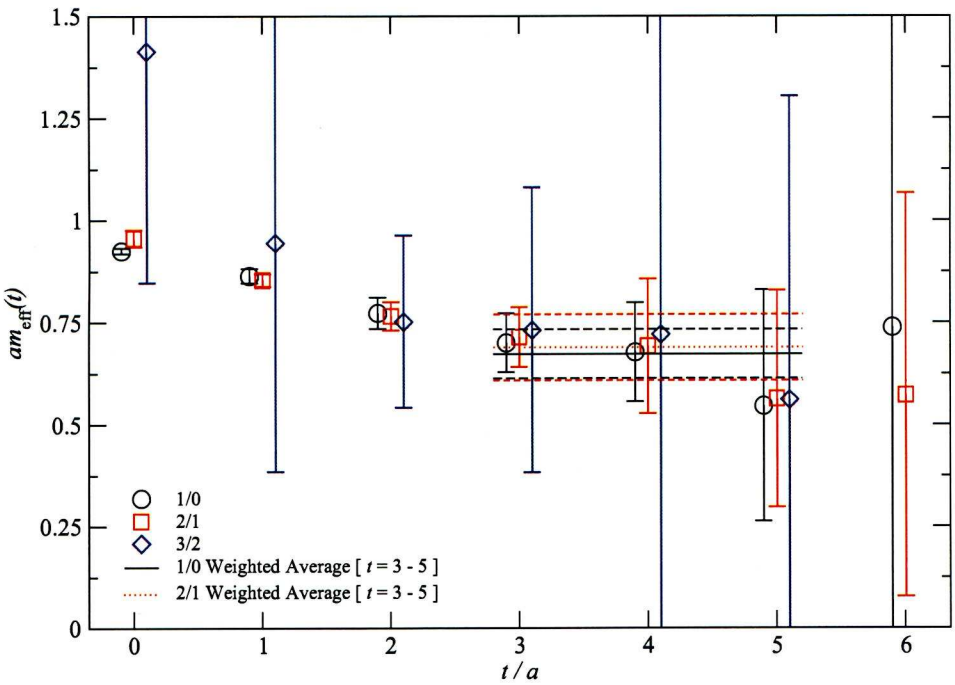

Figure 5.29: The effective masses computed using the variational correlators obtained using projections performed at the specified t/t_0 on a 3×3 basis of operators $\{\mathcal{O}_0^{\prime A_1^{++}}$, $\mathcal{O}_1^{\prime A_1^{++}}$, $\mathcal{O}_2^{\prime A_1^{++}}\}$ measured with $|\vec{p}| = 0$ on the fine lattices. The weighted averages performed between $t = 3$ and $t = 5$ are shown for the 1/0 and 2/1 projections.

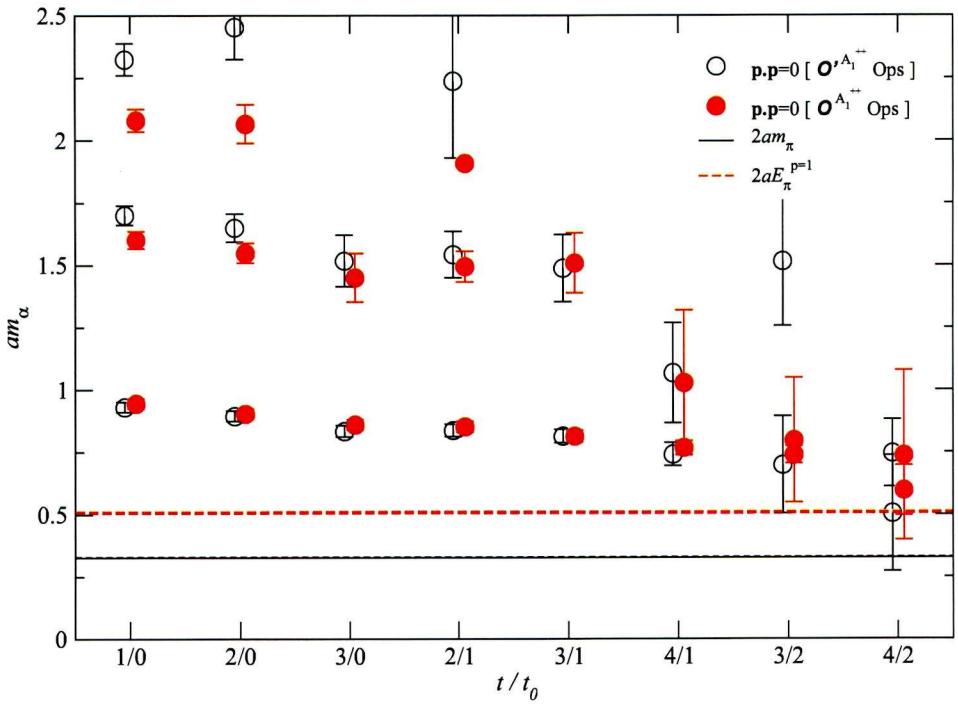

Figure 5.30: The masses extracted from the variational eigenvalues for different t/t_0 using the $|\vec{p}| = 0$ basis of operators $\{\mathcal{O}_1^{A_1^{++}}, \mathcal{O}_2^{A_1^{++}}, \mathcal{O}_3^{A_1^{++}}\}$ and the basis of alternative operators $\{\mathcal{O}_0'^{A_1^{++}}, \mathcal{O}_1'^{A_1^{++}}, \mathcal{O}_2'^{A_1^{++}}\}$ on the fine lattices. The errors are obtained using a bootstrap procedure with $N_{\mathrm{BS}} = 50$. Missing points correspond to negative or very poorly determined eigenvalues. The energies corresponding to a $\pi\pi$ state with $|\vec{p}| = 0$ and $|\vec{p}| = 1$ are drawn for comparision.

5.8.3 Comparison of Mass Estimates

In Fig. 5.31 we present a compilation of the results obtained using the weighted averaging procedure and the variational eigenvalues procedure. These are, from left to right:

- Weighted average ($t = 3 - 5$) of the variational effective mass from the 2/1 projection on a 4×4 basis of $\{\mathcal{O}_0^{A_1^{++}}, \mathcal{O}_1^{A_1^{++}}, \mathcal{O}_2^{A_1^{++}}, \mathcal{O}_3^{A_1^{++}}\}$ with $|\vec{p}| = 0$ — $am = 0.641(57)$.

- Weighted average ($t = 3 - 5$) of the variational effective mass from the 2/0 projection on a 4×4 basis of $\{\mathcal{O}_0^{A_1^{++}}, \mathcal{O}_1^{A_1^{++}}, \mathcal{O}_2^{A_1^{++}}, \mathcal{O}_3^{A_1^{++}}\}$ with $|\vec{p}| = 1$ — $am = 0.692(66)$.

- Weighted average ($t = 3 - 5$) of the variational effective mass from the 2/1 projection on a 3×3 basis of $\{\mathcal{O}_0'^{A_1^{++}}, \mathcal{O}_1'^{A_1^{++}}, \mathcal{O}_2'^{A_1^{++}}\}$ with $|\vec{p}| = 0$ — $am = 0.690(81)$.

- Masses extracted from the ground and first excited state eigenvalues from the 2/1 projection of a 3×3 basis of $\{\mathcal{O}_1^{A_1^{++}}, \mathcal{O}_2^{A_1^{++}}, \mathcal{O}_3^{A_1^{++}}\}$ with $|\vec{p}| = 0$ — $am = 0.854(22)$, $am^* = 1.496(52)$.

- Masses extracted from the ground and first excited state eigenvalues from the 3/0 projection of a 3×3 basis of $\{\mathcal{O}_1^{A_1^{++}}, \mathcal{O}_2^{A_1^{++}}, \mathcal{O}_3^{A_1^{++}}\}$ with $|\vec{p}| = 0$ — $am = 0.862(21)$, $am^* = 1.452(98)$.

- Masses extracted from the ground and first excited state eigenvalues from the 2/1 projection of a 3×3 basis of $\{\mathcal{O}_1^{A_1^{++}}, \mathcal{O}_2^{A_1^{++}}, \mathcal{O}_3^{A_1^{++}}\}$ with $|\vec{p}| = 1$ — $am = 0.874(21)$, $am^* = 1.345(44)$.

- Masses extracted from the ground and first excited state eigenvalues from the 2/1 projection of a 3×3 basis of $\{\mathcal{O}_0'^{A_1^{++}}, \mathcal{O}_1'^{A_1^{++}}, \mathcal{O}_2'^{A_1^{++}}\}$ with $|\vec{p}| = 0$ — $am = 0.838(25)$, $am^* = 1.543(92)$.

There is a slight difference between those masses obtained using the effective mass procedure and those obtained using the variational eigenvalues. We believe this inconsistency to be caused by lower lying states, potentially corresponding to decay channels — the groundstate variational eigenvalue for projections at large t seems to show consistency with a $\pi\pi$ state (Fig. 5.28). We were able to resolve this low lying state on the coarse lattices with reasonable accuracy by performing factorising fits, and therefore we should attempt to do the same for the fine lattices.

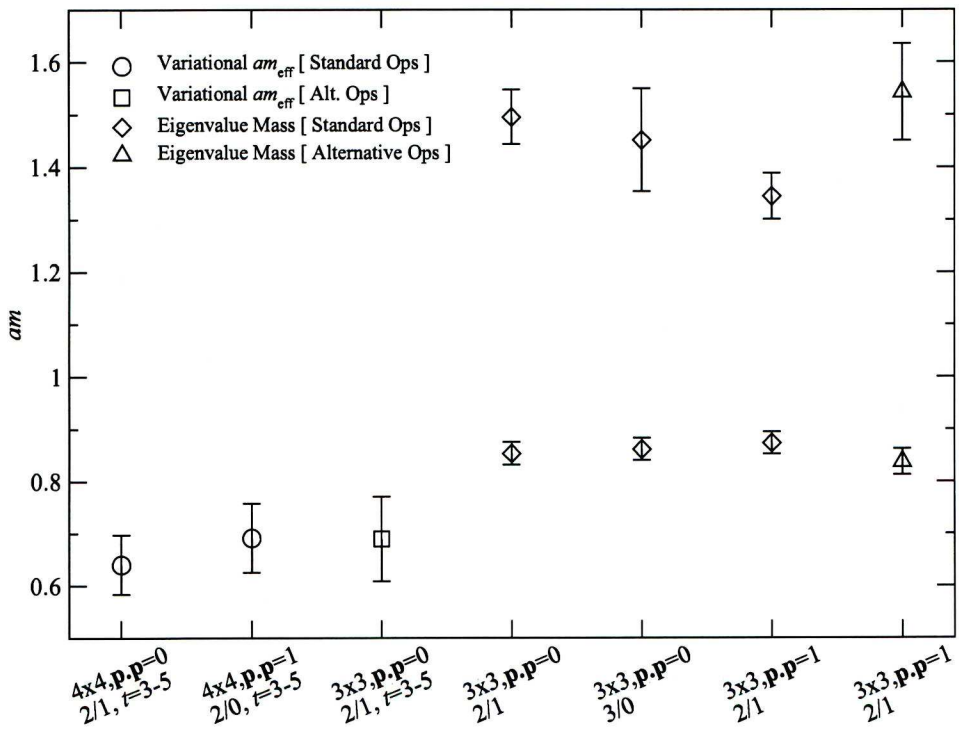

Figure 5.31: Comparison of mass estimates obtained for the scalar glueball using different methods (effective masses and variational eigenvalues) for the fine lattices. The points are described briefly on the axis and a more detailed description is given in the text (§5.8.3).

5.9 Factorising Fit Results

As with the coarse scalar glueball factorising fits we begin by performing fully correlated factorising fits a 4×4 matrix of correlators, using the basis of scalar glueball operators $\{\mathcal{O}_0^{A_1^{++}}, \mathcal{O}_1^{A_1^{++}}, \mathcal{O}_2^{A_1^{++}}, \mathcal{O}_3^{A_1^{++}}\}$ for both $|\vec{p}| = 0$ and $|\vec{p}| = 1$. Varying both the fit ranges and number of exponentials our criteria for a good fit remain the same, *i.e.* that the χ^2/d.o.f. is near to one and that the resulting parameters are reasonably stable with respect to changes in the fit range.

The results for the 4×4 factorising fits with $t_{\text{max}} = 7$ and $t_{\text{max}} = 8$ are presented in Tables 5.25 and 5.26 respectively, for $N_{\text{exp}} = 2$ and $N_{\text{exp}} = 3$ at both $|\vec{p}| = 0$ and $|\vec{p}| = 1$. We note that the majority of the fits are rather poor, particularly when compared with the coarse factorising fits — the three-exponential fits appear over-parameterised for $t_{\text{min}} > 2$ and errors are undetermined for a large number of parameters, indeed there are very few fits in which all parameters are well determined. This motivates us to perform uncorrelated factorising fits to the same matrix of correlators to determine if the cause of the poor fits is instability stemming from the use of correlated fits.

N_{exp}	$\lvert\vec{p}\rvert$	t_{min}	t_{max}	am_0	am_1	am_2	χ^2/d.o.f.
2	0	1	7	0.8170(9)	19.16[−]	—	6.747
		2	7	0.6906(29)	2.04[−]	—	1.868
		3	7	0[−]	0.767(12)	—	0.477
		4	7	0.5636(70)	1.78×10^5[−]	—	0.791
		5	7	0.455(13)	9.98[−]	—	0.502
2	1	1	7	0.8446(13)	19.00[−]	—	3.838
		2	7	0.8074(38)	1.302(66)	—	0.522
		3	7	0[−]	0.86[−]	—	0.376
		4	7	0.69[−]	1.79×10^5	—	0.540
		5	7	0.34(20)	9.98[−]	—	0.06
3	0	1	7	0.6518(30)	1.3337(66)	16.6[−]	2.495
		2	7	0.110(41)	0.8025(66)	1.68[−]	0.396
		3	7	0[−]	0.700(11)	8.31[−]	0.253
		4	7	0[−]	0.623(28)	6.743(61)	0.265
		5	7	0[−]	0.610(30)	1.67×10^3	0.295
3	1	1	7	0.8319(20)	1.366(13)	18.17[−]	0.642
		2	7	0[−]	0.8845(48)	1.127(57)	0.156
		3	7	0[−]	0.842(14)	10.532(16)	0.214
		4	7	0.26[−]	1.0287(92)	3.202(23)	0.03
		5	7	0[−]	0.39(52)	1.67×10^3	0.05

Table 5.25: Fitted mass parameters for two and three-exponential fully correlated factorising fits to a 4×4 matrix of correlators using a basis of operators $\{\mathcal{O}_0^{A_1^{++}}, \mathcal{O}_1^{A_1^{++}}, \mathcal{O}_2^{A_1^{++}}, \mathcal{O}_3^{A_1^{++}}\}$ with $|\vec{p}| = 0$ and $|\vec{p}| = 1$ for varying t_{min} with t_{max} fixed at $t = 7$. Where errors are quoted as [−] this indicates that the gradient in that direction of parameter space could not be determined, *i.e.* that the parameter is essentially free.

N_{exp}	$\lvert\vec{p}\rvert$	t_{min}	t_{max}	am_0	am_1	am_2	χ^2/d.o.f.
2	0	1	8	0.81647(92)	1.77[−]	—	6.515
		2	8	0.6224(33)	1.49[−]	—	2.194
		3	8	0.6415(34)	52.72[−]	—	1.607
		4	8	0.5399(63)	9.70×10^4[−]	—	1.152
		5	8	0.420(11)	11.61[−]	—	0.746
		6	8	0.397(23)	4.21[−]	—	0.720
2	1	1	8	0.8446(13)	18.93[−]	—	3.368
		2	8	0.8076(38)	1.314(65)	—	0.475
		3	8	0.7509(95)	52.72[−]	—	0.579
		4	8	0.69[−]	9.70×10^4[−]	—	0.471
		5	8	0.439(35)	11.61[−]	—	0.196
		6	8	0.560(72)	4.20[−]	—	0.207
3	0	1	8	0.5726(43)	1.1827(37)	19.79[−]	2.648
		2	8	0[−]	0.7657(43)	1.72[−]	0.398
		3	8	0[−]	0.7620(77)	31.46[−]	0.473
		4	8	0[−]	0.744(14)	8(36)	0.273
		5	8	0[−]	0.660(18)	15.26[−]	0.267
		6	8	0[−]	1.523(20)	65.36[−]	0.08
3	1	1	8	0.8319(20)	1.368(13)	21.11[−]	0.585
		2	8	0.27[−]	0.95[−]	1.116(55)	0.230
		3	8	0[−]	0.82[−]	31.46[−]	0.462
		4	8	0.430(26)	0.766(30)	6.657(33)	0.153
		5	8	0[−]	0.460(32)	15.26[−]	0.190
		6	8	0[−]	0.663(47)	65.36[−]	0.179

Table 5.26: Fitted mass parameters for two and three-exponential fully correlated factorising fits to a 4×4 matrix of correlators using a basis of operators $\{\mathcal{O}_0^{A_1^{++}}, \mathcal{O}_1^{A_1^{++}}, \mathcal{O}_2^{A_1^{++}}, \mathcal{O}_3^{A_1^{++}}\}$ with $|\vec{p}| = 0$ and $|\vec{p}| = 1$ for varying t_{min} with t_{max} fixed at $t = 8$. Where errors are quoted as [−] this indicates that the gradient in that direction of parameter space could not be determined, *i.e.* that the parameter is essentially free.

These results are presented in Tables 5.27 and 5.28 for the $t_{\max} = 7$ and $t_{\max} = 8$ factorising fits for both $N_{\exp} = 2$ and $N_{\exp} = 3$ with $|\vec{p}| = 0$ and $|\vec{p}| = 1$. Whilst the stability of the fits does seem marginally improved there are still a large number of poorly determined masses. We note, however, that there appears to be good consistency for the $N_{\exp} = 2, |\vec{p}| = 0$ and $|\vec{p}| = 1$ fits with both $t_{\max} = 7$ and $t_{\max} = 8$ if $t_{\min}$ is chosen small.

$N_{\exp}$	$\lvert\vec{p}\rvert$	$t_{\min}$	$t_{\max}$	am_0	am_1	am_2	χ^2/d.o.f.
2	0	1	7	0.7963(46)	1.742(23)	—	1.077
		2	7	0.657(14)	1.90(10)	—	0.437
		3	7	0±0.2	0.818(29)	—	0.146
		4	7	0±0.2	0.847(87)	—	0.074
		5	7	0.324(50)	34.61[−]	—	0.196
2	1	1	7	0.8407(42)	1.478(22)	—	0.769
		2	7	0.756(29)	0.991(50)	—	0.215
		3	7	0(0)	0.837(24)	—	0.229
		4	7	0.232(98)	2.15[−]	—	0.093
		5	7	0.317(86)	34.61[−]	—	0.099
3	0	1	7	0±0.31	0.8677(65)	1.743(24)	0.465
		2	7	0±0.17	0.760(22)	1.75(11)	0.092
3	1	1	7	0.8442(43)	1.162(65)	2.44(22)	0.245
		2	7	0(0)	0.887(12)	1.064(77)	0.120
		3	7	0(0)	0.882(25)	10.303(25)	0.143

Table 5.27: Fitted mass parameters for two and three-exponential uncorrelated factorising fits to a 4×4 matrix of correlators using a basis of operators $\{\mathcal{O}_0^{A_1^{++}}, \mathcal{O}_1^{A_1^{++}}, \mathcal{O}_2^{A_1^{++}}, \mathcal{O}_3^{A_1^{++}}\}$ with $|\vec{p}| = 0$ and $|\vec{p}| = 1$ for varying $t_{\min}$ with $t_{\max}$ fixed at $t = 7$. Where errors are quoted as [−] this indicates that the gradient in that direction of parameter space could not be determined, *i.e.* that the parameter is essentially free.

With this in mind we choose, using the 4×4 factorising fully-correlated fits, to study the $t_{\max}$ dependence of the fitted masses for small values of $t_{\min}$. The $t_{\max}$ dependence of the fit results are presented for $t_{\min} = 1$ and $t_{\min} = 2$ in Figs. 5.32 and 5.33 respectively, as well as Tables 5.29 and 5.30. For the $t_{\min} = 1$ results we see excellent consistency for the groundstates between the $N_{\exp} = 2$ (both $|\vec{p}| = 0$ and 1) and the $N_{\exp} = 3$ $|\vec{p}| = 1$ fits. The $N_{\exp} = 2$, $|\vec{p}| = 1$ fits for $t_{\min} = 2$ are also consistent with the $t_{\min} = 1$ fits, although there is a significant difference between the groundstate determinations between the $t_{\min} = 2$ $N_{\exp} = 2$ $|\vec{p}| = 0$ and $|\vec{p}| = 1$ fits.

5.9.1 Basis Experimentation

In order to best explore the apparent inconsistencies between groundstate masses observed above we performed factorising fits to the matrices of correlators formed using the bases $\{\mathcal{O}_0^{A_1^{++}}, \mathcal{O}_1^{A_1^{++}}, \mathcal{O}_2^{A_1^{++}}\}$, $\{\mathcal{O}_0^{A_1^{++}}, \mathcal{O}_1^{A_1^{++}}, \mathcal{O}_3^{A_1^{++}}\}$, $\{\mathcal{O}_0^{A_1^{++}}, \mathcal{O}_2^{A_1^{++}}, \mathcal{O}_3^{A_1^{++}}\}$ and $\{\mathcal{O}_1^{A_1^{++}}, \mathcal{O}_2^{A_1^{++}}, \mathcal{O}_3^{A_1^{++}}\}$. The latter was found to provide the most stable fits, as it was

N_{exp}	$\lvert\vec{p}\rvert$	t_{min}	t_{max}	am_0	am_1	am_2	χ^2/d.o.f.
2	0	1	8	0.7938(46)	1.741(23)	—	1.164
		2	8	0.638(14)	1.900(95)	—	0.580
		3	8	0±0.13	0.811(24)	—	0.143
		4	8	0±0.16	0.826(61)	—	0.080
2	1	1	8	0.8405(42)	1.478(22)	—	0.691
		2	8	0.756(28)	0.994(50)	—	0.207
		3	8	0(0)	0.812(21)	—	0.254
		4	8	0(0)	1.012(85)	—	0.120
		5	8	0(0)	0.441(63)	—	0.129
		6	8	0(0)	0.74(18)	—	0.105
3	0	1	8	0±0.17	0.8581(62)	1.749(23)	0.436
		2	8	0.638(15)	1.90(13)	68.64[−]	0.590
3	1	1	8	0.8440(43)	1.163(57)	2.44(17)	0.235
		2	8	0.757(25)	0.994(46)	68.85[−]	0.211
		3	8	0.43(11)	0.865(44)	10.77[−]	0.182
		4	8	0(0)	1.012(85)	13.70[−]	0.205
		5	8	0.434(59)	20.68[−]	502[−]	0.149
		6	8	0(0)	0.74(18)	416[−]	0.111

Table 5.28: Fitted mass parameters for two and three-exponential uncorrelated factorising fits to a 4×4 matrix of correlators using a basis of operators $\{\mathcal{O}_0^{A_1^{++}}, \mathcal{O}_1^{A_1^{++}}, \mathcal{O}_2^{A_1^{++}}, \mathcal{O}_3^{A_1^{++}}\}$ with $|\vec{p}| = 0$ and $|\vec{p}| = 1$ for varying t_{min} with t_{max} fixed at $t = 8$. Where errors are quoted as [−] this indicates that the gradient in that direction of parameter space could not be determined, *i.e.* that the parameter is essentially free.

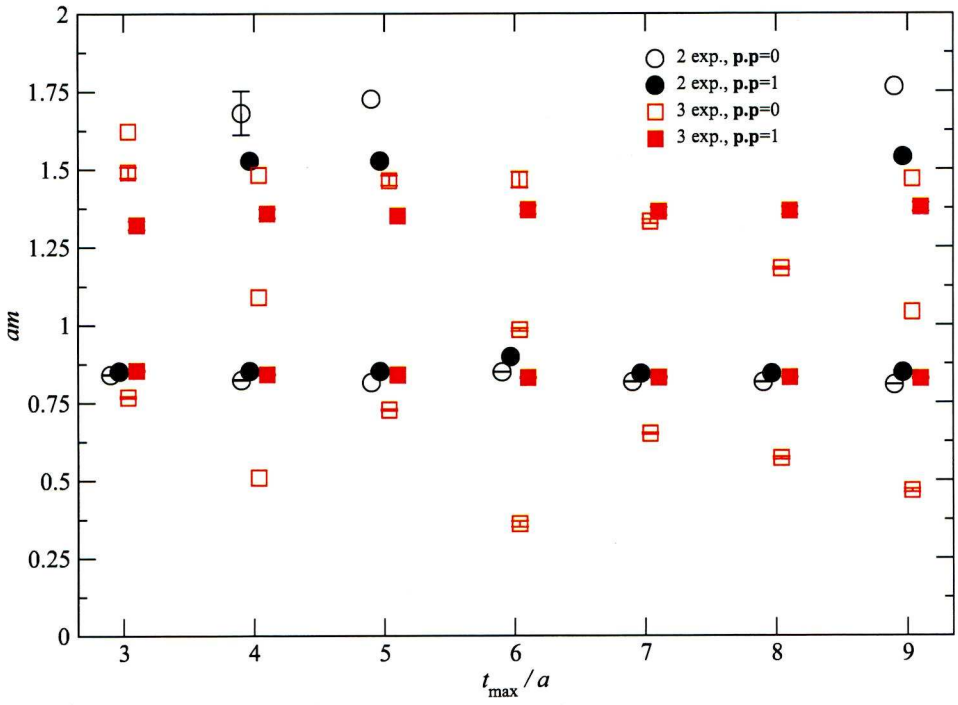

Figure 5.32: Results from factorising fits applied to the 4×4 basis of scalar glueball operators $\{\mathcal{O}_0^{A_1^{++}}, \mathcal{O}_1^{A_1^{++}}, \mathcal{O}_2^{A_1^{++}}, \mathcal{O}_3^{A_1^{++}}\}$ measured on the fine lattices. Both two and three-exponential fits are presented for the $|\vec{p}| = 0$ and $|\vec{p}| = 1$ correlators, with $t_{\text{min}} = 1$ and t_{max} allowed to vary. The two-exponential results are presented as circles, three-exponential results as squares, $|\vec{p}| = 0$ results open shapes and $|\vec{p}| = 1$ results filled shapes.

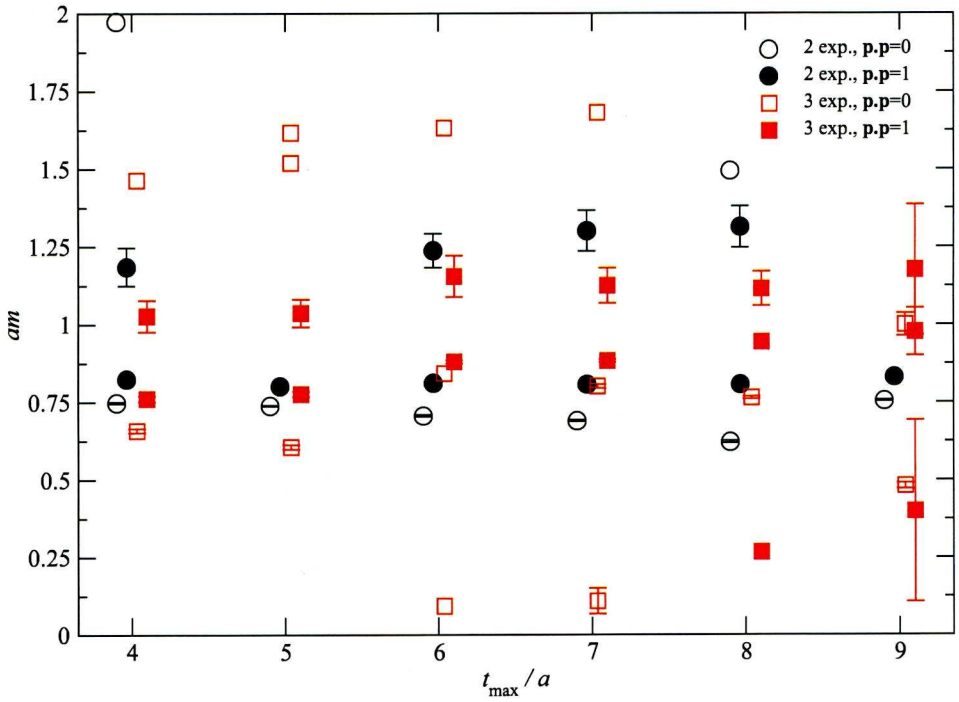

Figure 5.33: Results from factorising fits applied to the 4×4 basis of scalar glueball operators $\{\mathcal{O}_0^{A_1^{++}}, \mathcal{O}_1^{A_1^{++}}, \mathcal{O}_2^{A_1^{++}}, \mathcal{O}_3^{A_1^{++}}\}$ measured on the fine lattices. Both two and three-exponential fits are presented for the $|\vec{p}| = 0$ and $|\vec{p}| = 1$ correlators, with $t_{\text{min}} = 2$ and t_{max} allowed to vary. The two-exponential results are presented as circles, three-exponential results as squares, $|\vec{p}| = 0$ results open shapes and $|\vec{p}| = 1$ results filled shapes.

N_{exp}	$\lvert\vec{p}\rvert$	t_{min}	t_{max}	am_0	am_1	am_2	χ^2/d.o.f.
		1	3	0.84139(97)	19.84[−]	—	7.233
		1	4	0.8237(17)	1.681(71)	—	5.098
		1	5	0.82[−]	1.73[−]	—	5.255
2	0	1	6	0.84937(76)	692[−]	—	31.42
		1	7	0.81705(91)	19.16[−]	—	6.747
		1	8	0.81657(92)	19.06[−]	—	6.515
		1	9	0.80834(81)	1.77[−]	—	5.182
		1	3	0.8521(15)	19.56[−]	—	8.185
		1	4	0.8528(13)	1.53[−]	—	3.604
		1	5	0.8517(12)	1.53[−]	—	2.885
2	1	1	6	0.8985(14)	692[−]	—	37.12
		1	7	0.8446(13)	19.00[−]	—	3.838
		1	8	0.8446(13)	18.93[−]	—	3.368
		1	9	0.8480(11)	1.54[−]	—	1.933
		1	3	0.7695(31)	1.493(17)	1.62[−]	1.549
		1	4	0.51[−]	1.09[−]	1.48[−]	1.450
		1	5	0.7284(22)	1.466(16)	20.29[−]	1.987
3	0	1	6	0.3622(96)	0.9863(45)	1.468(26)	1.126
		1	7	0.6518(30)	1.3337(66)	16.65[−]	2.495
		1	8	0.5726(43)	1.1827(37)	19.78[−]	2.648
		1	9	0.4679(51)	1.04[−]	1.47[−]	1.866
		1	3	0.8551(21)	1.322(14)	2.67(12)	0.144
		1	4	0.8420(21)	1.360(14)	2.73(20)	0.431
		1	5	0.84[−]	1.352(13)	22.23[−]	0.378
3	1	1	6	0.8317(22)	1.371(14)	2.57[−]	0.542
		1	7	0.8319(20)	1.366(13)	18.17[−]	0.642
		1	8	0.8319(20)	1.368(13)	21.12[−]	0.585
		1	9	0.8274(23)	1.379(14)	2.40[−]	0.540

Table 5.29: Fitted mass parameters for two and three-exponential fully correlated factorising fits to a 4×4 matrix of correlators using a basis of operators $\{\mathcal{O}_0^{A_1^{++}}, \mathcal{O}_1^{A_1^{++}}, \mathcal{O}_2^{A_1^{++}}, \mathcal{O}_3^{A_1^{++}}\}$ with $|\vec{p}| = 0$ and $|\vec{p}| = 1$ for varying t_{max} with t_{min} fixed at $t = 1$. Where errors are quoted as [−] this indicates that the gradient in that direction of parameter space could not be determined, *i.e.* that the parameter is essentially free.

N_{exp}	$\lvert\vec{p}\rvert$	t_{min}	t_{max}	am_0	am_1	am_2	χ^2/d.o.f.
2	0	2	4	0.7486(27)	1.97[−]	—	0.779
		2	5	0.7392(17)	16.67[−]	—	1.037
		2	6	0.7070(27)	2.13[−]	—	1.513
		2	7	0.6906(29)	2.04[−]	—	1.868
		2	8	0.6224(33)	1.49[−]	—	2.194
		2	9	0.7551(18)	26.91[−]	—	4.305
2	1	2	4	0.8249(40)	1.186(61)	—	0.2483
		2	5	0.8021(35)	16.42[−]	—	0.558
		2	6	0.8122(38)	1.238(55)	—	0.416
		2	7	0.8074(38)	1.302(66)	—	0.522
		2	8	0.8076(37)	1.314(67)	—	0.475
		2	9	0.8319(36)	26.91[−]	—	1.977
3	0	2	4	0.6601(69)	1.46[−]	9.37[−]	0.149
		2	5	0.6072(70)	1.52[−]	1.62[−]	0.195
		2	6	0[−]	0.84[−]	1.63[−]	0.205
		2	7	0.110(41)	0.8025(66)	1.68[−]	0.396
		2	8	0[−]	0.7657(43)	1.71[−]	0.398
		2	9	0.4824(96)	1.001(36)	1.651(23)	1.368
3	1	2	4	0.7627(96)	1.029(51)	10.19[−]	0.03
		2	5	0.7772(85)	1.038(44)	10.94[−]	0.102
		2	6	0[−]	0.8811(53)	1.156(66)	0.176
		2	7	0[−]	0.8845(48)	1.127(57)	0.156
		2	8	0.27[−]	0.95[−]	1.116(55)	0.230
		2	9	0.40(29)	0.978(77)	1.18(21)	0.254

Table 5.30: Fitted mass parameters for two and three-exponential fully correlated factorising fits to a 4×4 matrix of correlators using a basis of operators $\{\mathcal{O}_0^{A_1^{++}}, \mathcal{O}_1^{A_1^{++}}, \mathcal{O}_2^{A_1^{++}}, \mathcal{O}_3^{A_1^{++}}\}$ with $|\vec{p}| = 0$ and $|\vec{p}| = 1$ for varying t_{max} with t_{min} fixed at $t = 2$. Where errors are quoted as [−] this indicates that the gradient in that direction of parameter space could not be determined, *i.e.* that the parameter is essentially free.

with the variational projections.

We find the best fits are obtained for $t_{\text{min}} = 1$ and $5 \leq t_{\text{max}} \leq 9$ with $N_{\text{exp}} = 3$ for the $|\vec{p}| = 1$ correlators. The results for the $N_{\text{exp}} = 2$ and $N_{\text{exp}} = 3$ fits to the $|\vec{p}| = 0$ and $|\vec{p}| = 1$ correlator are presented in Table 5.31 where t_{min} is fixed at 1 and t_{max} varies. We find that for $t_{\text{min}} > 1$ the majority of fits are unstable, favouring either degenerate masses (*i.e.* effectively single exponential fits) or finding undetermined errors for the fit parameters.

N_{exp}	$\lvert\vec{p}\rvert$	t_{min}	t_{max}	am_0	am_1	am_2	χ^2/d.o.f.
2	0	1	4	0.86[–]	0.86[–]	—	99.73
		1	5	0.85[–]	0.85[–]	—	81.47
		1	6	0.85[–]	0.85[–]	—	70.40
		1	7	0.80884(98)	1.80[–]	—	12.96
		1	8	0.8084(10)	1.80[–]	—	12.76
		1	9	0.8088(10)	1.80[–]	—	11.85
2	1	1	4	0.8526(13)	1.55[–]	—	8.021
		1	5	0.8515(13)	1.55[–]	—	6.337
		1	6	0.8489(13)	1.56[–]	—	5.747
		1	7	0.8478(13)	1.56[–]	—	5.269
		1	8	0.8478(13)	1.56[–]	—	4.628
		1	9	0.8478(13)	1.56[–]	—	4.150
3	0	1	4	0.86[–]	0.86[–]	0.86[–]	106
		1	5	0.86[–]	0.86[–]	0.86[–]	85.6
		1	6	0.86[–]	0.86[–]	0.86[–]	73.3
		1	7	0.85[–]	0.85[–]	0.85[–]	63.8
		1	8	0.85[–]	0.85[–]	0.85[–]	57.0
		1	9	0.85[–]	0.85[–]	0.85[–]	50.8
3	1	1	4	0.90[–]	0.90[–]	0.90[–]	137
		1	5	0.8379(22)	1.355(14)	2.65[–]	0.805
		1	6	0.8296(24)	1.364(14)	2.47[–]	1.169
		1	7	0.8248(24)	1.371(14)	2.30[–]	1.361
		1	8	0.8248(24)	1.373(14)	2.30[–]	1.227
		1	9	0.8247(25)	1.371(14)	2.30[–]	1.146

Table 5.31: Fitted mass parameters for two and three-exponential fully correlated factorising fits to a 3×3 matrix of correlators using a basis of operators $\{\mathcal{O}_1^{A_1^{++}}, \mathcal{O}_2^{A_1^{++}}, \mathcal{O}_3^{A_1^{++}}\}$ with $|\vec{p}| = 0$ and $|\vec{p}| = 1$ for varying t_{max} with t_{min} fixed at $t = 1$. Where errors are quoted as [–] this indicates that the gradient in that direction of parameter space could not be determined, *i.e.* that the parameter is essentially free.

5.9.2 Overall Average

In order to obtain our final determination of the scalar glueball mass on fine lattices we will again carry out the averaging procedure as used by the Particle Data Group [132]. We use the determinations from the following sources:

- the masses obtained from the weighted average of the variational effective masses computed on the following three projections: the 2/1 projection on the 4×4 basis of $\{\mathcal{O}_0^{A_1^{++}}, \mathcal{O}_1^{A_1^{++}}, \mathcal{O}_2^{A_1^{++}}, \mathcal{O}_3^{A_1^{++}}\}$ with $|\vec{p}| = 0$, computed between $t = 3 - 5$; the 2/0 projection on the 4×4 basis of $\{\mathcal{O}_0^{A_1^{++}}, \mathcal{O}_1^{A_1^{++}}, \mathcal{O}_2^{A_1^{++}}, \mathcal{O}_3^{A_1^{++}}\}$ with $|\vec{p}| = 1$ computed between $t = 3 - 5$; and the 2/1 projections on the 3×3 basis of $\{\mathcal{O}_0'^{A_1^{++}}, \mathcal{O}_1'^{A_1^{++}}, \mathcal{O}_2'^{A_1^{++}}\}$ with $|\vec{p}| = 0$ computed between $t = 3 - 5$. The difference between these three estimates is used to estimate the systematic error.

- the masses extracted from the variational eigenvalues for the 3×3 matrix of correlators formed using the basis of operators $\{\mathcal{O}_1^{A_1^{++}}, \mathcal{O}_2^{A_1^{++}}, \mathcal{O}_3^{A_1^{++}}\}$. The values for the 2/1 and 3/0 projections with both $|\vec{p}| = 0$ and $|\vec{p}| = 1$ will be used, and the difference will be used to estimate the systematic error.

- the masses extracted from the variational eigenvalues for the 3×3 matrix of correlators formed using the basis of operators $\{\mathcal{O}_0'^{A_1^{++}}, \mathcal{O}_1'^{A_1^{++}}, \mathcal{O}_2'^{A_1^{++}}\}$. The values for the 2/1 and 3/0 projections will be used ($|\vec{p}| = 0$ only) and the difference used to estimate the systematic error.

- the factorising fit results to a 4×4 matrix of correlators formed using the basis of operators $\{\mathcal{O}_0^{A_1^{++}}, \mathcal{O}_1^{A_1^{++}}, \mathcal{O}_2^{A_1^{++}}, \mathcal{O}_3^{A_1^{++}}\}$. The values for the three-exponential fits to the $|\vec{p}| = 1$ correlators will be used with $t_{\mathrm{min}} = 1$, $t_{\mathrm{max}} = 4 - 8$ and the two-exponential fits to the $|\vec{p}| = 1$ correlators with $t_{\mathrm{min}} = 2$ and $t_{\mathrm{max}} = 5 - 8$. The differences will be used to estimate the systematic error.

- the factorising fit results to a 3×3 matrix of correlators formed using the basis of operators $\{\mathcal{O}_1^{A_1^{++}}, \mathcal{O}_2^{A_1^{++}}, \mathcal{O}_3^{A_1^{++}}\}$. The two and three-exponential fits to the $|\vec{p}| = 1$ correlators will be used, with $t_{\mathrm{min}} = 1$, $t_{\mathrm{max}} = 5 - 8$, the difference being used to estimate the systematic error.

These sources are presented in Tables 5.32, 5.33, 5.34, 5.35 and 5.36 and give a final value for the scalar glueball groundstate mass on the fine lattices of

$$am = 0.8332(59) \tag{5.14}$$

where the error is both statistical and systematic. This is shown in Fig. 5.34 along with the five sources.

The same procedure was carried out for the first-excited state where estimates were available, the sources shown in Fig. 5.35, obtaining a final value of

$$am^* = 1.368(17) \ . \tag{5.15}$$

Again the error on the final estimate is less than 1% but again we feel our reasons for choosing particular results over others are addressed in the text.

Source	Central Value	Statistical Error
2/1 proj., 4×4 basis $\{\mathcal{O}_0^{A_1^{++}}, \mathcal{O}_1^{A_1^{++}}, \mathcal{O}_2^{A_1^{++}}, \mathcal{O}_3^{A_1^{++}}\}$, $\lvert\vec{p}\rvert = 0 : t = 3-5$	0.641	0.057
2/0 proj., 4×4 basis $\{\mathcal{O}_0^{A_1^{++}}, \mathcal{O}_1^{A_1^{++}}, \mathcal{O}_2^{A_1^{++}}, \mathcal{O}_3^{A_1^{++}}\}$, $\lvert\vec{p}\rvert = 1 : t = 3-5$	0.692	0.066
2/1 proj., 3×3 basis $\{\mathcal{O}_0^{\prime A_1^{++}}, \mathcal{O}_1^{\prime A_1^{++}}, \mathcal{O}_2^{\prime A_1^{++}}\}$, $\lvert\vec{p}\rvert = 0 : t = 3-5$	0.690	0.081
Average±stat.±sys.		0.674±0.068±0.020

Table 5.32: The weighted averages of the variational effective masses for various bases of operators, as described, along with a determination of the the overall statistical and systematic errors.

Source	Central Value	Statistical Error
$\lvert\vec{p}\rvert = 0$ Eig. (2/1)	0.854	0.022
$\lvert\vec{p}\rvert = 0$ Eig. (3/0)	0.862	0.021
$\lvert\vec{p}\rvert = 1$ Eig. (2/1)	0.874	0.021
$\lvert\vec{p}\rvert = 1$ Eig. (3/0)	0.927	0.022
Average±stat.±sys.		0.879±0.022±0.019

Table 5.33: Masses extracted from the eigenvalues obtained from the solutions of the GEVP (4.17) for the 3×3 matrices of correlators formed using the bases of operators $\{\mathcal{O}_1^{A_1^{++}}, \mathcal{O}_2^{A_1^{++}}, \mathcal{O}_3^{A_1^{++}}\}$ for $\lvert\vec{p}\rvert = 0$ and $\lvert\vec{p}\rvert = 1$ respectively, at $t/t_0 = 2/1$ and $t/t_0 = 3/0$

Source	Central Value	Statistical Error
$\lvert\vec{p}\rvert = 0$ Eig. (2/1)	0.838	0.025
$\lvert\vec{p}\rvert = 0$ Eig. (3/0)	0.834	0.023
Average±stat.±sys.		0.836±0.024±0.003

Table 5.34: Masses extracted from the eigenvalues obtained from the solutions of the GEVP (4.17) for the 3×3 matrices of correlators formed using the bases of operators $\{\mathcal{O}_0^{\prime A_1^{++}}, \mathcal{O}_1^{\prime A_1^{++}}, \mathcal{O}_2^{\prime A_1^{++}}\}$ for $\lvert\vec{p}\rvert = 0$ and respectively, at $t/t_0 = 2/1$ and $t/t_0 = 3/0$

Source	Central Value	Statistical Error
$\lvert\vec{p}\rvert = 1$, $t_{\text{min}} = 1$, $t_{\text{max}} = 4$ ($N_{\text{exp}} = 3$)	0.8420	0.0021
$\lvert\vec{p}\rvert = 1$, $t_{\text{min}} = 1$, $t_{\text{max}} = 6$ ($N_{\text{exp}} = 3$)	0.8317	0.0022
$\lvert\vec{p}\rvert = 1$, $t_{\text{min}} = 1$, $t_{\text{max}} = 7$ ($N_{\text{exp}} = 3$)	0.8319	0.0020
$\lvert\vec{p}\rvert = 1$, $t_{\text{min}} = 1$, $t_{\text{max}} = 8$ ($N_{\text{exp}} = 3$)	0.8319	0.0020
$\lvert\vec{p}\rvert = 1$, $t_{\text{min}} = 2$, $t_{\text{max}} = 5$ ($N_{\text{exp}} = 2$)	0.8021	0.0035
$\lvert\vec{p}\rvert = 1$, $t_{\text{min}} = 2$, $t_{\text{max}} = 6$ ($N_{\text{exp}} = 2$)	0.8122	0.0038
$\lvert\vec{p}\rvert = 1$, $t_{\text{min}} = 2$, $t_{\text{max}} = 7$ ($N_{\text{exp}} = 2$)	0.8074	0.0038
$\lvert\vec{p}\rvert = 1$, $t_{\text{min}} = 2$, $t_{\text{max}} = 8$ ($N_{\text{exp}} = 2$)	0.8076	0.0037
Average±stat.±sys.		0.8208±0.0029±0.0057

Table 5.35: Factorising fit results for the $N_{\text{exp}} = 2$ and $N_{\text{exp}} = 3$ fits to the 4×4 matrices of correlators formed using the basis of operators $\{\mathcal{O}_0^{A_1^{++}}, \mathcal{O}_1^{A_1^{++}}, \mathcal{O}_2^{A_1^{++}}, \mathcal{O}_3^{A_1^{++}}\}$ for $\lvert\vec{p}\rvert = 1$.

Source	Central Value	Statistical Error
$\vert\vec{p}\vert = 1$, $t_{\max} = 5$ ($N_{\exp} = 2$)	0.8515	0.0013
$\vert\vec{p}\vert = 1$, $t_{\max} = 6$ ($N_{\exp} = 2$)	0.8489	0.0013
$\vert\vec{p}\vert = 1$, $t_{\max} = 7$ ($N_{\exp} = 2$)	0.8478	0.0013
$\vert\vec{p}\vert = 1$, $t_{\max} = 8$ ($N_{\exp} = 2$)	0.8478	0.0013
$\vert\vec{p}\vert = 1$, $t_{\max} = 5$ ($N_{\exp} = 3$)	0.8379	0.0022
$\vert\vec{p}\vert = 1$, $t_{\max} = 6$ ($N_{\exp} = 3$)	0.8296	0.0024
$\vert\vec{p}\vert = 1$, $t_{\max} = 7$ ($N_{\exp} = 3$)	0.8248	0.0024
$\vert\vec{p}\vert = 1$, $t_{\max} = 8$ ($N_{\exp} = 3$)	0.8248	0.0024
Average±stat.±sys.		0.839±0.0018±0.0043

Table 5.36: Factorising fit results for the $N_{\exp} = 2$ and $N_{\exp} = 3$ fits to the 3×3 matrix of correlators formed using the basis of operators $\{\mathcal{O}_1^{A_1^{++}}, \mathcal{O}_2^{A_1^{++}}, \mathcal{O}_3^{A_1^{++}}\}$ for $|\vec{p}| = 1$.

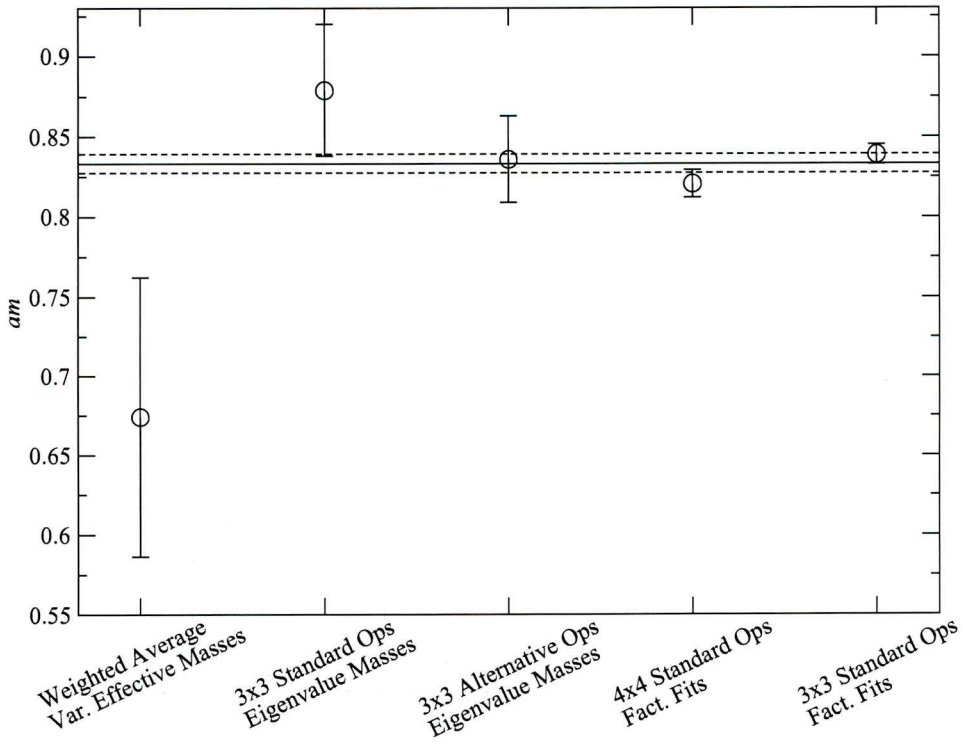

Figure 5.34: The overall average for the scalar glueball groundstate mass on the fine lattices, computed as described in the text.

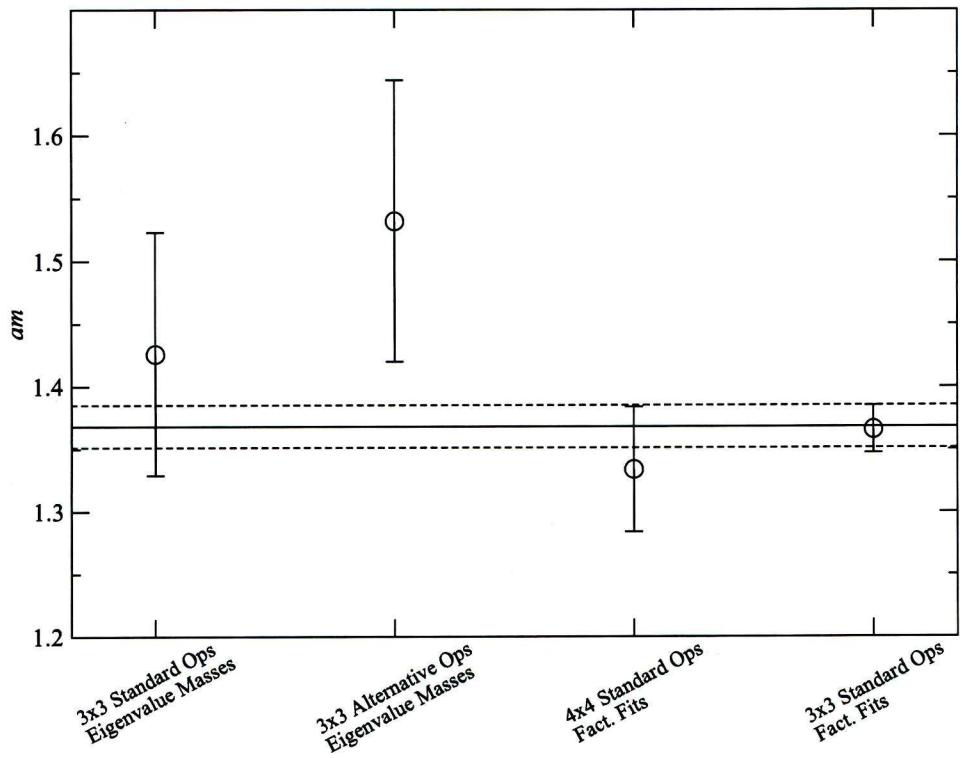

Figure 5.35: The overall average for the scalar glueball first excited state mass on the fine lattices, computed as described in the text.

5.10 Glueball Decay

Having observed signals in our fits which appear close to the 2π threshold we can no longer be confident about our mass estimate from these fits. In order to restore this confidence we must check the strength of the mixing between the glueball and $\pi\pi$ operators. Early attempts to study the mixing directly have been made [147], although these were performed at pion masses such that $2m_\pi$ was just below m_G. One would naïvely expect that glueball decay would be flavour blind, decaying into $\pi\pi$, $K\bar{K}$ and $\eta\eta$ final states with equal widths. Of course since we are now observing the state (or states) to which the gluonic operators couple most strongly then mixing effects are likely to violate flavour blindness — if the 'glueball' mixes strongly with a mainly $u\bar{u}+d\bar{d}$ state then the $\pi\pi$ decay channel is preferred over the OZI suppressed $K\bar{K}$ channel, and vice versa if the coupling is strongest to an $s\bar{s}$ state.

One can in principle study decay matrix elements directly on the lattice following the procedure of Lellouch and Lüscher [148] however this requires us to have very accurate determinations of our matrix elements on a number of different lattices and as such is a difficult technique to apply even for states less subject to noise than the glueball.

We choose to follow the method of [149][8] and form the mixing matrix

$$M_{ab}(t) = \begin{pmatrix} M_{GG}(t) & M_{\pi G}(t) \\ M_{G\pi}(t) & M_{\pi\pi}(t) \end{pmatrix} = \begin{pmatrix} \langle \mathcal{O}_i^{A_1^{++}}(0)\mathcal{O}_i^{A_1^{++}}(t)\rangle & \langle C_\pi(0)\mathcal{O}_i^{A_1^{++}}(t)\rangle \\ \langle \mathcal{O}_i^{A_1^{++}}(t)C_\pi(0)\rangle & \langle C_\pi(t)C_\pi(t)\rangle \end{pmatrix} \quad (5.16)$$

where $\mathcal{O}_i^{A_1^{++}}(0)$ and $\mathcal{O}_i^{A_1^{++}}(t)$ are the $|\vec{p}| = 0$ scalar glueball operators defined in (5.1) at timeslices 0 and t respectively, and $C_\pi(0)$ and $C_\pi(t)$ are the single pion correlators on timeslice 0 and t respectively. The $C_\pi(0)$ correlator allows us to study a $\pi\pi$ state localised in time, and due to our methods for computing the connected correlator we are restricted to using $C_\pi(0)$ which reduces our statistics for the 2π operators by a factor of 64.

We can attempt to perform a multichannel fit to this matrix using the fitting form

$$f_{ab}(t) = \begin{pmatrix} G(t) + \eta_\pi^2\Pi_2(t) & \eta_G G(t) + \eta_\pi\Pi_2(t) \\ \eta_G G(t) + \eta_\pi\Pi_2(t) & \Pi_2(t) + \eta_G^2 G(t) \end{pmatrix} \quad (5.17)$$

where η_G and η_π are measures of the mixing between the 2π operators and a glueball state and the glueball operators and a 2π state, respectively. Choosing the following forms for $G(t)$ and $\Pi_2(t)$

$$\begin{aligned} G(t) &= A_G e^{-m_G t} \\ \Pi_2(t) &= A_{2\pi} e^{-2m_\pi t} \end{aligned} \quad (5.18)$$

[8] With additional advice from one of the authors [150]

we can attempt to proceed in three ways. Firstly and ideally we would wish to use the fit to fix all parameters, including the glueball and pion masses, however due to the reduction in statistics for the pion our matrix is rather noisy and this method was found to fail with poor χ^2/dof and large uncertainties on all parameters. Secondly we could fix the glueball and pion masses to those obtained from previous determinations, although this was also found to give poor fits. We expect that this may be due to the fact that when a glueball decays into two pions the decay products are free to move off with a total spatial momentum of zero, such that each pion may have equal and opposite momenta of modulus $\left|\vec{k}_n\right| = \frac{2\pi n}{L}$, where L is the spatial extent of the lattice. Because of this we are unlikely to observe a pion mass of exactly $2m_\pi$, nor of $E_1 = 2\sqrt{m_\pi^2 + \left|\vec{k}_1\right|}$ etc., but rather some effective pion state at some intermediate energy. In principle one could attempt to fit to a tower of momentum states, although since each requires its own amplitude this is likely to overparameterise the fit rapidly.

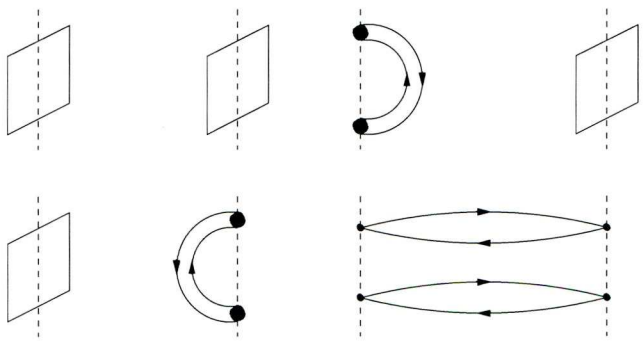

Figure 5.36: Schematic of the glueball-$\pi\pi$ mixing matrix defined in (5.16), where we have shown the element $M_{G\pi}$ as we would ideally compute it.

One can form the ratio [149, 150]

$$x_{G\pi}(t) = \frac{M_{G\pi}(t)}{\sqrt{M_{GG}(t) M_{\pi\pi}(t)}} \tag{5.19}$$

where the $M_{ab}(t)$ are the elements of (5.16) on timeslice t. This gives us a measure of the off-diagonal mixing matrix elements, normalised by the diagonal entries.

We have computed these ratios for the coarse and fine lattices, using the glueball operator with three levels of Teper blocking — *i.e.* $\mathcal{O}_3^{A_1^{++}}$ — which we found shows similar behaviour to the lower blocking levels but with less noise. We used the pion correlators with both local source and local sink, and fuzzed source and fuzzed sink. Our results are presented in Fig. 5.37.

For the coarse ratios we see that at small t they appear consistent with zero, turning negative for $t \sim 5$, although here the error is rather large. We do note however that the fine mixing ratio seems to show a similar downturn for $t \sim 3 - 4$. Whilst these ratios

give only a guide to the mixing of the glueball operators and a $\pi\pi$ the smallness of $x_{G\pi}$ for small times indicates that provided we choose t_{min} small enough we should obtain a good overlap with the stable glueball, and conversely that by choosing t_{min} large we may obtain a significant overlap with the $\pi\pi$ state. This indeed appears to have been the case.

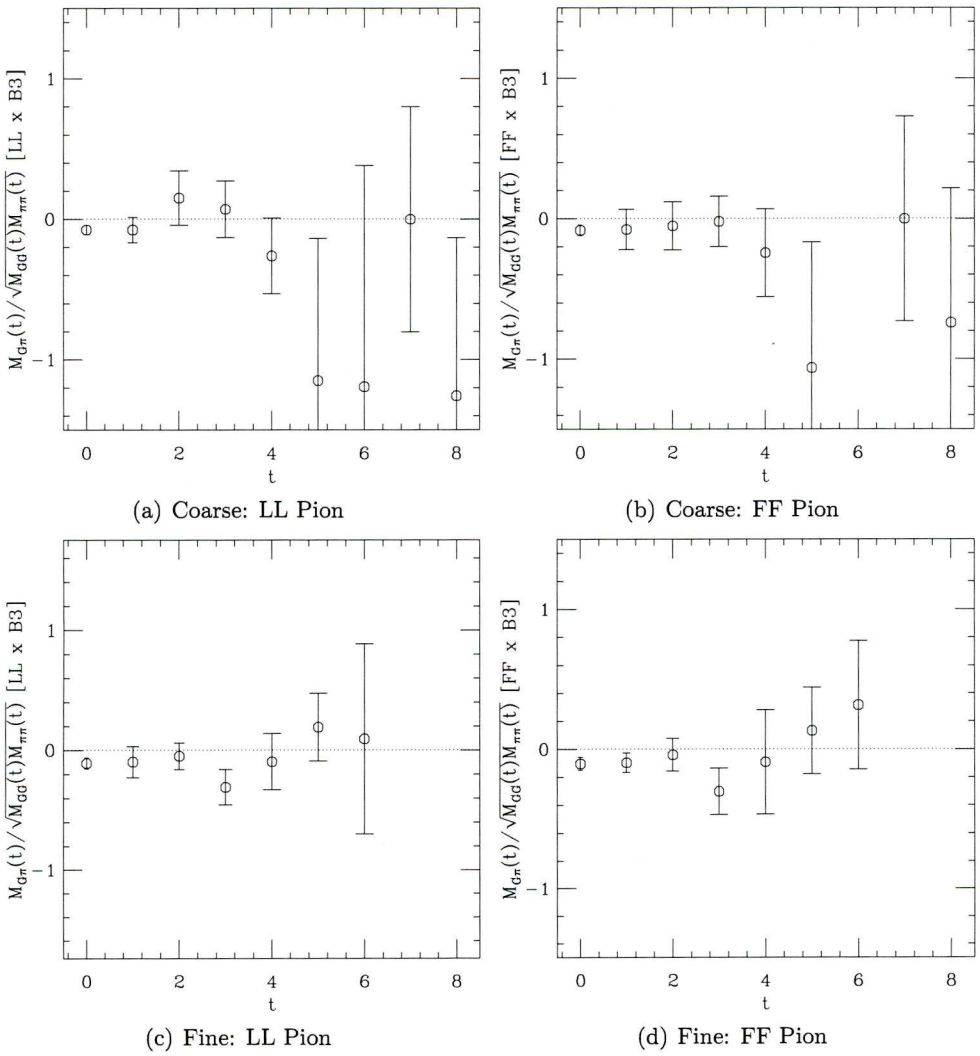

(a) Coarse: LL Pion

(b) Coarse: FF Pion

(c) Fine: LL Pion

(d) Fine: FF Pion

Figure 5.37: The measure of glueball-$\pi\pi$ mixing defined in (5.19) for, clockwise from top-left: the local-local (LL) pion correlators with the three-times Teper blocked glueball operators on the coarse lattices; the fuzzed-fuzzed (FF) pion correlators with the three-times Teper blocked glueball operators on the coarse lattices; the fuzzed-fuzzed (FF) pion correlators with the three-times Teper blocked glueball operators on the fine lattices; and the local-local (LL) pion correlators with the three-times Teper blocked glueball operators on the fine lattices.

5.11 Comparison of Results

Having extracted estimates of the ground and first excited scalar glueball masses for both the coarse and fine lattices we must now attempt to compare these to previous determinations, both from the lattice and experiment. To this end we first remove the explicit scale dependence from our results by converting am to $r_0 m$ — this allows for a direct comparison with previous lattice estimates without introducing the additional systematic error of choosing a physical value for r_0.

Result	am	$r_0 m$
Coarse – Ground	1.0468(75)	3.991(36)
Fine – Ground	0.8332(59)	4.215(38)
Coarse – Excited	1.875(87)	7.15(35)
Fine – Excited	1.368(17)	6.92(10)

Table 5.37: Scalar glueball masses (ground and first-excited states) from the coarse and fine lattices converted into units of the Sommer parameter r_0.

In Fig. 5.38 we present our results along with those from a recent UKQCD study of scalar glueballs using staggered fermions [146], a UKQCD study using $\mathcal{O}(a)$ non-perturbatively improved Wilson fermions ($N_f = 2$) [117] and the continuum limit result from a quenched anisotropic study of the glueball spectrum [106]. We perform a continuum extrapolation using the form

$$\phi_0(a) = r_0 m_G + c_4 \frac{a^4}{r_0^4} \tag{5.20}$$

where $r_0 m_G$ and c_4 are the parameters to be determined. In [106] this was found to work well for all glueball states except for the A_1^{++} — this was thought to be due to strong lattice spacing dependence caused by proximity to the the non-physical phase transition in the Wilson fundamental-adjoint plane, however the alternative form used in [106] has four free parameters which we cannot hope to constrain with two data points. Of course it is still somewhat ambitious to attempt a continuum extrapolation using (5.20) with two data points only and we emphasise that this has been performed as a guide only. We do note, however, that there is excellent consistency between our continuum value and that of Morningstar and Peardon, obtaining $r_0 m_G = 4.32$ compared to their value of $r_0 m_G = 4.21(11)(4)$. Our value corresponds to a physical value of 1.83 GeV.

Whether or not such an extrapolation is valid, given the limited data points, our masses do seem to show rather weak dependence on a — certainly weaker than that observed in [117] and of a similar strength to that observed in [106].

In Fig. 5.39 we present our results against the pion mass, shown with the same comparisons from the literature as in Fig. 5.38. One might tentatively claim that the

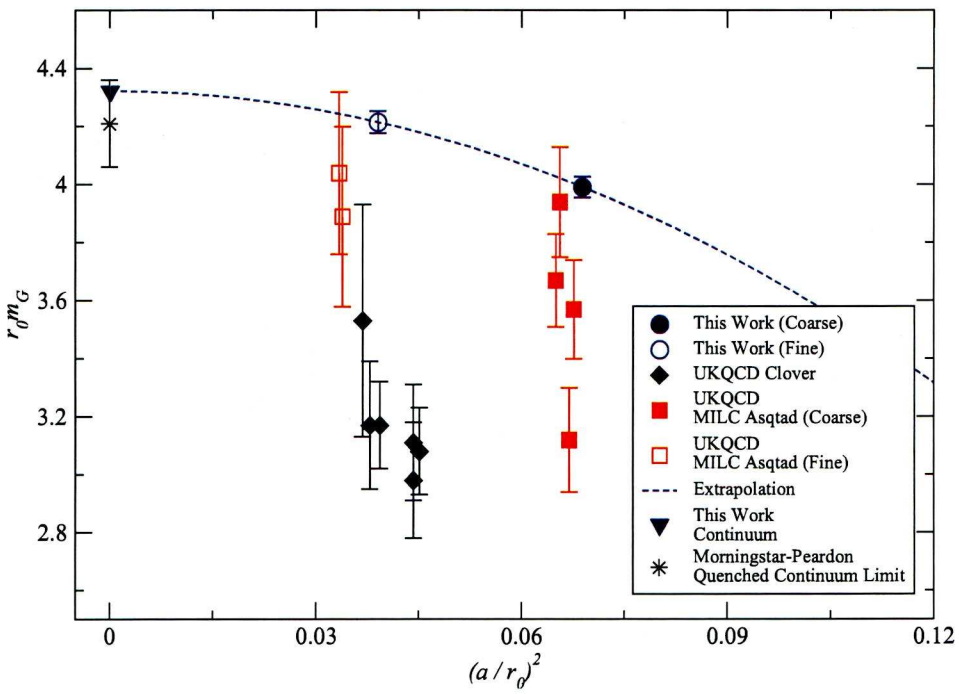

Figure 5.38: Our measurements of the scalar glueball mass shown with previous quenched (Morningstar and Peardon [106]) and dynamical (UKQCD on MILC Asqtad [146] and UKQCD Clover [117]) determinations with the continuum extrapolation performed as in [106].

glueball mass increases as one decreases the pion mass, hinting at some underlying mixing dynamics. However the UKQCD measurements on the coarse MILC asqtad ensembles are rather spread out and if, as is suspected, the $\mathcal{O}(a)$ improved Wilson measurements are supressed by the phase structure of the action used then they should probably be discounted and there remains very little trend to study.

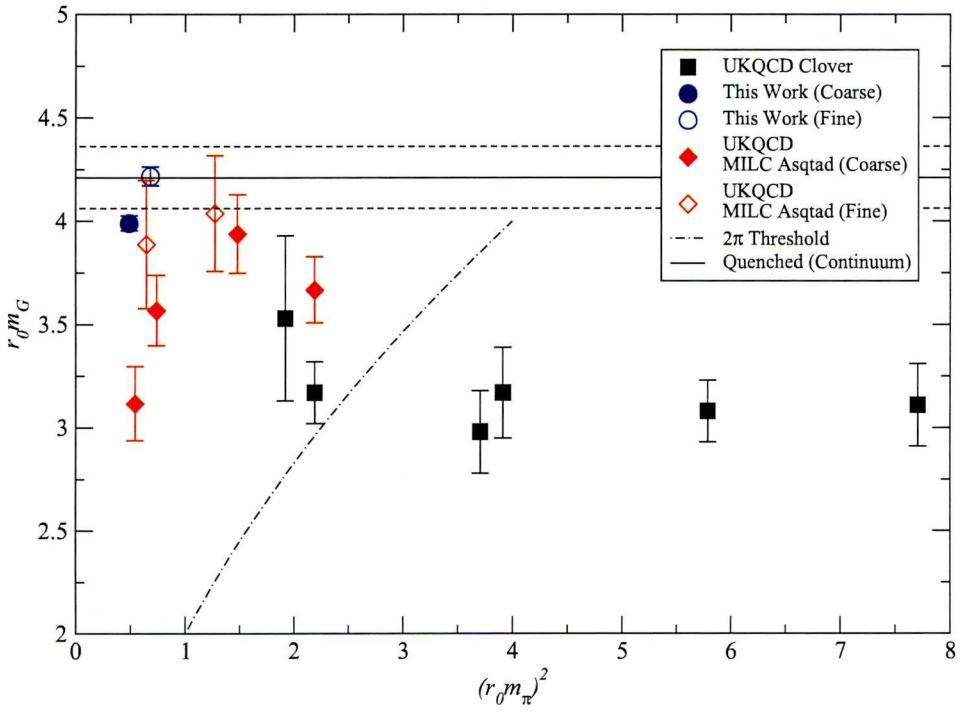

Figure 5.39: Our measurements of the scalar glueball mass shown with previous dynamical (UKQCD on MILC Asqtad [146] and UKQCD Clover [117]) determinations. The $\pi\pi$ threshold is shown (dash-dotted line) for convenience.

5.12 Pseudoscalar Glueball

As discussed the pseudoscalar glueball has received little attention in recent lattice QCD studies of the glueball spectrum. Since the pseudoscalar glueball is expected to mix with the η and η' pseudoscalar mesons it could be very sensitive to the effects of dynamical quarks and thereby show large unquenching effects. In order to shed light on this we have measured the pseudoscalar glueball on our lattices

We first present the measurements on the coarse lattices, followed by those on the fine lattices. We have attempted to study the effective masses for the pseudoscalar glueball correlators but the signal is lost to noise too quickly for us to be able to resolve a plateau. We therefore start by looking at the eigenvalue spectrum.

5.12.1 Coarse Measurements

Eigenvalue Masses

In Table 5.38 we present the eigenvalues from the solution of the GEVP (4.17) at the specified t/t_0, as well as the masses extracted from them, for a 3×3 matrix of correlators formed using the basis of operators $\{\mathcal{O}_0^{A_1^{-+}}, \mathcal{O}_1^{A_1^{-+}}, \mathcal{O}_2^{A_1^{-+}}\}$. The groundstate masses are also plotted in Fig. 5.40. We see that the projections are reasonably stable for the 1/0, 2/1 and 2/0 projections.

t/t_0	λ^0	$am(\lambda^0)$	λ^1	$am(\lambda^1)$	λ^2	$am(\lambda^2)$
1/0	0.1535(38)	1.863(41)	0.0769(30)	2.565(61)	0.0268(22)	3.62(11)
2/1	0.216(59)	1.53(22)	0.178(28)	1.73(21)	0.115(31)	2.16(38)
3/2	0.40(74)	0.93(41)	0.04(16)	3.2(1.4)	−0.24(58)	0(0.76)
2/0	0.0329(25)	1.706(57)	0.0088(21)	2.37(13)	0.0052(18)	2.63(62)
3/0	0.0067(19)	1.667(86)	−0.0003(20)	0(1)	−0.0034(18)	0(0.40)
3/1	0.106(27)	1.12(19)	0.074(24)	1.30(99)	−0.037(55)	0(0.42)

Table 5.38: Eigenvalues obtained from the solution of the GEVP at the specified t/t_0, and masses extracted using (4.19). 3×3 basis of $\{\mathcal{O}_0^{A_1^{-+}}, \mathcal{O}_1^{A_1^{-+}}, \mathcal{O}_2^{A_1^{-+}}\}$ operators with $|\vec{p}| = 0$ measured on the coarse lattices.

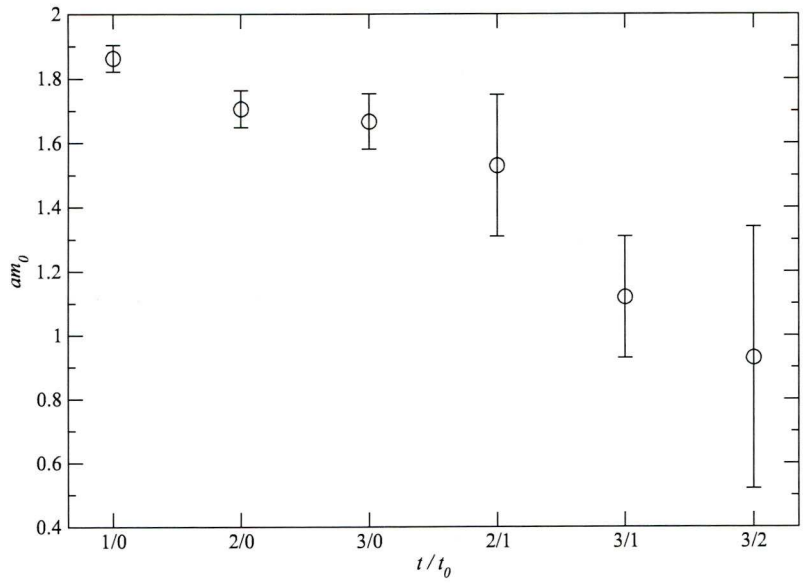

Figure 5.40: The masses extracted from the groundstate variational eigenvalues using (4.19) for different t/t_0 projections performed on a 3×3 matrix of correlators formed from the basis of pseudoscalar glueball operators $\{\mathcal{O}_0^{A_1^{-+}}, \mathcal{O}_1^{A_1^{-+}}, \mathcal{O}_2^{A_1^{-+}}\}$ measured with $|\vec{p}| = 0$ on the coarse lattices.

Factorising Fits

We have performed 3×3 factorising fits to the matrix of correlators formed using the basis of pseudoscalar glueball operators $\{\mathcal{O}_0^{A_1^{-+}}, \mathcal{O}_1^{A_1^{-+}}, \mathcal{O}_2^{A_1^{-+}}\}$ with $|\vec{p}| = 0$. We initially performed two-exponential fully-correlated fits to these correlators and whilst we obtained good values for χ^2/d.o.f. we found the second mass to be unreliable. It was observed that the most reliable fits were those with $t_{\text{min}} = 1$ and $3 \leq t_{\text{max}} \leq 5$ and we therefore choose to study the $t_{\text{min}} = 1$ uncorrelated fits. The fit parameters are presented in Table 5.39 and we see that there is very little dependence on t_{max}. We also include the three-exponential fully correlated fits in Table 5.39.

N_{exp}	t_{min}	t_{max}	am_0	am_1	am_2	χ^2/d.o.f.
2	1	3	1.715(21)	2.120(57)	—	0.466
	1	4	1.703(22)	2.114(55)	—	0.440
	1	5	1.702(21)	2.115(55)	—	0.412
	1	6	1.703(21)	2.116(55)	—	0.442
	1	7	1.703(21)	2.116(55)	—	0.430
	1	8	1.703(21)	2.116(55)	—	0.407
3	1	4	1.549(57)	1.951(47)	2.94(52)	0.275
	1	5	1.563(61)	1.959(66)	2.88(44)	0.275
	1	6	1.562(70)	1.958(72)	2.89(53)	0.394
	1	7	1.56[−]	1.96[−]	2.90(40)	0.387
	1	8	1.556(70)	1.952(68)	2.95(41)	0.398

Table 5.39: Fitted mass parameters for two and three-exponential factorising uncorrelated and correlated (respectively) fits to a 3×3 matrix of correlators using a basis of operators $\{\mathcal{O}_0^{A_1^{-+}}, \mathcal{O}_1^{A_1^{-+}}, \mathcal{O}_2^{A_1^{-+}}\}$ measured on the coarse lattices with $|\vec{p}| = 0$ for varying t_{max} with t_{min} fixed at $t = 1$. Where errors are quoted as [−] this indicates that the gradient in that direction of parameter space could not be determined, *i.e.* that the parameter is essentially free.

We note there is a systematic difference between the groundstate mass obtained using two-exponential fits and that obtained using three-exponential fits. Since the three-exponential fits seem to be stable with reasonable χ^2/d.o.f. we choose to use these masses. We note that the groundstate masses remain the same, within errors, as those in Table 5.39 if we use fully-correlated fits to the $N_{\text{exp}} = 2$ data and uncorrelated fits to the $N_{\text{exp}} = 3$ data. In order to obtain reasonable fits we have found it necessary to use $t_{\text{min}} = 1$.

Overall Average

In order to apply our averaging procedure to the coarse pseudoscalar glueball results we include the eigenvalue masses and the factorising fit results. We include the 2/0 projection in the average for the eigenvalue masses which due to the positivity violations for the action used is not a sound thing to do, however we point out the large statistical

and systematic errors on the overall determination for the eigenvalue masses means that the final determination is dominated by the factorising fit results. The estimations of the systematic errors for the eigenvalue masses and the factorising fit masses are presented in Tables 5.40 and 5.41 respectively. After applying our averaging procedure we obtain a mass of

$$am_G^{A_1^{-+}} = 1.560(67) \tag{5.21}$$

for the groundstate (see Fig. 5.41) and

$$am_G^{A_1^{-+}*} = 1.956(65) \tag{5.22}$$

for the first excited state.

Source	Central Value	Statistical Error
2/1 Eig.	1.538	0.22
2/0 Eig.	1.706	0.057
Average±stat.±sys.		1.618±0.139±0.124

Table 5.40: Masses extracted from the eigenvalues obtained from the solutions of the GEVP (4.17) for the 3×3 matrix of correlators formed using the basis of operators $\{\mathcal{O}_0^{A_1^{-+}}, \mathcal{O}_2^{A_1^{-+}}, \mathcal{O}_3^{A_1^{-+}}\}$ measured on the coarse lattices for $|\vec{p}| = 0$ at $t/t_0 = 2/1$ and $t/t_0 = 2/0$.

Source	Central Value	Statistical Error
$N_{\text{exp}} = 3$ Fit, $t_{\text{min}} = 1$, $t_{\text{max}} = 4$	1.549	0.057
$N_{\text{exp}} = 3$ Fit, $t_{\text{min}} = 1$, $t_{\text{max}} = 5$	1.563	0.061
$N_{\text{exp}} = 3$ Fit, $t_{\text{min}} = 1$, $t_{\text{max}} = 6$	1.562	0.070
$N_{\text{exp}} = 3$ Fit, $t_{\text{min}} = 1$, $t_{\text{max}} = 8$	1.556	0.070
Average±stat.±sys.		1.556±0.065±0.004

Table 5.41: Determination of the overall systematic error on the factorising fit results for the 3×3 matrix of correlators formed using the basis of operators $\{\mathcal{O}_0^{A_1^{-+}}, \mathcal{O}_2^{A_1^{-+}}, \mathcal{O}_3^{A_1^{-+}}\}$ measured on the coarse lattices for $|\vec{p}| = 0$.

5.12.2 Fine Measurements

We now present our measurements of the pseudoscalar glueball on the fine lattices.

Eigenvalue Masses

In Table 5.42 and Fig. 5.42 we present the eigenvalues from the solution of the GEVP (4.17) at the specified t/t_0, and the masses extracted therefrom, for the 3×3 matrix of correlators formed from the basis of pseudoscalar operators $\{\mathcal{O}_0^{A_1^{-+}}, \mathcal{O}_1^{A_1^{-+}}, \mathcal{O}_2^{A_1^{-+}}\}$ measured with $|\vec{p}| = 0$ on the fine lattices. We note that, as with the coarse projections, the 2/0, 2/1 and 3/0 projections appear to give the best results.

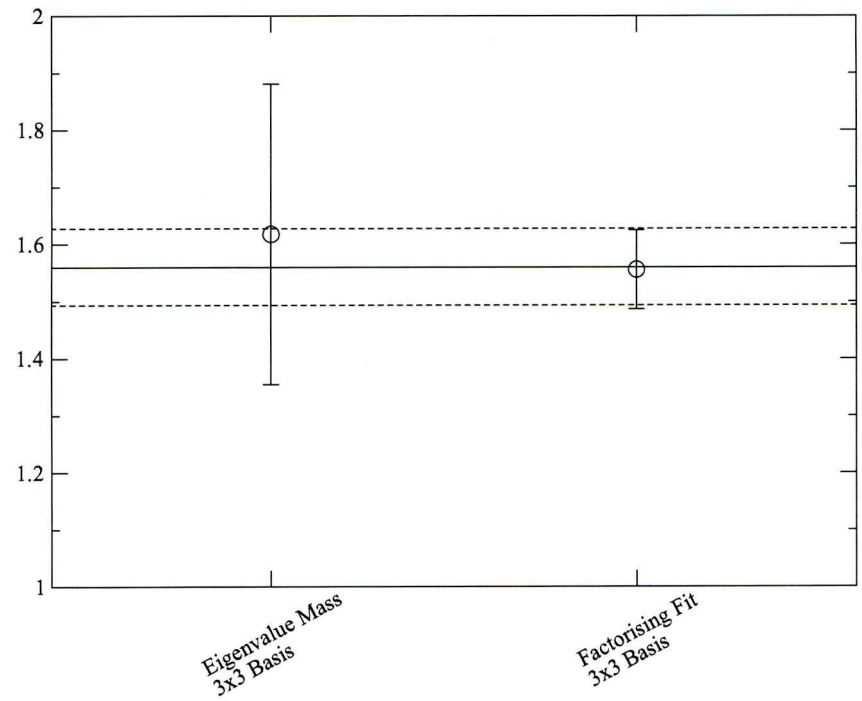

Figure 5.41: The overall average for the pseudoscalar glueball groundstate mass on the coarse lattices, computed as described in the text.

t/t_0	λ^0	$am(\lambda^0)$	λ^1	$am(\lambda^1)$	λ^2	$am(\lambda^2)$
1/0	0.2395(56)	1.429(32)	0.1348(39)	2.004(46)	0.0344(29)	3.37(10)
2/1	0.290(11)	1.236(43)	0.129(31)	2.05(19)	−0.023(56)	0(2)
3/2	0.6(1.6)	0.54(40)	0.27(23)	1.3(1.1)	−2(32)	0(1)
2/0	0.0663(30)	1.357(34)	0.0184(26)	1.99(81)	0.0017(30)	3(1)
3/0	0.0207(40)	1.293(76)	0.0037(27)	2(1)	−0.0053(27)	0(0.8)
3/1	0.114(20)	1.09(10)	0.004(21)	2.74(90)	−0.19(06)	0(0.46)

Table 5.42: Eigenvalues obtained from the solution of the GEVP at the specified t/t_0, and masses extracted using (4.19). 3×3 basis of $\{\mathcal{O}_0^{A_1^{-+}}, \mathcal{O}_1^{A_1^{-+}}, \mathcal{O}_2^{A_1^{-+}}\}$ operators with $|\vec{p}| = 0$ measured on the fine lattices.

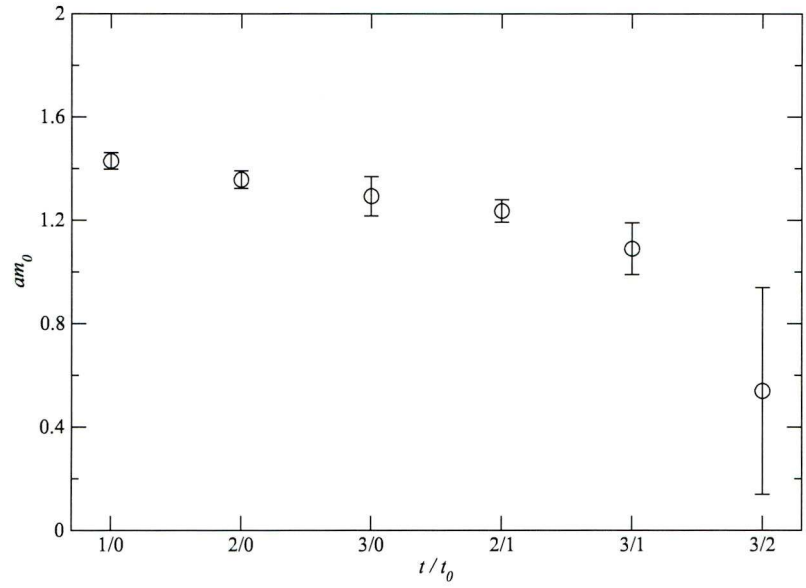

Figure 5.42: The masses extracted from the groundstate variational eigenvalues using (4.19) for different t/t_0 projections performed on a 3×3 matrix of correlators formed from the basis of pseudoscalar glueball operators $\{\mathcal{O}_0^{A_1^{-+}}, \mathcal{O}_1^{A_1^{-+}}, \mathcal{O}_2^{A_1^{-+}}\}$ measured with $|\vec{p}| = 0$ on the fine lattices.

Factorising Fit Results

We have performed 3×3 factorising fits to the matrix of correlators formed using the basis of pseudoscalar glueball operators $\{\mathcal{O}_0^{A_1^{-+}}, \mathcal{O}_1^{A_1^{-+}}, \mathcal{O}_2^{A_1^{-+}}\}$ with $|\vec{p}| = 0$. We have again performed uncorrelated two-exponential fits and fully correlated three-exponential fits, as dictated by the results. These have been performed with t_{min} fixed at $t = 1$ for varying t_{max}. We note, in contrast to the coarse factorising fit results (Table 5.41), that the groundstate masses for both the two-exponential and three-exponential fits are consistent.

Overall Average

In order to apply our averaging procedure to the fine pseudoscalar glueball results we include the eigenvalue masses and the factorising fit results. In order to determine the systematic errors on the eigenvalue masses we include those results from the 2/0 and 3/0 projections, again noting that the overall average is dominated by the factorising fit results. Our estimations of the systematic errors for the eigenvalue masses and the factorising fit masses are presented in Tables 5.44 and 5.45 respectively. After applying our averaging procedure we obtain a mass of

$$am_G^{A_1^{-+}} = 1.265(17) \tag{5.23}$$

N_{exp}	t_{min}	t_{max}	am_0	am_1	am_2	χ^2/d.o.f.
2	1	3	1.289(16)	2.084(50)	—	0.769
	1	4	1.277(16)	2.067(49)	—	0.679
	1	5	1.263(17)	2.061(48)	—	0.804
	1	6	1.262(17)	2.059(48)	—	0.708
	1	7	1.261(17)	2.059(48)	—	0.658
	1	8	1.261(17)	2.059(48)	—	0.578
3	1	4	1.275(12)	1.842(52)	2.68[−]	0.696
	1	5	1.261(12)	1.903(47)	2.60[−]	0.847
	1	6	1.260(20)	1.904(48)	2.61[−]	0.731
	1	7	1.260(12)	1.909(48)	2.63[−]	0.677
	1	8	1.261(12)	1.909(48)	2.63[−]	0.594

Table 5.43: Fitted mass parameters for two and three-exponential factorising uncorrelated and correlated (respectively) fits to a 3×3 matrix of correlators using a basis of operators $\{\mathcal{O}_0^{A_1^{-+}}, \mathcal{O}_1^{A_1^{-+}}, \mathcal{O}_2^{A_1^{-+}}\}$ measured on the fine lattices with $|\vec{p}| = 0$ for varying t_{max} with t_{min} fixed at $t = 1$. Where errors are quoted as $[-]$ this indicates that the gradient in that direction of parameter space could not be determined, *i.e.* that the parameter is essentially free.

for the groundstate (see Fig. 5.43) and

$$am_G^{A_1^{-+}*} = 1.984(77) \tag{5.24}$$

for the first excited state.

Source	Central Value	Statistical Error
2/1 Eig.	1.236	0.043
2/0 Eig.	1.357	0.034
3/0 Eig.	1.293	0.076
Average±stat.±sys.		1.295±0.051±0.043

Table 5.44: Masses extracted from the eigenvalues obtained from the solutions of the GEVP (4.17) for the 3×3 matrix of correlators formed using the basis of operators $\{\mathcal{O}_0^{A_1^{-+}}, \mathcal{O}_2^{A_1^{-+}}, \mathcal{O}_3^{A_1^{-+}}\}$ measured on the fine lattices for $|\vec{p}| = 0$ at $t/t_0 = 2/1$, $t/t_0 = 2/0$ and $t/t_0 = 3/0$.

5.12.3 Comparison of Results

We remove the explicit dependence on a from our results by converting into units of the Sommer parameter r_0, the results presented in Table 5.46. These are presented in Fig. 5.44 along with a continuum extrapolation, performed using (5.20) — again, since we have too few data points to constrain the fit this is presented as a guide only. We obtain a continuum value of $r_0 m_G^{0^{-+}} = 6.61$ ($M_G \sim 2.79$ GeV) which again compares well with the quenched determination of $r_0 m_G^{0^{-+}} = 6.33(7)(6)$ ($M_G \sim 2590(40)(120)$ MeV) [106]. We note that the dependence on a^2 is rather strong, that is to say it is at least as strong as that observed for the scalar glueball in Fig. 5.38.

Source	Central Value	Statistical Error
$N_{\mathrm{exp}} = 2$ Fit, $t_{\mathrm{min}} = 1$, $t_{\mathrm{max}} = 4$	1.277	0.016
$N_{\mathrm{exp}} = 2$ Fit, $t_{\mathrm{min}} = 1$, $t_{\mathrm{max}} = 5$	1.263	0.017
$N_{\mathrm{exp}} = 2$ Fit, $t_{\mathrm{min}} = 1$, $t_{\mathrm{max}} = 6$	1.262	0.017
$N_{\mathrm{exp}} = 2$ Fit, $t_{\mathrm{min}} = 1$, $t_{\mathrm{max}} = 7$	1.261	0.017
$N_{\mathrm{exp}} = 2$ Fit, $t_{\mathrm{min}} = 1$, $t_{\mathrm{max}} = 8$	1.261	0.017
$N_{\mathrm{exp}} = 3$ Fit, $t_{\mathrm{min}} = 1$, $t_{\mathrm{max}} = 4$	1.275	0.012
$N_{\mathrm{exp}} = 3$ Fit, $t_{\mathrm{min}} = 1$, $t_{\mathrm{max}} = 5$	1.261	0.012
$N_{\mathrm{exp}} = 3$ Fit, $t_{\mathrm{min}} = 1$, $t_{\mathrm{max}} = 6$	1.260	0.020
$N_{\mathrm{exp}} = 3$ Fit, $t_{\mathrm{min}} = 1$, $t_{\mathrm{max}} = 7$	1.260	0.012
$N_{\mathrm{exp}} = 3$ Fit, $t_{\mathrm{min}} = 1$, $t_{\mathrm{max}} = 8$	1.261	0.012
Average$\pm$stat.$\pm$sys.		1.264$\pm$0.015$\pm$0.002

Table 5.45: Determination of the overall systematic error on the factorising fit results for the 3×3 matrix of correlators formed using the basis of operators $\{\mathcal{O}_0^{A_1^{-+}}, \mathcal{O}_2^{A_1^{-+}}, \mathcal{O}_3^{A_1^{-+}}\}$ measured on the coarse lattices for $|\vec{p}| = 0$.

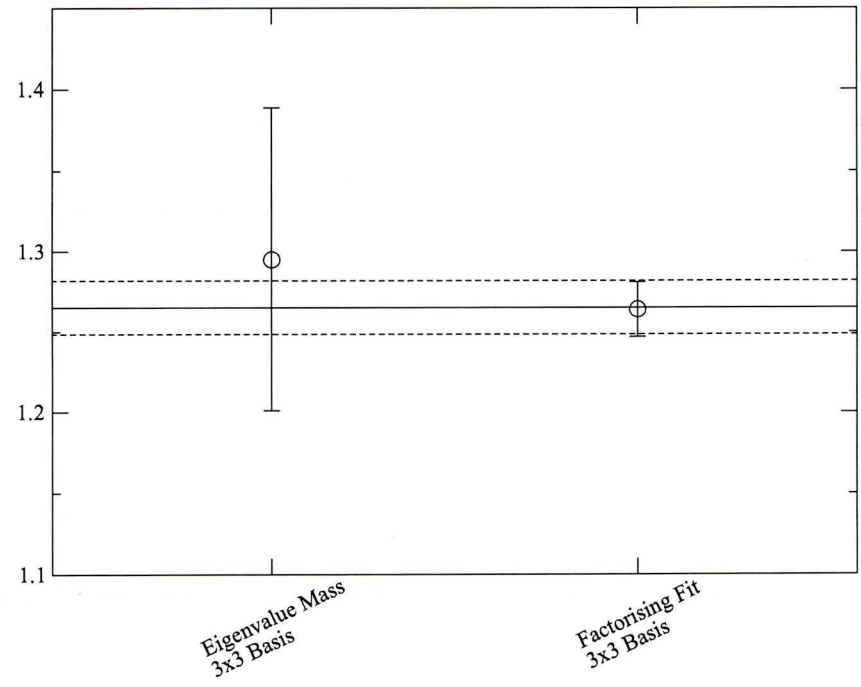

Figure 5.43: The overall average for the pseudoscalar glueball groundstate mass on the fine lattices, computed as described in the text.

With so few data points the extrapolation is simply a guide but we view this as an area for future study.

Result	am	$r_0 m$
Coarse – Ground	1.560(67)	5.95(12)
Fine – Ground	1.265(17)	6.399(99)
Coarse – Excited	1.956(65)	7.46(26)
Fine – Excited	1.984(77)	10.04(41)

Table 5.46: Pseudoscalar glueball masses (ground and first-excited states) from the coarse and fine lattices converted into units of the Sommer parameter r_0.

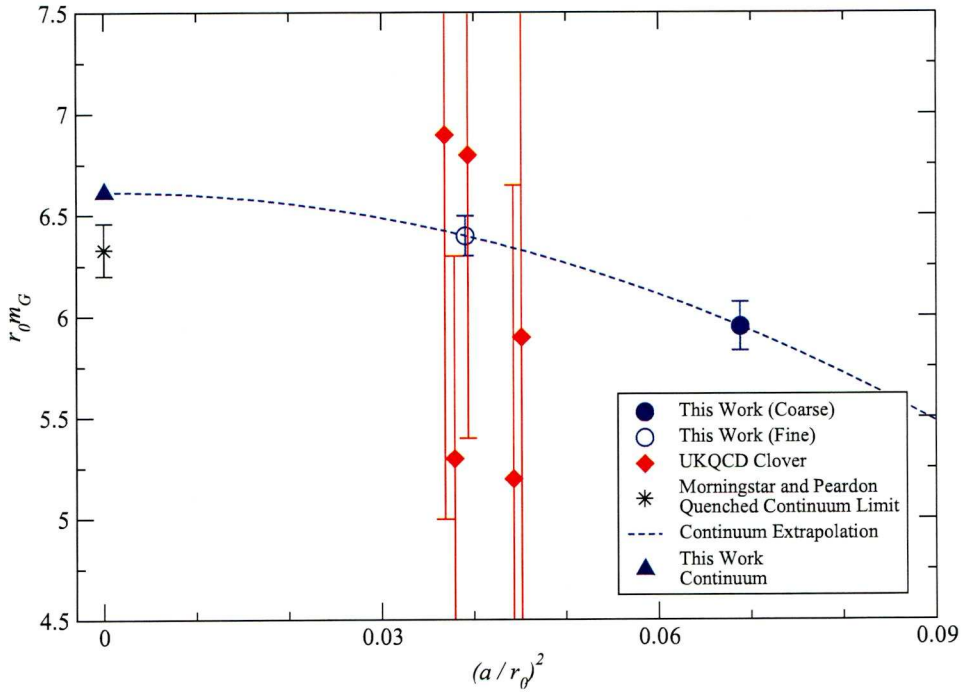

Figure 5.44: Our measurements of the pseudoscalar glueball mass shown with previous quenched (Morningstar and Peardon [106]) and dynamical (UKQCD Clover [117]) determinations with the continuum extrapolation performed as in [106].

In Fig. 5.45 we present our results against the same UKQCD dynamical $\mathcal{O}(a)$ non-perturbatively improved Wilson fermion results, this time against $r_0^2 m_\pi^2$ in order to show possible unquenching effects. Since the clover results for the pseudoscalar glueball are not affected by the phase-transition we can take them into account here and therefore conclude that unquenching effects for the pseudoscalar glueball are very weak indeed.

5.13 Tensor Glueball

Due to a machine failure we only have measurements for the tensor glueball on our coarse lattices. We have measured both the $\mathcal{O}^{E_1^{++}}$ and $\mathcal{O}'^{E_1^{++}}$ operators at $|\vec{p}| = 0$ on

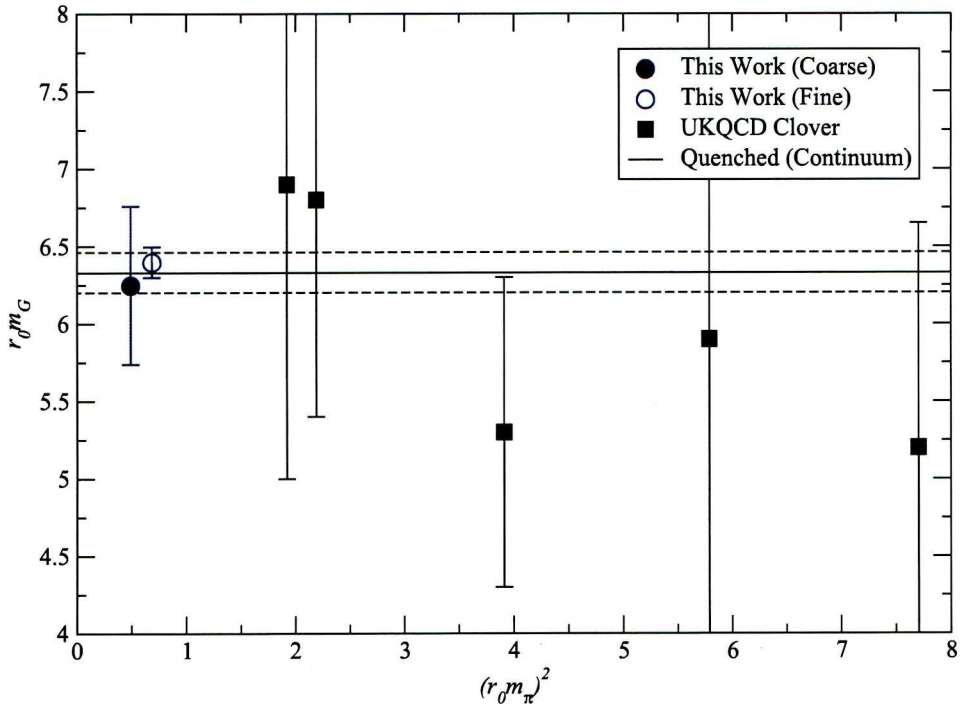

Figure 5.45: Our measurements of the pseudoscalar glueball mass shown with those determinations from the dynamical UKQCD Clover [117] measurements. The quenched continuum limit from [106] is shown for comparison.

the coarse lattices and present our analysis here.

5.13.1 Eigenvalue Masses

In Tables 5.47 and 5.48 we present the eigenvalues obtained from the solutions of the GEVP (4.17) on 4×4 matrices of correlators formed using bases of the $\mathcal{O}^{E_1^{++}}$ and $\mathcal{O}'^{E_1^{++}}$ operators at the specified t/t_0, and the masses extracted therefrom. These masses are compared in Fig. 5.46 and show excellent agreement

t/t_0	λ^0	$am(\lambda^0)$	λ^1	$am(\lambda^1)$	λ^2	$am(\lambda^2)$
1/0	0.1801(44)	1.714(39)	0.081(3)	2.51(6)	0.041(2)	3.19(8)
2/1	0.216(30)	1.53(11)	0.16(3)	1.86(17)	0.06(5)	2.8(1.2)
2/0	0.0371(21)	1.647(42)	0.018(2)	2.00(10)	0(0)	3.55(95)
3/0	0.0113(25)	1.495(73)	0.009(2)	1.59(40)	0(0)	0(1)
3/1	0.100(40)	1.15(15)	0.09(2)	1.23(29)	0(0)	0(1)

Table 5.47: Eigenvalues obtained from the solution of the GEVP at the specified t/t_0, and masses extracted using (4.19). 4×4 basis of $\{\mathcal{O}_0^{E_1^{++}}, \mathcal{O}_1^{E_1^{++}}, \mathcal{O}_2^{E_1^{++}}, \mathcal{O}_2^{E_1^{++}}\}$ operators with $|\vec{p}| = 0$ measured on the fine lattices. We do not show λ^3 or $am(\lambda^3)$ as in all cases they are poorly determined.

t/t_0	λ^0	$am(\lambda^0)$	λ^1	$am(\lambda^1)$	λ^2	$am(\lambda^2)$
1/0	0.1796(46)	1.717(39)	0.0923(29)	2.38(6)	0.041(2)	3.19(8)
2/1	0.256(30)	1.36(12)	0.222(42)	1.50(27)	0.077(39)	3(1)
2/0	0.0378(22)	1.638(43)	0.0086(24)	2.38(14)	0.004(2)	2.77(86)
3/0	0.0145(22)	1.411(73)	0.0025(20)	2.00(18)	0(0)	0(1)
3/1	0.119(45)	1.06(18)	0.056(22)	1.44(27)	0(0)	0(1)

Table 5.48: Eigenvalues obtained from the solution of the GEVP at the specified t/t_0, and masses extracted using (4.19). 4 × 4 basis of $\{\mathcal{O}_0'^{E_1^{++}}, \mathcal{O}_1'^{E_1^{++}}, \mathcal{O}_2'^{E_1^{++}}, \mathcal{O}_2'^{E_1^{++}}\}$ operators with $|\vec{p}| = 0$ measured on the fine lattices. We do not show λ^3 or $am(\lambda^3)$ as in all cases they are poorly determined.

5.13.2 Factorising Fits

We have performed 4 × 4 fully correlated factorising fits to the matrix of correlators formed using the bases of operators $\{\mathcal{O}_0^{E_1^{++}}, \mathcal{O}_1^{E_1^{++}}, \mathcal{O}_2^{E_1^{++}}, \mathcal{O}_3^{E_1^{++}}\}$ and $\{\mathcal{O}_0'^{E_1^{++}}, \mathcal{O}_1'^{E_1^{++}}, \mathcal{O}_2'^{E_1^{++}}, \mathcal{O}_3'^{E_1^{++}}\}$ for two and three-exponentials, the results presented in Tables 5.49 and 5.50. As with the pseudoscalar glueball it was found that the most stable fit results were obtained using $t_{\text{min}} = 1$.

5.13.3 Overall Average

In Table 5.51 we present the estimates of the systematic errors determined for them masses extracted from the factorising fits on correlators formed using the $\mathcal{O}^{E_1^{++}}$ operators and those formed using the $\mathcal{O}'^{E_1^{++}}$. We include only points where the error is well

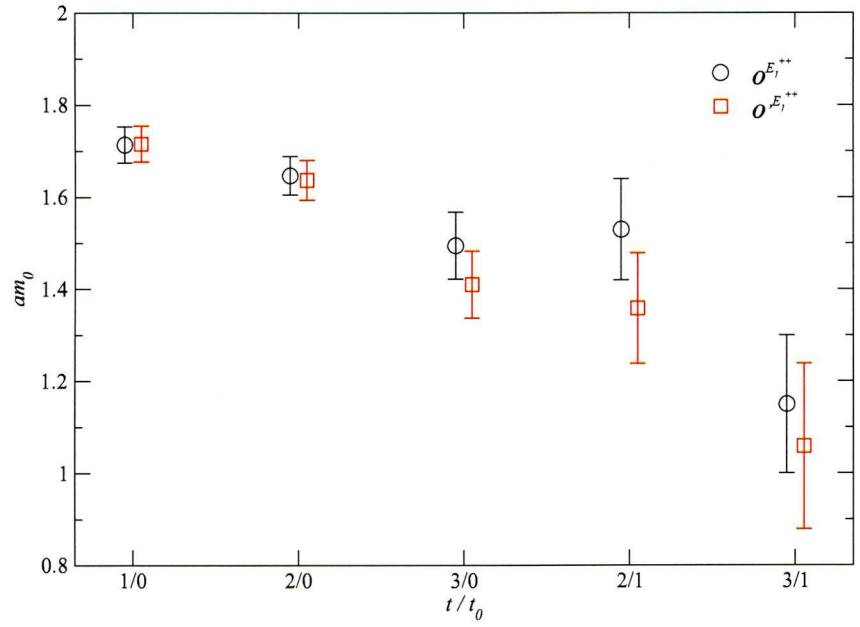

Figure 5.46: The masses extracted from the groundstate variational eigenvalues using (4.19) for different t/t_0 projections performed on 4×4 matrices of correlators formed using the bases of tensor glueball operators $\{\mathcal{O}_0^{E_1^{++}}, \mathcal{O}_1^{E_1^{++}}, \mathcal{O}_2^{E_1^{++}}, \mathcal{O}_3^{E_1^{++}}\}$ and $\{\mathcal{O}_0'^{E_1^{++}}, \mathcal{O}_1'^{E_1^{++}}, \mathcal{O}_2'^{E_1^{++}}, \mathcal{O}_3'^{E_1^{++}}\}$ measured with $|\vec{p}| = 0$ on the coarse lattices.

N_{exp}	t_{min}	t_{max}	am_0	am_1	am_2	χ^2/d.o.f.
2	1	3	1.5222(88)	1.94[–]	—	1.096
	1	4	1.5226(93)	22.49[–]	—	1.028
	1	5	1.499(11)	30.92[–]	—	1.007
	1	6	1.5197(93)	22.65[–]	—	0.809
	1	7	1.5201(94)	22.77[–]	—	0.711
	1	8	1.5196(93)	22.66[–]	—	0.635
3	1	3	1.504(14)	1.921(74)	4(1)	0.160
	1	4	1.51[–]	1.885(54)	4.28[–]	0.187
	1	5	1.505(11)	1.890(64)	4.10[–]	0.267
	1	6	1.505(11)	1.890(63)	3.92[–]	0.261
	1	7	1.506(12)	1.891(64)	3.91[–]	0.244
	1	8	1.506(11)	1.884(65)	3.95[–]	0.229

Table 5.49: Fitted mass parameters for two and three-exponential factorising fully correlated fits to a 4×4 matrix of correlators formed using a basis of operators $\{\mathcal{O}_0^{E_1^{++}}, \mathcal{O}_1^{E_1^{++}}, \mathcal{O}_2^{E_1^{++}}, \mathcal{O}_3^{E_1^{++}}\}$ measured on the coarse lattices with $|\vec{p}| = 0$ for varying t_{max} with t_{min} fixed at $t = 1$. Where errors are quoted as [–] this indicates that the gradient in that direction of parameter space could not be determined, *i.e.* that the parameter is essentially free.

N_{exp}	t_{min}	t_{max}	am_0	am_1	am_2	χ^2/d.o.f.
2	1	3	1.527(11)	2.83[−]	—	0.890
	1	4	1.527(11)	2.83[−]	—	0.755
	1	5	1.516(12)	2.79[−]	—	0.652
	1	6	1.515(12)	2.79[−]	—	0.589
	1	7	1.515(12)	2.78[−]	—	0.520
	1	8	1.515(12)	2.77[−]	—	0.476
3	1	4	1.479(28)	2.00(15)	3.39(34)	0.136
	1	5	1.48[−]	2.06(13)	3.39(14)	0.165
	1	6	1.490(15)	2.39(12)	19.56(11)	0.186
	1	7	1.515(12)	2.78[−]	4.41[−]	0.530
	1	8	1.490(14)	2.40(13)	18.77[−]	0.177

Table 5.50: Fitted mass parameters for two and three-exponential factorising fully correlated fits to a 4×4 matrix of correlators formed using a basis of operators $\{\mathcal{O}_0'^{E_1^{++}}, \mathcal{O}_1'^{E_1^{++}}, \mathcal{O}_2'^{E_1^{++}}, \mathcal{O}_3'^{E_1^{++}}\}$ measured on the coarse lattices with $|\vec{p}| = 0$ for varying t_{max} with t_{min} fixed at $t = 1$. Where errors are quoted as [−] this indicates that the gradient in that direction of parameter space could not be determined, *i.e.* that the parameter is essentially free.

determined, so for the $\mathcal{O}^{E_1^{++}}$ operators that is all $N_{\text{exp}} = 2$ fits and all $N_{\text{exp}} = 3$ fits, excluding that for $t_{\text{max}} = 4$. For the $\mathcal{O}'^{E_1^{++}}$ operators we include all $N_{\text{exp}} = 2$ fits and all $N_{\text{exp}} = 3$ except that corresponding to $t_{\text{max}} = 5$. For the eigenvalue masses we use the groundstate mass obtained for the 2/1 and 3/0 projections for both types of operator. In order to get a better idea of the systematics involved we combine the estimates from different operators types (*e.g.* the factorising fits from both the $\mathcal{O}^{E_1^{++}}$ and $\mathcal{O}'^{E_1^{++}}$ correlators). This is also shown in Table 5.51. Applying the PDG averaging process to these combined values we obtain a final estimate of the tensor glueball groundstate on the coarse lattices of

$$am_G^{2^{++}} = 1.510(13) \tag{5.25}$$

and a value of

$$am_G^{2^{++}*} = 1.98(26) \tag{5.26}$$

for the excited state.

Source	Central Value	Stat. Error.	Sys. Error
Factorising Fits, $\mathcal{O}^{E_1^{++}}$	1.5118	0.0079	0.0028
Factorising Fits, $\mathcal{O}'^{E_1^{++}}$	1.5089	0.0118	0.0055
Factorising Fits Combined	1.5099	0.0099	0.0027
Eigenvalue Mass, $\mathcal{O}^{E_1^{++}}$	1.513	0.092	0.025
Eigenvalue Mass, $\mathcal{O}'^{E_1^{++}}$	1.386	0.097	0.036
Eigenvalue Masses Combined	1.450	0.095	0.090

Table 5.51: Estimates of the systematic errors on the tensor glueball groundstate mass, as described in the text.

5.13.4 Comparison of Results

We remove the explicit dependence on the scale a from our results by converting into units of the Sommer parameter and present our results in Table 5.52. Our result for the groundstate is presented along with those values from [106] and [117][9] in Fig. 5.47 and whilst with only one data point of our own we are unable to perform a continuum extrapolation the lattice spacing dependence appears to be very weak — this is consistent with findings of quenched anisotropic studies [106] and [107]

Result	am	$r_0 m$
Coarse – Ground	1.510(13)	5.756(61)
Coarse – Excited	1.98(26)	7.55±1.01

Table 5.52: Tensor glueball mass (ground and first-excited state) from the coarse lattices converted into units of the Sommer parameter r_0.

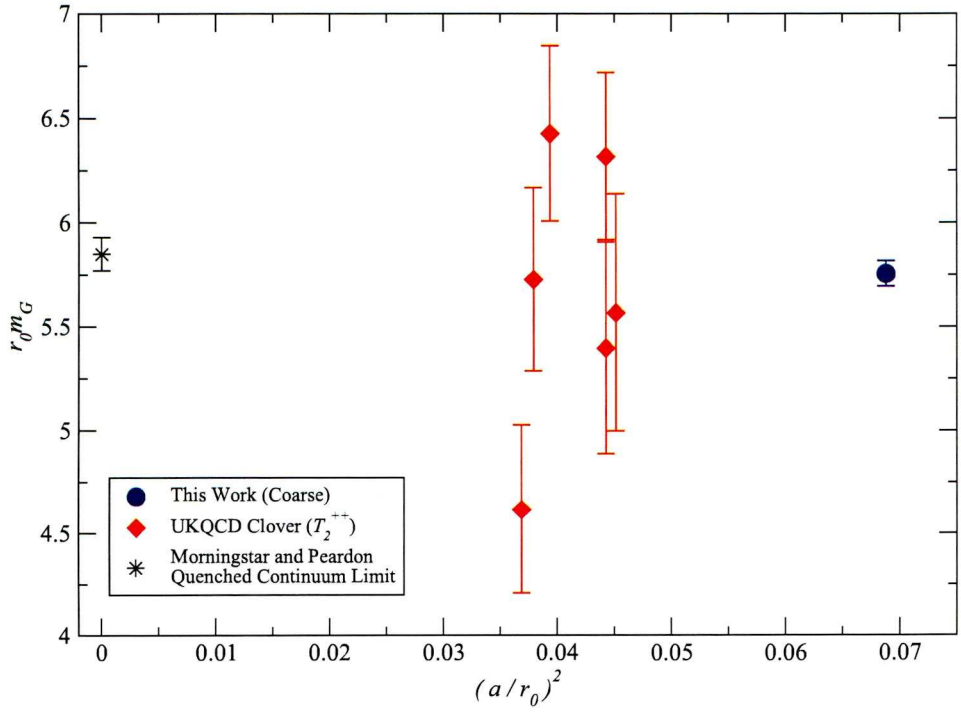

Figure 5.47: Our measurement of the tensor glueball mass on the coarse lattices shown with previous quenched (Morningstar and Peardon [106]) and dynamical (UKQCD Clover [117] — T_2^{++} irrep.) determinations.

In Fig. 5.48 we present our result against the same UKQCD dynamical $\mathcal{O}(a)$ non-perturbatively improved Wilson fermion results, this time against $r_0^2 m_\pi^2$ in order to show any unquenching effects. The lack of precise data for larger pion masses and our

[9]We note that the former uses a set of operators which transform under both the E_1^{++} and T_2^{++} irreps, while the latter uses operators which transform under the T_2^{++} irrep. We use operators which transform under the E_1^{++} irrep only.

single determination of the mass makes it difficult to observe any general trend for the data. Hopefully the addition of a precisely determined data point corresponding to our fine ensemble might help highlight the unquenching behaviour.

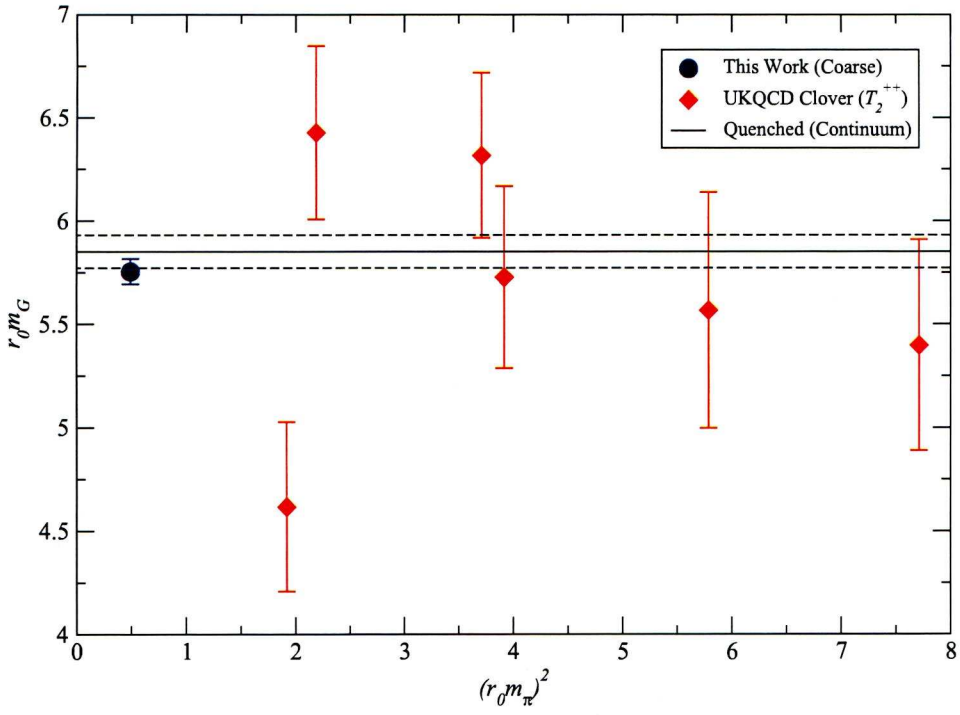

Figure 5.48: Our measurements of the tensor glueball mass shown with those determinations from the dynamical UKQCD Clover [117] measurements. The quenched continuum limit from [106] is shown for comparison.

Chapter 6

Summary and Outlook

6.1 Glueball Spectroscopy

We have measured the scalar, pseudoscalar and tensor sectors of the glueball spectrum on our lattices, obtaining results consistent with those obtained from a high-statistics study of the glueball spectrum in the quenched approximation on anisotropic lattices [106]. This suggests that unquenching effects in the glueball spectrum are reasonably weak.

The higher level of statistics allowed us to perform fits to larger t where for the scalar glueball we believe we observed decay into pseudoscalar pairs. Whilst we made a preliminary attempt to study the mixing of the scalar glueball operators with a $\pi\pi$ state our method was not ideal — a more detailed study in which the full three-point functions are formed as in [147] would be a natural progression.

Furthermore while we obtained good results for the tensor glueball on the coarse lattices we have no results for it on the fine lattices. Since it is a relatively minor extension we would hope to see this computed soon.

6.1.1 Summary Of Analyses and Results

We present a brief summary of the analyses performed and results obtained in Chapter 5.

Scalar Glueball: Coarse Lattices

In Section 5.4 we presented the effective mass results for the coarse scalar glueball. A noticeable dependence on the blocking level was observed and therefore in §5.4.1 we presented the effective mass computed with the variational groundstate correlator in an attempt to eliminate this dependence. Whilst this did give us cleaner results we observed an instability in the variational projections, observable in the distribution of the eigenvalues, which motivated us to perform the variational projection with smaller bases

of operators which proved to give best results with the basis $\{\mathcal{O}_0^{A_1^{++}}, \mathcal{O}_2^{A_1^{++}}, \mathcal{O}_3^{A_1^{++}}\}$. We also saw in the masses extracted from the eigenvalues a first glimpse of a potential $G \to 2\pi$ decay.

In Section 5.5 we presented the effective mass results for the $|\vec{p}| = 1$ coarse scalar glueball correlators finding extremely large statistical errors (Table 5.4), however they were found to be consistent with the $|\vec{p}| = 0$ results (Fig. 5.7). Applying the variational method and computing the effective mass using the groundstate correlators gave us improved results and, using a smaller basis of operators, the $|\vec{p}| = 1$ eigenvalue masses showed excellent consistency with the $|\vec{p}| = 0$ eigenvalues masses (Fig. 5.9) as well as showing us further evidence of $G \to 2\pi$ decay.

In §5.5.3 we briefly present results obtained from the effective mass and eigenvalue masses computed using the alternative scalar glueball operators $\mathcal{O}'^{A_1^{++}}$ which were found to be consistent with the standard operator $\mathcal{O}^{A_1^{++}}$ results (Fig. 5.12). In Fig. 5.13 (§5.5.4) we present a comparison of results obtained from both the effective mass and variational eigenvalue mass methods and observe good consistency.

In Section 5.6 we perform fully-correlated factorising fits to correlators formed using the basis of coarse scalar glueball operators $\{\mathcal{O}_0^{A_1^{++}}, \mathcal{O}_1^{A_1^{++}}, \mathcal{O}_2^{A_1^{++}}, \mathcal{O}_3^{A_1^{++}}\}$. We found that an $N_{\text{exp}} = 3$ model overparameterised the data and that $N_{\text{exp}} = 2$ fits sufficed. The groundstate mass showed a strong downward trend with increasing t_{min} (Figs. 5.14 and 5.15) which is consistent with the behaviour observed in the effective mass analysis. An anomaly was observed where some fits chose groundstates with $am \sim 0.9$ whereas others chose groundstates with $am \sim 1.05$ (Tables 5.6 and 5.7), independent of N_{exp}, $|\vec{p}|$ and fit range. We believe this inconsistency is resolved in Table 5.8 (§5.6.1) where we see that the $N_{\text{exp}} = 3$ fits favouring the lower lying state have unphysically large values for am_3 implying the fit is overparameterised and therefore that those results are unreliable.

As with the effective masses we used the alternative scalar glueball operators $\mathcal{O}'^{A_1^{++}}$ to check the consistency of our results (§5.6.2). Performing fully-correlated factorising fits with $N_{\text{exp}} = 2$ gave poor fits (large values for χ^2/d.o.f.) so we chose to perform uncorrelated factorising fits. The results for both the ground and excited state masses showed excellent consistency with those from fits to correlators formed using the standard operators $\mathcal{O}^{A_1^{++}}$, in particular providing no evidence for a state with $am \sim 0.9$ (Fig. 5.21).

In §5.6.3 we determined the systematic errors on our various determinations of the ground and first excited state masses for the scalar glueball on the coarse lattices (Tables 5.12, 5.13, 5.14, 5.15 and 5.16). We then used the Particle Data Group (PDG) weighted averaging procedure to obtain an overall estimate of the masses and associated

errors (Figs. 5.22 and 5.23), obtaining values of $am = 1.0468(75)$ and $am^* = 1.875(87)$ respectively, and a discussion of the surprisingly small errors on each is given.

Scalar Glueball: Fine Lattices

Having obtained estimates of the scalar glueball mass on the coarse lattices we proceeded to perform a series of similar analyses on the fine lattices. In Section 5.7 we presented the results for the effective masses and variational effective masses and eigenvalues. As with the coarse results the standard effective mass results were rather inconclusive (Table 5.17) and we moved quickly onto the variational effective mass. Here we observed an apparent inconsistency between the effective mass and the eigenvalue mass, the effective mass lying considerably lower than the eigenvalue mass ($am \sim 0.65$ *cf.* $am \sim 0.88$). Again there was some evidence from the eigenvalue masses (Tables 5.19 and 5.20) for a $G \to 2\pi$ decay and, although the statistical errors ruled out a clear identification of it as such, this helped explain the inconsistency between the effective masses and eigenvalue masses.

In Section 5.8 we presented the effective mass results for the $|\vec{p}| = 1$ (Table 5.21) — similar behaviour to the $|\vec{p}| = 0$ results was found and the results were found to be consistent between both (Fig. 5.26). The variational projections for a 4×4 basis of $|\vec{p}| = 1$ operators were found to be particularly unstable (Table 5.22), and we therefore proceeded to experiment with smaller bases of operators. The basis of operators $\{\mathcal{O}_1^{A_1^{++}}, \mathcal{O}_2^{A_1^{++}}, \mathcal{O}_3^{A_1^{++}}\}$ was again found to give the most stable projection (Table 5.23) and a comparison of the $|\vec{p}| = 0$ and $|\vec{p}| = 1$ eigenvalue masses for this basis was given in Fig. 5.28.

In §5.8.2 we presented variational effective mass results computed on correlators formed from a 3×3 basis of the handed scalar glueball operators $\mathcal{O}'^{A_1^{++}}$. Again the variational effective masses were low when compared to the variational eigenvalues, which showed excellent consistency with the eigenvalue masses computed from a basis of standard scalar operators (Fig. 5.30).

As with the coarse scalar glueball results in §5.8.3 we presented a comparison of the results obtained using the effective mass and eigenvalue mass methods (Fig. 5.31). There was a evident divide between those results from the effective mass procedure and those from the eigenvalue procedure, which we attributed to the presence of lower lying states, *e.g.* a 2π state from the decay $G \to 2\pi$.

In Section 5.9 we presented the factorising fit results for the scalar glueball operators on the fine lattices. In contrast to the coarse analysis we found fully-correlated fits to give poorer results than in the coarse analysis (Tables 5.25 and 5.26), however by performing uncorrelated factorising fits (Tables 5.27 and 5.28) we found that these

were equally poor for large $t_{\rm min}$ and therefore chose to continue with fully-correlated fits with small values of $t_{\rm min}$. These results were presented in Tables 5.29 and 5.30 and Figs. 5.32 and 5.33.

Whilst the $|\vec{p}| = 1$ factorising fit results were largely consistent for $N_{\rm exp} = 2$ and $N_{\rm exp} = 3$ for $t_{\rm min} = 1$ the $N_{\rm exp} = 3$ $|\vec{p}| = 0$ results showed significant deviations from the consensus. For the $t_{\rm min} = 2$ fits the $N_{\rm exp} = 3$ results were clearly overparameterised, and the $N_{\rm exp} = 2$ fits showed inconsistencies in the groundstate mass between the $|\vec{p}| = 0$ and $|\vec{p}| = 1$ results. In order to attempt to resolve these inconsistencies fully-correlated factorising fits were performed using smaller (3×3) bases of operators in §5.9.1. The basis $\{\mathcal{O}_1^{A_1^{++}}, \mathcal{O}_2^{A_1^{++}}, \mathcal{O}_3^{A_1^{++}}\}$ provided the most stable fits (Table 5.31), although only for $t_{\rm min} = 1$ and $N_{\rm exp} = 3$, $|\vec{p}| = 1$.

As with the coarse results in §5.9.2 we determined the systematic errors on our various determinations of the scalar glueball on the fine lattices (Tables 5.32, 5.33, 5.34, 5.35 and 5.36). The PDG weighted averaging procedure was then applied in order to obtain a final estimate of the ground and first excited masses (shown in Figs. 5.34 and 5.35 respectively), obtaining final values of $am = 0.8332(59)$ and $am^* = 1.368(17)$.

Glueball Mixing

In Section 5.10 we performed an exploratory study following the methods of [149,150] into the mixing of the scalar glueball and fermionic $\pi\pi$ operators. Whilst the results were in no way conclusive they did indicate, as we have previously found, that at small values of $t_{\rm min}$ one is able to get a better overlap with the 'glueball' state, whereas at larger values of $t_{\rm min}$ the $\pi\pi$ overlap begins to dominate.

Scalar Glueball Continuum and Unquenching Results

In order to best compare our results with those in the literature in Section 5.11 we performed a continuum extrapolation, using the extrapolation form (5.20) from [106]. We addressed concerns regarding the use of this extrapolation form given its failure in [106] due to larger than expected $\mathcal{O}(a^2)$ contributions, and found it gave good results although due to our limited lattice spacings allowed us to determine a central value only for the continuum mass ($r_0 m_G = 4.32$ or $M_G = 1.83$ GeV). This compared well with value of $r_0 m_G = 4.21(11)(4)$ obtained in [106] (Fig. 5.38) and an ensemble at an additional lattice spacing would be welcome in order to provide us with an estimate of the error in our continuum extrapolation.

In Fig. 5.39 we attempted to show the effects of unquenching on the scalar glueball mass however due to our limited range of m_π and doubts as to the validity of the UKQCD $\mathcal{O}(a)$ improved Wilson scalar glueball results [117] we were unable to draw

any particular conclusions.

Pseudoscalar Glueball Results

In §5.12.1 we performed a series of analyses in order to determine the pseudoscalar glueball mass on the coarse lattices. We attempted to study the effective masses on the coarse lattices but the signal was lost to noise far too quickly to resolve any sort of plateau. We instead obtained estimates from the variational eigenvalue masses on a 3×3 basis of pseudoscalar glueball operators $\{\mathcal{O}_0^{A_1^{-+}}, \mathcal{O}_1^{A_1^{-+}}, \mathcal{O}_2^{A_1^{-+}}\}$, presented in Table 5.38 and Fig. 5.40, and from factorising fits with $N_{\text{exp}} = 2$ and $N_{\text{exp}} = 3$ (uncorrelated and fully-correlated respectively). The factorising fit results are shown in Table 5.39.

A systematic difference was observed between these different fits, but since the $N_{\text{exp}} = 3$ fits had reasonably well determined third masses and good χ^2/d.o.f. whilst taking into account the correlations in the data we chose to concentrate on these results.

Estimates of overall systematic error on these determinations of the pseudoscalar glueball groundstate are presented in Tables 5.40 and 5.41 and the final estimate of $am_G^{A_1^{-+}} = 1.560(67)$ is shown in Fig. 5.41. The mass for the first-excited state was determined as $am_G^{A_1^{-+}*} = 1.956(65)$.

The exact same analysis was performed for the fine pseudoscalar glueball with the eigenvalue mass results presented in Table 5.42 and Fig. 5.42 and the factorising fit results presented in Table 5.43. The fine eigenvalue results were equally stable to the coarse results whilst the factorising fit results showed more agreement between the $N_{\text{exp}} = 2$ uncorrelated fits and the $N_{\text{exp}} = 3$ fully-correlated fits. Systematic errors were again determined, shown in Tables 5.44 and 5.45, and the PDG weighted averaging procedure applied to obtain a groundstate pseudoscalar glueball mass on the fine lattices of $am_G^{A_1^{-+}} = 1.265(17)$ (Fig. 5.43) and a mass for the first-excited pseudoscalar glueball of $am_G^{A_1^{-+}} = 1.984(77)$.

We again performed a continuum extrapolation using (5.20) (Fig. 5.44) obtaining a continuum value of $r_0 m_G^{0^{-+}} = 6.61$ ($M_G \sim 2.79$ GeV), which compared well to the quenched determination of $r_0 m_G^{0^{-+}} = 6.33(7)(6)$ from [106]. In Fig. 5.45 we present our results along with those from [117] against $r_0^2 m_\pi^2$ in order to show the effects of unquenching and determined that if there are any unquenching effects then they are indeed weak.

Tensor Glueball Results

In Section 5.13 we presented an analysis of the tensor glueball on the coarse lattices only, since due to a machine failure we did not have the fine operators. Both the $\mathcal{O}^{E_1^{++}}$ and $\mathcal{O}'^{E_1^{++}}$ are used for this analysis.

As with the pseudoscalar glueball the effective mass results for the tensor glueball were extremely poor so we included the eigenvalue mass and factorising fit results only. The results for the eigenvalue masses from 4×4 bases of $\{\mathcal{O}_0^{E_1^{++}}, \mathcal{O}_1^{E_1^{++}}, \mathcal{O}_2^{E_1^{++}}, \mathcal{O}_3^{E_1^{++}}\}$ and $\{\mathcal{O}_0^{\prime E_1^{++}}, \mathcal{O}_1^{\prime E_1^{++}}, \mathcal{O}_2^{\prime E_1^{++}}, \mathcal{O}_3^{\prime E_1^{++}}\}$ are presented in Tables 5.47 and 5.48 respectively. The projections with small t were stable and furthermore the eigenvalues from each basis of operator showed excellent consistency (Fig. 5.46). For the factorising fits fully-correlated fits were performed with both $N_{\text{exp}} = 2$ and $N_{\text{exp}} = 3$ with results presented in Tables 5.49 and 5.50.

The overall systematic errors on each source using different operator types were determined in Table 5.51 and the PDG weighted averaging procedure applied to obtain a final estimate of the tensor glueball groundstate mass on the coarse lattices of $am_G^{2^{++}} = 1.510(13)$ and the first-excited state mass of $am_G^{2^{++}*} = 1.98(26)$.

Since we had results for the coarse lattice only we were unable to perform a continuum extrapolation but by including the results from [117] and [106] we were able to gauge the degree of lattice spacing dependence as shown in Fig 5.47 and determined it to be weak which is consistent with the quenched anisotropic studies [106] and [107].

In Fig 5.48 we showed our result along with those from [117] against $r_0^2 m_\pi^2$ and found there to be no observable unquenching effect. The inclusion of a fine data point here would be useful.

6.2 Meson Spectroscopy and Mixing

There is strong evidence from both lattice QCD [140,149,151] and experiment [129] that the 'glueball' and the scalar mesons mix. Such mixing would certainly be a satisfactory way of helping to explain the observed spectrum of scalar singlet resonances between 1 and 2 GeV. Lattice QCD provides an excellent way to study this mixing from first principles. In order to study such mixing one may work with a basis of scalar glueball operators and a basis of scalar meson operators to form a mixing matrix, following the methods of [140] or [149].

It was our intention that this project should include a study of both the scalar non-singlet meson a_0 and the scalar singlet meson f_0 as well as a study of the mixing of the latter with the glueball state, however delays in measurement of the loops as well as unexpected complications in the glueball analyses meant that this was no longer possible. Accurate measurements of both the scalar and pseudoscalar singlet meson sectors is a long-standing goal [141, 152–156] of the UKQCD's staggered spectroscopy program — indeed it is for this purpose the large ensembles described in Chapter 3 have been generated, using a large number of rackyears on the UKQCD's QCDOC [94].

The connected and disconnected diagrams required to study scalar and pseudoscalar flavour-singlet mesons on the lattice have been measured using both the QCDOC and clusters to which we have access, such as ScotGrid [157] and the NW-Grid [158]. The computation of such disconnected diagrams is particularly computationally expensive — as quark loops they are inherently sensitive to fluctuations of the fermion sea. In order to measure these loops we have employed the stochastic source method [159] which allows us to efficiently sample the disconnected loops using noise drawn from a distribution with unit variance and an expectation value of zero; in our case Gaussian distribution was used as this was found to have a lower variance than $Z(2)$ noise in a preliminary study [152][1].

For the computation of the $\mathbf{1} \otimes \mathbf{1}$ and $\gamma_5 \otimes \mathbf{1}$ disconnected operators we have been able to make use of a variance reduction trick unique to staggered fermions due to Venkataraman and Kilcup (VKVR) [160]. This trick exploits the properties of the staggered fermion matrix M and of $M^\dagger M$ in order to recast our stochastic estimator of the disconnected loops into a form with reduced variance. This is applicable for operators which have been shifted by an even number of links within the hypercube, which is the case for both the zero-link $\mathbf{1} \otimes \mathbf{1}$ operator and the four-link $\gamma_5 \otimes \mathbf{1}$ operator. While in principle the reduced stochastic noise allows us to use fewer sources we still choose a conservative number of stochastic sources such that disconnected loops to which the the VKVR trick is not applicable are still determined with an acceptably low variance — we therefore choose $N_{\text{src}} = 64$. Further details of the methods used to measure our disconnected loops can be found in [154].

As the glueball spectrum has been well studied using gluonic operators on our coarse and fine lattices we would hope to include them in a mixing study as described. Furthermore it has been observed that taste breaking effects contribute strongly, predominantly in the form of two-pseudoscalar bubble, to both the f_0 and a_0 meson correlators [133, 141] and the form of these contributions have been determined from within the framework of staggered chiral perturbation theory (SChPT) [161–163] such that they can be taken into account. Whilst the contributions to the f_0 correlator are enhancements of physically allowed decay channels the contributions to the a_0 correlator violate G-parity and as such it is more important that they are taken into account.

The accurate measurement of the η' meson is one of the key physics goals of this project — it will be the first time that the η' will have been measured with such large statistics for dynamical $2 + 1$ flavour fermions. Measurement of the η' itself is particularly demanding — not only does it require the computation of the $\gamma_5 \otimes \mathbf{1}$ disconnected loops but these loops are related to the topological charge of the gauge

[1] It should be pointed out that in a later study with higher statistics [154] the difference between the use of Gaussian and $Z(2)$ noise was found to be marginal, particularly for $N_{\text{src}} > 8$.

configuration. Topological modes have been known to show long autocorrelation times [164] compared to other observables and as such larger numbers of configurations may be required to ensure statistical errors are under control. Furthermore the η' has been targeted as a potential test of the validity of the fourth-root trick due to its sensitivity to the underlying topology and the axial-anomaly [66, 70].

In principle the η and η' mesons mix with the pseudoscalar glueball. Whilst we have found the mass of the pseudoscalar glueball to be large – $M_G \sim 2.8$ GeV – it would still be interesting to include the pseudoscalar glueball interpolating operators in a mixing scenario, such as that put forth by Cheng, Li and Liu [135].

Bibliography

[1] M. Gell-Mann, Phys. Lett. **8**, 214 (1964).

[2] G. Zweig, CERN-TH-412.

[3] A. Chodos, R. L. Jaffe, K. Johnson, C. B. Thorn and V. F. Weisskopf, Phys. Rev. D **9**, 3471 (1974).

[4] M. E. Peskin and D. V. Schroeder, *An Introduction to quantum field theory*, Fifth ed. (Addison-Wesley, 1995).

[5] K. G. Wilson, Phys. Rev. **D10**, 2445 (1974).

[6] P. Weisz, Nucl. Phys. **B212**, 1 (1983).

[7] M. Luscher and P. Weisz, Commun. Math. Phys. **97**, 59 (1985).

[8] K. Symanzik, Nucl. Phys. **B226**, 187 (1983).

[9] K. Symanzik, Nucl. Phys. **B226**, 205 (1983).

[10] HPQCD, A. Hart, G. M. von Hippel and R. R. Horgan, Phys. Rev. **D79**, 074008 (2009), 0812.0503.

[11] M. Luscher and P. Weisz, Phys. Lett. **B158**, 250 (1985).

[12] M. Luscher and P. Weisz, Nucl. Phys. **B240**, 349 (1984).

[13] G. P. Lepage and P. B. Mackenzie, Phys. Rev. **D48**, 2250 (1993), hep-lat/9209022.

[14] H. D. Trottier, Phys. Rev. **D55**, 6844 (1997), hep-lat/9611026.

[15] M. G. Alford, T. R. Klassen and G. P. Lepage, Phys. Rev. **D58**, 034503 (1998), hep-lat/9712005.

[16] P. Lepage, Nucl. Phys. Proc. Suppl. **60A**, 267 (1998), hep-lat/9707026.

[17] L. H. Karsten and J. Smit, Nucl. Phys. **B183**, 103 (1981).

[18] K. Wilson, *New Phenomena in Subnuclear Physics* (Plenum, New York, 1977), .

[19] H. B. Nielsen and M. Ninomiya, Nucl. Phys. **B185**, 20 (1981).

[20] H. B. Nielsen and M. Ninomiya, Nucl. Phys. **B193**, 173 (1981).

[21] H. B. Nielsen and M. Ninomiya, Phys. Lett. **B105**, 219 (1981).

[22] H. Kluberg-Stern, A. Morel, O. Napoly and B. Petersson, Nucl. Phys. **B220**, 447 (1983).

[23] N. Kawamoto and J. Smit, Nucl. Phys. **B192**, 100 (1981).

[24] H. J. Rothe, *Lattice gauge theories: An Introduction*, World Sci. Lect. Notes Phys. Vol. 74, Third ed. (World Scientific, 2005).

[25] I. Montvay and G. Munster, *Quantum fields on a lattice*Cambridge Monographs on Mathematical Physics (Cambridge University Press, 1994).

[26] Y.-b. Luo, Phys. Rev. **D55**, 353 (1997), hep-lat/9604025.

[27] W.-J. Lee and S. R. Sharpe, Phys. Rev. **D60**, 114503 (1999), hep-lat/9905023.

[28] S. R. Sharpe, Nucl. Phys. Proc. Suppl. **34**, 403 (1994), hep-lat/9312009.

[29] Y.-b. Luo, Phys. Rev. **D57**, 265 (1998), hep-lat/9702013.

[30] G. W. Kilcup and S. R. Sharpe, Nucl. Phys. **B283**, 493 (1987).

[31] M. F. L. Golterman, Nucl. Phys. **B273**, 663 (1986).

[32] M. F. L. Golterman and J. Smit, Nucl. Phys. **B255**, 328 (1985).

[33] MILC, C. Bernard *et al.*, Nucl. Phys. Proc. Suppl. **119**, 769 (2003).

[34] UKQCD, A. Hart, Nucl. Phys. Proc. Suppl. **106**, 575 (2002), hep-lat/0110167.

[35] APE, M. Albanese *et al.*, Phys. Lett. **B192**, 163 (1987).

[36] M. Teper, Phys. Lett. **B183**, 345 (1987).

[37] T. Blum *et al.*, Phys. Rev. **D55**, 1133 (1997), hep-lat/9609036.

[38] G. P. Lepage, Phys. Rev. **D59**, 074502 (1999), hep-lat/9809157.

[39] S. Naik, Nucl. Phys. **B316**, 238 (1989).

[40] MILC, K. Orginos, D. Toussaint and R. L. Sugar, Phys. Rev. **D60**, 054503 (1999), hep-lat/9903032.

[41] HPQCD, E. Follana *et al.*, Phys. Rev. **D75**, 054502 (2007), hep-lat/0610092.

[42] HPQCD, C. T. H. Davies *et al.*, (2008), 0810.3548.

[43] P. H. Ginsparg and K. G. Wilson, Phys. Rev. **D25**, 2649 (1982).

[44] H. Neuberger, Phys. Lett. **B417**, 141 (1998), hep-lat/9707022.

[45] D. B. Kaplan, Phys. Lett. **B288**, 342 (1992), hep-lat/9206013.

[46] Y. Shamir, Nucl. Phys. **B406**, 90 (1993), hep-lat/9303005.

[47] Alpha, R. Frezzotti, P. A. Grassi, S. Sint and P. Weisz, JHEP **08**, 058 (2001), hep-lat/0101001.

[48] F. Farchioni *et al.*, Eur. Phys. J. **C39**, 421 (2005), hep-lat/0406039.

[49] B. Blossier *et al.*, JHEP **07**, 043 (2009), 0904.0954.

[50] ETM, R. Baron *et al.*, PoS **LATTICE2008**, 094 (2008), 0810.3807.

[51] ETM, K. Jansen, C. Michael, A. Shindler and M. Wagner, JHEP **12**, 058 (2008), 0810.1843.

[52] ETM, P. Dimopoulos, C. McNeile, C. Michael, S. Simula and C. Urbach, (2008), 0810.1220.

[53] K. Jansen, A. Nube and A. Shindler, (2008), 0810.0300.

[54] European Twisted Mass, C. Alexandrou *et al.*, Phys. Rev. **D78**, 014509 (2008), 0803.3190.

[55] B. A. Berg, *Markov Chain Monte Carlo Simulations and their Statistical Analysis* (World Scientific, 2004).

[56] D. H. Weingarten and D. N. Petcher, Phys. Lett. **B99**, 333 (1981).

[57] G. H. Golub and C. F. Van Loan, *Matrix Computations*, Third ed. (The John Hopkins University Press, 1996).

[58] N. Metropolis *et al.*, The Journal of Chemical Physics **21**, 1087 (1953).

[59] D. C. Rapaport, *The Art of Molecular Dynamics Simulation*, Second ed. (Cambridge University Press, 2004).

[60] S. Duane and J. B. Kogut, Phys. Rev. Lett. **55**, 2774 (1985).

[61] S. Duane and J. B. Kogut, Nucl. Phys. **B275**, 398 (1986).

[62] S. Duane, A. D. Kennedy, B. J. Pendleton and D. Roweth, Phys. Lett. **B195**, 216 (1987).

[63] C. Bernard, M. Golterman and Y. Shamir, Phys. Rev. **D73**, 114511 (2006), hep-lat/0604017.

[64] C. Bernard, M. Golterman, Y. Shamir and S. R. Sharpe, Phys. Lett. **B649**, 235 (2007), hep-lat/0603027.

[65] S. R. Sharpe, PoS **LAT2006**, 022 (2006), hep-lat/0610094.

[66] A. S. Kronfeld, PoS **LAT2007**, 016 (2007), 0711.0699.

[67] M. Creutz, (2006), hep-lat/0603020.

[68] M. Creutz, Phys. Lett. **B649**, 230 (2007), hep-lat/0701018.

[69] M. Creutz, Phys. Lett. **B649**, 241 (2007), 0704.2016.

[70] M. Creutz, PoS **LAT2007**, 007 (2007), 0708.1295.

[71] S. A. Gottlieb, W. Liu, D. Toussaint, R. L. Renken and R. L. Sugar, Phys. Rev. **D35**, 2531 (1987).

[72] P. de Forcrand and T. Takaishi, Nucl. Phys. Proc. Suppl. **53**, 968 (1997), hep-lat/9608093.

[73] R. Frezzotti and K. Jansen, Phys. Lett. **B402**, 328 (1997), hep-lat/9702016.

[74] ETM, K. Jansen and C. Urbach, PoS **LAT2006**, 203 (2006), hep-lat/0610015.

[75] K. Jansen *et al.*, PoS **LAT2007**, 036 (2007), 0709.4434.

[76] PACS-CS, S. Aoki *et al.*, (2008), 0807.1661.

[77] JLQCD, K. I. Ishikawa *et al.*, Nucl. Phys. Proc. Suppl. **119**, 1000 (2003), hep-lat/0209061.

[78] M. A. Clark and A. D. Kennedy, Nucl. Phys. Proc. Suppl. **129**, 850 (2004), hep-lat/0309084.

[79] M. A. Clark, A. D. Kennedy and Z. Sroczynski, Nucl. Phys. Proc. Suppl. **140**, 835 (2005), hep-lat/0409133.

[80] M. A. Clark, *The Rational Hybrid Monte Carlo Algorithm*, PhD thesis, University of Edinburgh, 2005.

[81] E. Y. Remez, US Atomic Energy Commision .

[82] A. Frommer, B. Nockel, S. Gusken, T. Lippert and K. Schilling, Int. J. Mod. Phys. **C6**, 627 (1995), hep-lat/9504020.

[83] B. Jegerlehner, (1996), hep-lat/9612014.

[84] M. A. Clark and A. D. Kennedy, Phys. Rev. Lett. **98**, 051601 (2007), hep-lat/0608015.

[85] M. A. Clark and A. D. Kennedy, Phys. Rev. **D75**, 011502 (2007), hep-lat/0610047.

[86] C. Bernard *et al.*, Nucl. Phys. Proc. Suppl. **106**, 199 (2002).

[87] CP-PACS and JLQCD, A. Ukawa, Nucl. Phys. Proc. Suppl. **106**, 195 (2002).

[88] UKQCD, H. Wittig, Nucl. Phys. Proc. Suppl. **106**, 197 (2002), hep-lat/0203021.

[89] M. Hasenbusch, Phys. Lett. **B519**, 177 (2001), hep-lat/0107019.

[90] J. C. Sexton and D. H. Weingarten, Nucl. Phys. **B380**, 665 (1992).

[91] M. A. Clark, PoS **LAT2006**, 004 (2006), hep-lat/0610048.

[92] T. Takaishi and P. de Forcrand, Phys. Rev. **E73**, 036706 (2006), hep-lat/0505020.

[93] I. P. Omelyan, I. M. Mryglod and R. Folk, Comput. Phys. Commun. **151**, 272 (2003).

[94] P. Boyle *et al.*, Nucl. Phys. Proc. Suppl. **140**, 169 (2005).

[95] S. J. Brodsky, G. P. Lepage and P. B. Mackenzie, Phys. Rev. D **28**, 228 (1983).

[96] E. Eichten *et al.*, Phys. Rev. Lett. **34**, 369 (1975).

[97] J. L. Richardson, Phys. Lett. **B82**, 272 (1979).

[98] W. Celmaster, H. Georgi and M. Machacek, Phys. Rev. **D17**, 879 (1978).

[99] UKQCD, S. P. Booth *et al.*, Phys. Lett. **B294**, 385 (1992), hep-lat/9209008.

[100] C. W. Bernard *et al.*, Phys. Rev. **D62**, 034503 (2000), hep-lat/0002028.

[101] K. Schilling, Nucl. Phys. Proc. Suppl. **83**, 140 (2000), hep-lat/9909152.

[102] R. Sommer, Nucl. Phys. **B411**, 839 (1994), hep-lat/9310022.

[103] B. Efron, Biometrika **68**, 589 (1981).

[104] B. Alles, G. Boyd, M. D'Elia, A. Di Giacomo and E. Vicari, Phys. Lett. **B389**, 107 (1996), hep-lat/9607049.

[105] C. J. Morningstar and M. J. Peardon, Phys. Rev. **D56**, 4043 (1997), hep-lat/9704011.

[106] C. J. Morningstar and M. J. Peardon, Phys. Rev. **D60**, 034509 (1999), hep-lat/9901004.

[107] Y. Chen *et al.*, Phys. Rev. **D73**, 014516 (2006), hep-lat/0510074.

[108] A. Nolan, M. Peardon and A. O Cais, PoS **LAT2007**, 127 (2007).

[109] P. Meier, Biometrics **9**, 59 (1953).

[110] C. Michael and I. Teasdale, Nucl. Phys. **B215**, 433 (1983).

[111] M. Luscher and U. Wolff, Nucl. Phys. **B339**, 222 (1990).

[112] D. B. Leinweber, W. Melnitchouk, D. G. Richards, A. G. Williams and J. M. Zanotti, Lect. Notes Phys. **663**, 71 (2005), nucl-th/0406032.

[113] J. J. Dudek, R. G. Edwards, N. Mathur and D. G. Richards, Phys. Rev. **D77**, 034501 (2008), 0707.4162.

[114] T. Burch *et al.*, Phys. Rev. **D73**, 094505 (2006), hep-lat/0601026.

[115] T. Burch *et al.*, Phys. Rev. **D74**, 014504 (2006), hep-lat/0604019.

[116] B. Berg and A. Billoire, Nucl. Phys. **B221**, 109 (1983).

[117] UKQCD, A. Hart and M. Teper, Phys. Rev. **D65**, 034502 (2002), hep-lat/0108022.

[118] C. Michael and M. Teper, Nucl. Phys. **B314**, 347 (1989).

[119] UKQCD, C. R. Allton *et al.*, Phys. Rev. **D65**, 054502 (2002), hep-lat/0107021.

[120] A. C. Lichtl, PoS **LAT2007**, 118 (2007), 0711.4072.

[121] C. Michael, Phys. Rev. **D49**, 2616 (1994), hep-lat/9310026.

[122] C. Michael and A. McKerrell, Phys. Rev. **D51**, 3745 (1995), hep-lat/9412087.

[123] H. Fritzsch and M. Gell-Mann, eConf **C720906V2**, 135 (1972), hep-ph/0208010.

[124] C. Michael and M. Teper, Phys. Lett. **B206**, 299 (1988).

[125] UKQCD, G. S. Bali *et al.*, Phys. Lett. **B309**, 378 (1993), hep-lat/9304012.

[126] H.-B. Liao, Eur. Phys. J. **A31**, 461 (2007).

[127] M. S. Chanowitz, Int. J. Mod. Phys. **A21**, 5535 (2006), hep-ph/0609217.

[128] PANDA, J. S. Lange, Int. J. Mod. Phys. **A24**, 369 (2009).

[129] E. Klempt and A. Zaitsev, Phys. Rept. **454**, 1 (2007), 0708.4016.

[130] V. Crede and C. A. Meyer, Prog. Part. Nucl. Phys. **63**, 74 (2009), 0812.0600.

[131] BES, G. Xu, (2008), 0805.1960.

[132] Particle Data Group, C. Amsler *et al.*, Phys. Lett. **B667**, 1 (2008).

[133] C. Aubin *et al.*, Phys. Rev. **D70**, 094505 (2004), hep-lat/0402030.

[134] RBC and UKQCD, D. J. Antonio *et al.*, Phys. Rev. **D75**, 114501 (2007), hep-lat/0612005.

[135] H.-Y. Cheng, H.-n. Li and K.-F. Liu, Phys. Rev. **D79**, 014024 (2009), 0811.2577.

[136] T. Gutsche, V. E. Lyubovitskij and M. C. Tichy, Phys. Rev. **D80**, 014014 (2009), 0904.3414.

[137] TPC/Two Gamma, H. Aihara *et al.*, Phys. Rev. Lett. **57**, 51 (1986).

[138] H.-Y. Cheng, Int. J. Mod. Phys. **A24**, 3392 (2009), 0901.0741.

[139] U. M. Heller, Phys. Lett. **B362**, 123 (1995), hep-lat/9508009.

[140] UKQCD, A. Hart, C. McNeile, C. Michael and J. Pickavance, Phys. Rev. **D74**, 114504 (2006), hep-lat/0608026.

[141] E. B. Gregory, A. C. Irving, C. C. McNeile, S. Miller and Z. Sroczynski, PoS **LAT2005**, 027 (2006), hep-lat/0510066.

[142] M. Loan and Y. Ying, Prog. Theor. Phys. **116**, 169 (2006), hep-lat/0603030.

[143] C. Michael, Acta Phys. Polon. **B21**, 119 (1990).

[144] R. W. Johnson and M. J. Teper, Phys. Rev. **D66**, 036006 (2002), hep-ph/0012287.

[145] H. B. Meyer and M. J. Teper, Nucl. Phys. **B658**, 113 (2003), hep-lat/0212026.

[146] S. Miller, *A Study of Glueballs and Scalar Mesons in Lattice QCD*, PhD thesis, University of Liverpool, 2005.

[147] J. Sexton, A. Vaccarino and D. Weingarten, Phys. Rev. Lett. **75**, 4563 (1995), hep-lat/9510022.

[148] L. Lellouch and M. Luscher, Commun. Math. Phys. **219**, 31 (2001), hep-lat/0003023.

[149] UKQCD, C. McNeile and C. Michael, Phys. Rev. **D63**, 114503 (2001), hep-lat/0010019.

[150] C. Michael, private communication.

[151] W.-J. Lee and D. Weingarten, Phys. Rev. **D61**, 014015 (2000), hep-lat/9910008.

[152] E. B. Gregory, A. C. Irving, C. McNeile, S. Miller and Z. Sroczynski, PoS **LAT2005**, 083 (2006), hep-lat/0509193.

[153] E. B. Gregory, A. C. Irving, C. M. Richards and C. McNeile, PoS **LAT2006**, 176 (2006), hep-lat/0610044.

[154] E. B. Gregory, A. C. Irving, C. M. Richards and C. McNeile, Phys. Rev. **D77**, 065019 (2008), 0709.4224.

[155] E. B. Gregory, A. Irving, C. M. Richards, C. McNeile and A. Hart, PoS **LAT2007**, 099 (2007), 0710.1725.

[156] UKQCD, E. B. Gregory, C. McNeile, A. C. Irving and C. Richards, (2008), 0810.0136.

[157] A. Earl, P. Clark and S. Thorn, ScotGrid: A prototype Tier 2 centre.

[158] The Northwest Grid (NW-Grid), http://www.nw-grid.ac.uk/.

[159] S.-J. Dong and K.-F. Liu, Phys. Lett. **B328**, 130 (1994), hep-lat/9308015.

[160] L. Venkataraman and G. Kilcup, (1997), hep-lat/9711006.

[161] S. Prelovsek, PoS **LAT2005**, 085 (2006), hep-lat/0509083.

[162] C. W. Bernard, C. E. DeTar, Z. Fu and S. Prelovsek, PoS **LAT2006**, 173 (2006), hep-lat/0610031.

[163] C. Bernard, C. E. DeTar, Z. Fu and S. Prelovsek, Phys. Rev. **D76**, 094504 (2007), 0707.2402.

[164] L. Del Debbio, H. Panagopoulos and E. Vicari, JHEP **08**, 044 (2002), hep-th/0204125.